Trigger Studies for SUSY Searches in the 0-Lepton Channel with ATLAS at LHC

Masterarbeit

vorgelegt der
Fakultät für Physik
der
Ludwig-Maximilians-Universität München

von Josephine Verena Laura Wittkowski
geboren am 29. März 1987 in München

München, 23. 9. 2011

Gutachterin: Prof. Dr. Dorothee Schaile

Abstract

Since 2010 the ATLAS detector at the LHC (CERN) has been taking collision data. Supersymmetry is a theoretical framework which serves as an extension of the Standard Model and can theoretically solve its problems. This thesis deals especially with a selection which looks for a supersymmetric signal in events having jets with high transverse momentum and high missing transverse energy. To obtain a signal with events orthogonal to related searches, leptons are vetoed.

The ATLAS data taking system is designed for an event rate of 200 Hz or 400 Hz on average. This is achieved by selecting only interesting events by means of the ATLAS trigger. A promising idea to optimize the data taking rate evaluated in this thesis is a cut on the pseudorapidity of the leading jet at trigger level. The comparison between Monte Carlo simulated supersymmetric signal events and the real data reveals that the jets with the highest transverse momentum in supersymmetric events are more central than the ones in Standard Model events. But it becomes apparent that the efficiency for triggering on supersymmetric events is strongly reduced.

An important variable used in Supersymmetry searches is missing transverse energy. Studying trigger turn-on curves as function of this variable, an unexpected slow rise was observed. This thesis investigates different definitions of missing transverse energy variables and finally traces the unexpected slow rise to a faulty implementation of the calculation of a specific missing transverse energy variable.

Zusammenfassung

Der ATLAS Detektor am LHC (CERN) nimmt seit 2010 Kollisions-Daten. Supersymmetrie ist ein theoretisches Konzept, das als Erweiterung des Standard Modells dient und theoretisch dessen Probleme lösen kann. In dieser Arbeit steht die Auswahl von Ereignissen mit Jets mit hohem Transversalimpuls und mit viel fehlender Energie im Vordergrund, mit denen man nach supersymmetrischen Signal sucht.

Die Daten-Rate am ATLAS darf nicht mehr als 200 Hz oder 400 Hz betragen. Dies wird erreicht indem nur interessante Ereignisse mit Hilfe des ATLAS Triggersystems ausgewählt werden. Es erscheint viel versprechend, die Daten-Rate mit einem Schnitt auf die Pseudorapidität der führenden Jets eines Ereignisses zu optimieren. Der Vergleich mit Monte Carlo simulierten supersymmetrischen Signal-Ereignissen und echten Daten zeigt, dass die Jets mit dem höchten Transversalimpuls in supersymmetrischen Ereignissen zentraler sind als in Standard Modell-Ereignissen. Es stellt sich jedoch heraus, dass die Effizienz beim Triggerns auf supersymmetrische Ereignisse stark vermindert wird.

Fehlende Transversalenergie ist eine wichtige Variable bei der Suche nach Supersymmetrie. Bei der Betrachtung von Turn-on-Kurven für Trigger-Signaturen fällt ein unerwartet langsamer Anstieg auf. Diese Arbeit untersucht verschiedene Definitionen der fehlenden Transversalenergie. Der unerwartet langsame Anstieg wird schließlich auf die falsche Umsetzung der Berechnung einer speziellen fehlenden Transversalenergie-Variablen zurückgeführt.

Sheldon Cooper: Ah, gravity - thou art a heartless bitch.

(from *The Big Bang Theory*, C. Lorre / B. Prady)

Contents

1. Introduction

In the past century the Standard Model of elementary particles with three generations of fermions was developed and - as the name implies - serves as the established framework to explain the subatomic particles and their interactions. All Standard Model constituents have been observed in experiments so far except for one piece of the puzzle: The Higgs boson is assumed to be massive but has not been observed yet.

In the current experiments at the Large Hadron Collider at CERN[1], the mass range of the Higgs boson is narrowed down. It is possible that it will be excluded in all mass ranges with 95 % confidence level by the time the data taking is finished. Although it is the simplest way to make the Standard Model work, unaesthetic theoretical assumptions have been made for this purpose and the Higgs mechanism still leads to many undetermined parameters [1].

If the Higgs boson generating the simplest conceivable Higgs mechanism is going to be excluded, there are new models which make it more difficult to observe the Higgs boson. One will have to take into account the possibility that the Higgs boson can decay into undetectable final states like dark matter or the possibility of two Higgs bosons in the Standard Model Higgs sector [2].

Symmetries and their conservation are some of the most important principles in physics. The functionality of the Standard Model is based on sticking to these laws. All processes on the elementary particle level feature symmetries concerning the conservation of the quantities momentum, energy, angular momentum and charge. The interactions mediated by the strong force therefore conserve e.g. the total hypercharge and the total isospin in every closed system.

In the following an example for symmetry in particle physics will be given. Looking at the quantum numbers of the elementary particles, the hadrons can be arranged by the values of their hypercharge and their third isospin component. There is an obvious sym-

---

[1] CERN (French): **C**onseil **E**uropéen pour la **R**echerche **N**ucléaire

metry between particles and antiparticles. A baryon octet (total spin $\frac{1}{2}$ for each baryon), a baryon decuplet (total spin $\frac{3}{2}$) and a meson octet with the eight lightest mesons can be formed. These hadrons are built by the smallest known constituents of matter - by two (mesons) or three (baryons) quarks. The hexagonal octets display symmetry in a high degree: the particles and antiparticles are seated at opposite places, displaying the opposite charge and forming isospin doublets (see figure 1.1) [3].

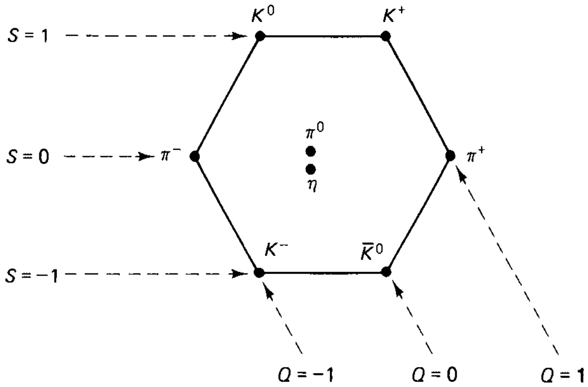

Figure 1.1.: The meson octet [4]

One might say that it is the aim to find a fundamental symmetry in elementary particle physics. A theory based on this attempt is Supersymmetry. It states an extension to the Standard Model. In this framework the relation between fermions and bosons again entails symmetry - each Standard Model fermion gets a supersymmetric bosonic partner and to each Standard Model boson a supersymmetric fermion is assigned. The superpartners have different masses and therefore Supersymmetry is believed to be a broken symmetry. Coming back to the Higgs mechanism, in Supersymmetry the Higgs sector consists of five Higgs bosons plus their superpartners (the Higgsinos). The constraints on the properties of the Higgs bosons are changed which leads to new searched-for signals. Supersymmetry would also solve some problems the Standard Model has to deal with. For example does it propose new candidates for the dark matter.

This thesis concentrates on the evaluation of triggers for supersymmetric events to make it more likely that those can be found in the data taken by ATLAS. ATLAS is one of the experiments connected to the Large Hadron Collider. After an initial proton-proton collision, the constituents of the protons (quarks) are not directly visible as they immediately start forming new hadrons. The whole centre-of-mass energy is used to compose new particles. It can only be kept track of the final states to get information about which particle states were formed inside the ATLAS detector in the meantime. The structure of subatomic particles is only visible in dynamic processes and interactions [3].

A survey of the constituents and functionality of the Standard Model will be given in the beginning of this work. The introduction of the framework of Supersymmetry is motivated by unresolved aspects of the Standard Model. The ATLAS detector is presented in chapter 3.2 and it will be explained how the read-out information is used to reconstruct physical particles.

The data rate recorded by ATLAS must not increase as the luminosity goes up. Therefore a possibility of reducing the data rate will be evaluated by cutting on the characteristics of the reconstructed final state particles. A high efficiency for the observation of supersymmetric signal must still be sustained.

There can be missing energy in an event as not all particles can be detected in ATLAS. Looking at the rate of events which pass the trigger requirements, a discrepancy between two different reconstruction algorithms for the missing transverse energy is observed. The origin of this deviation will be investigated in chapter 8.4.

2. Theoretical Background

2.1. The Standard Model

The Standard Model of elementary particle physics describes the behaviour of the smallest known constituents of the universe and the forces which act on them. It was developed in the 20th century and most of its hypotheses were proven by the experimental discovery of particles and the measurement of their interactions.

2.1.1. Theoretical Principles

Action S as an attribute of the dynamics of a physical system can be expressed as the integral over time of the Lagrange function L. The Lagrange function itself is the spatial integral of the Lagrangian density $\mathscr{L}$ (briefly: the Lagrangian). All equations of motion can be derived from it and the evolution of a field ϕ can be determined [5].

$$S = \int L \, \mathrm{d}t = \int \mathscr{L}(\phi, \partial_\mu \phi) \, \mathrm{d}^4 x \tag{2.1}$$

The Lagrangian wave functions summarize the dynamics of a system. They remain invariant under a continuous group of local transformations where a local phase difference is created. This is called gauge invariance.

The impact of the electromagnetic force is described by **Q**uantum **E**lectro**d**ynamics (QED). The force is mediated by the exchange of massless (virtual) photons between electrically charged particles [5].

The electromagnetic and the weak forces may be treated independently for energy values below a special unification energy. For higher energies both merge into the electroweak force. The weak force can not be described as a gauge theory of its own and therefore it is reasonable to unify both the electromagnetic and the weak forces to the electroweak force. Otherwise this leads to inconsistencies concerning the generators of the groups allocated to the electromagnetic and the weak force [6]. This unification represents the coupling of fermions via W-bosons, Z-bosons or photons. Bosons are particles with integer spin, fermions have half-integer spin quantum numbers.

The Lagrangian which describes the electroweak interaction is

$$\mathscr{L}_{electroweak} = \sum_k \bar{\psi}_k i\gamma^\mu D_\mu \psi_k - \frac{1}{4} B_{\mu\nu} B^{\mu\nu} - \frac{1}{4} \vec{W}_{\mu\nu} \vec{W}^{\mu\nu} \tag{2.2}$$

with fields which are allocated to particles. For example, ψ refers to a fermion and $\bar{\psi}$ to an anti-fermion. D^μ denotes the covariant derivative

$$D^\mu := \partial^\mu + iqA^\mu. \tag{2.3}$$

$$B^{\mu\nu} = \partial^\mu B^\nu - \partial^\nu B^\mu \tag{2.4}$$

and

$$W^{\mu\nu} = \partial^\mu \vec{W}^\nu - \partial^\nu \vec{W}^\mu - g\vec{W}^\mu \times \vec{W}^\nu \tag{2.5}$$

are the field strength tensors from which the fields for the bosons W^+, W^-, Z^0 and γ are attained.
Weak interactions involve only left-handed fermions and right-handed anti-fermions. The helicity expresses the orientation of the momentum vector and the spin vector of a particle [6]. This model of the electroweak unification was formulated by A. Salam, S. Glashow and S. Weinberg.

In consequence of the Pauli principle, a fermion has an anti-symmetric wave function in total. A fermionic particle state which is made up from three quarks of the same flavour and charge features symmetric space, spin and flavour functions; it is thus also symmetric in total. The baryon $|\Delta^{++}> = |uuu>$ serves as an example [4]. To solve this problem, colour was introduced ad hoc as a quantum number of quarks by Han, Nambu, Greenberg and Gell-Mann. The colours red, anti-red, green, anti-green, blue and anti-blue $(r, \bar{r}, g, \bar{g}, b, \bar{b})$ as attributes of quarks in **Q**uantum **C**hromo**d**ynamics (QCD) are properties in the fashion of electromagnetic charge. Thus the massless gluons also carry colour, namely a combination of colour and anti-colour. An octet of eight possible gluons is available which mediate the strong force between quarks. The corresponding Lagrangian is

$$\mathscr{L}_{QCD} = \bar{\psi}(i\gamma_\mu D^\mu - m)\psi - \frac{1}{4}\vec{G}_{\mu\nu}\vec{G}^{\mu\nu}. \tag{2.6}$$

The QCD field strength tensor

$$\vec{G}^{\mu\nu} = \partial^\mu \vec{G}^\nu - \partial^\nu \vec{G}^\mu - g_s \vec{G}^\mu \times \vec{G}^\nu \tag{2.7}$$

is composed by the gluon fields $\vec{G}_\mu$ and the SU(3) vector product. From this Lagrangian can be concluded that gluons interact with each other, too, as there are only gluons involved in the third term of equation (2.7) [6].

2.1.2. Higgs Mechanism

The Standard Model is a renormalizable quantum field theory. Divergent amplitudes for interaction processes are absorbed by the redefinition of bare properties of particles which do not have a physical equivalent [4].

The Higgs Mechanism was introduced to give a reason for the masses of the mediating W^+, W^- and Z^0 bosons. Their masses can only be explained by the spontaneous symmetry breaking of the additional Higgs field. Otherwise the gauge invariance would be destructed and renormalizability can no longer be assumed.

The ground state of the complex scalar Higgs field does not possess the symmetry of the basic equation and corresponds to a non-zero constant. The consequence of choosing a single specific phase is the breaking of the global symmetry; massless scalar Goldstone bosons are introduced. They can be absorbed into the fields by proper transformations. Therefore, terms in the Lagrangian depend both on the Higgs field and the fields of the bosons:

$$\mathscr{L}_{Higgs} = \frac{1}{2}(D_\mu\phi)^\dagger(D^\mu\phi) - V(\phi) - \tilde{g}_f(\bar{R}\phi^\dagger L + \bar{L}\phi R). \tag{2.8}$$

$$D_\mu = \partial_\mu + \frac{1}{2}ig'YB_\mu(x) + \frac{1}{2}ig\vec{\tau}\vec{W}_\mu(x) \tag{2.9}$$

is the covariant derivative.

The wine bottle potential

$$V(\phi) = -\mu^2 |\phi|^2 + \lambda^2 |\phi|^4 \tag{2.10}$$

together with the first term of equation (2.8) describes both the mass acquirement of the bosons via the coupling to the Higgs boson and the self-coupling of the Higgs bosons [6]. The last term in equation (2.8) theoretically states the masses of fermions as the

Higgs boson is supposed to interact with those via the Yukawa coupling.
It is the Higgs mechanism which causes the electroweak symmetry breaking and makes the $W^{\pm}$ and Z^0 bosons massive. Hence the observation of these massive bosons is theoretically explained. According to the theory of the Higgs mechanism the Higgs boson itself is also assumed to have a mass. The whole mechanism still needs to be experimentally verified.

2.1.3. Forces

The Standard Model is put together in the sum of the three Lagrangians introduced. The three fundamental forces have different ranges depending on the strengths of the couplings between mediators and interacting particles. The strength of the electromagnetic interaction between particles which carry an electromagnetic charge is determined by the dimensionless fine-structure constant[1] $\alpha = \frac{e^2}{4\pi\hbar c} \approx \frac{1}{137}$. The weak force has a much smaller field strength which leads to a coupling only of $\mathcal{O}(10^{-13})$. An interesting feature comes up considering the strong coupling constant: $\alpha_s(q^2)$ strongly depends on the momentum transfer q in the interaction process. For very large q^2 and small distances between quarks this leads to the so-called asymptotic freedom, the quarks behaving as if they were free. On the other hand the coupling becomes very strong for small momentum transfer (see figure 2.1) [4].

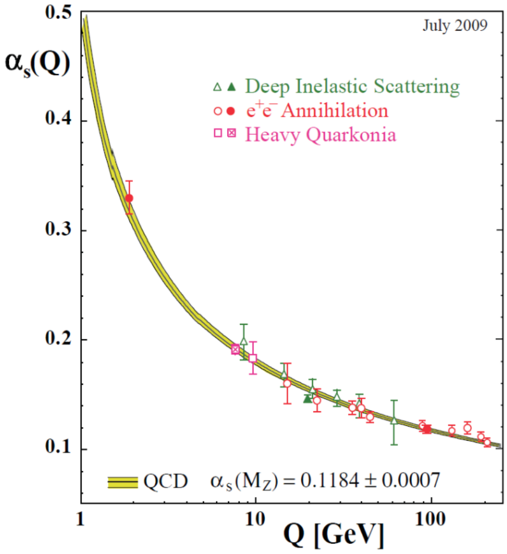

Figure 2.1.: Summary of measurements of the strong coupling constant α_s [8]

---

[1] In the following, $\hbar = c = 1$.

Of course there is also the gravitational force which is much weaker compared to the others. It is not included in the Standard Model unification of the forces. Efforts have been made to include all four kinds of interactions in a **G**rand **U**nifying **T**heory (GUT) as it is assumed that they were unified in the early stages of the universe when the temperatures were very high [4].

2.1.4. Particle Zoo

The particles of the Standard Model are classified by their spin quantum number which is the projection of the intrinsic orbital angular momentum vector. Besides they are grouped according to their role in the interactions of particles.

The bosons are the mediating particles. The fermions are divided into three generations for the leptons and the quarks. For masses and charges of the elementary particles see table 2.1 and 2.2. e is the elementary charge equal to the charge of an electron, $e = 1.602 \times 10^{-19}$ C [7]. The elementary particles carry electromagnetic charge except for the neutrinos, photons, gluons and Z^0-bosons.

Leptons			Quarks		
Flavour	Mass	Charge	Flavour	Mass	Charge
e^-	0.511 MeV	-e	up	1.5 - 3.3 MeV	$+\frac{2}{3}e$
ν_e	0	0	down	3.5 - 6.0 MeV	$-\frac{1}{3}e$
μ^-	105.658 MeV	-e	charm	$1.27^{+0.07}_{-0.11}$GeV	$+\frac{2}{3}e$
ν_μ	0	0	strange	104^{+26}_{-34} MeV	$-\frac{1}{3}e$
τ^-	1776.84 ± 0.17 MeV	-e	top	$171.2 \pm 2.1 \pm 1.3$ GeV	$+\frac{2}{3}e$
ν_τ	0	0	bottom	$4.20^{+0.17}_{-0.07}$ GeV	$-\frac{1}{3}e$

Table 2.1.: The three generations of fermions and their attributes [7]

mediator	charge	mass	force
photon	0	0	electromagnetic (electroweak)
gluon	0	0	strong
$W^\pm$	$\pm e$	80.398 ± 0.025 GeV	charged weak (electroweak)
Z^0	0	91.188 ± 0.002 GeV	neutral weak (electroweak)

Table 2.2.: Attributes of the bosons [7]

The strongly interacting particles, namely the quarks and gluons, carry colour charge in addition. For every particle introduced there exists a partner with the same mass but opposite charge. For example the antiparticle of the electron e^- is the positron e^+, for the top-quark t it is the anti-top quark $\bar{t}$ etc.

The interactions between elementary particles in annihilation or scattering processes are illustrated by Feynman diagrams. The orientation of the arrow of a particle graph to the time arrow distinguishes between particles and antiparticles, see figure 2.2.

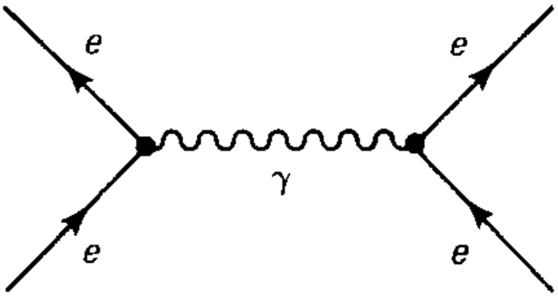

Figure 2.2.: Two incoming electrons are repulsed because of like charges: 'Møller scattering' (time bottom-up) [4].

The quarks are never observed as single isolated particles as they face colour confinement. Only colour-neutral hadrons, formed by quarks, can exist. Possible states are mesons (*colour, anti-colour*) and baryons (*rgb*). Protons ($|p> = |uud>$) and neutrons ($|n> = |udd>$) are each made out of three quarks and therefore constitute baryons. Colour confinement explains the effect of hadronization: when the distance between two quarks forming a meson increases, the energy between them rises until it is energetically more favourable to form two mesons [10].

2.2. Limitations of the Standard Model

The Standard Model is constructed as a consistent theory to describe the interactions between elementary particles. Although it is validated for many measurable effects there remain open questions. Most of all, it is expected to experimentally observe the Higgs boson at the LHC experiments as the energy scale achieved by the LHC opens up a promising range to search for the Higgs boson.
As already mentioned can the gravitational force not be included in the Standard Model. Another issue which can not be assembled in the Standard Model is the dark matter and the dark energy which make up most of the universe.

The values of the variables in the Standard Models like the masses of the fermions or the Higgs potential can be calculated with a finite number of at least 18 free parameters. The parameters themselves again have to be measured and there are attempts to make them theoretically predictable.
As indicated in figure 2.3, all three forces should be unified for very high energies. Both the electromagnetic and the weak coupling constants turn out to be running with q^2, too, but depend less strongly on it. When reaching the Planck scale M_P at about 10^{19} GeV, the gravitational interactions become comparable in magnitude despite their small coupling strength. The fact that there are so many scales between the masses of the W^+ and W^- bosons equal to 82 GeV and the Planck scale[2] is called gauge hierarchy [6].

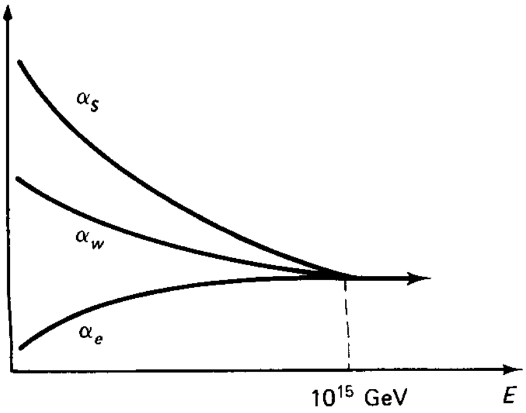

Figure 2.3.: Evolution of weak, electromagnetic and strong coupling constants with q^2 [4]

When looking at energy scales, a problem with the mass m_H of the Higgs boson occurs. The Higgs mass can acquire very high values due to corrections which may cancel accidentally via so-called fine-tuning. It is natural to choose the value of the cutoff in the same order of magnitude like the Planck scale. But then the quantum corrections to m_H^2 are 30 orders of magnitude larger than the expected value of the Higgs mass of roughly $\mathcal{O}(100\,\text{GeV})$. Again a new theory is needed in which the Higgs mass is calculable. I should not claim heavy fine-tuning to modify the Higgs mass in order to balance closed loops with virtual particles in Feynman diagrams [11].

---

[2] Or in other words the weak and electromagnetic force merging at $10^2 - 10^3$ GeV $\ll M_P$

2.3. Supersymmetry

2.3.1. Motivation

The above quantum corrections cancel each other systematically if a symmetry between fermions and bosons is assumed. This provides a solution to the hierarchy problem and the loop contributions to m_H^2 vanish. As pointed out in figures 2.4 and 2.5, the contribution of each fermion is cancelled by its bosonic superpartner.

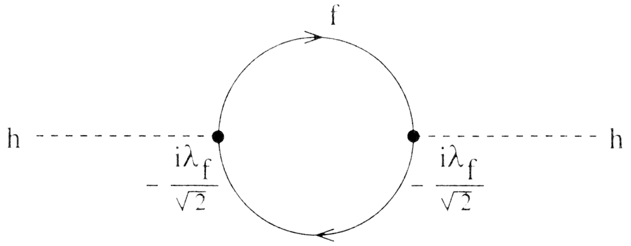

Figure 2.4.: Closed loop with virtual fermions contributing to m_H^2 [16]

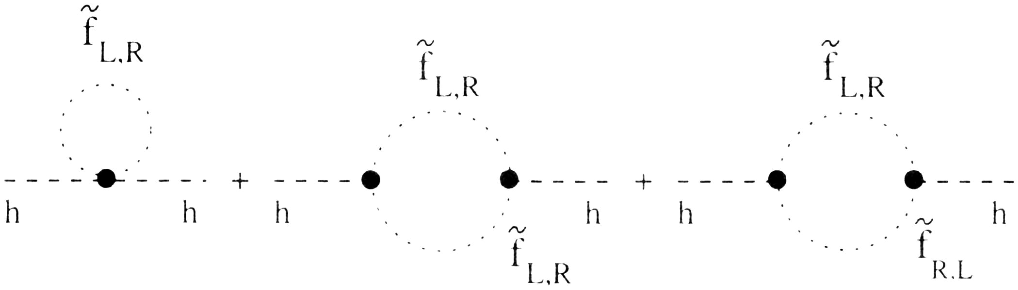

Figure 2.5.: Contribution to m_H^2 cancelled by sfermions [16]

Such symmetry can be attained by a transformation like

$$\hat{Q}|fermion>=|boson> \tag{2.11}$$

$$\hat{Q}|boson>=|fermion>\ . \tag{2.12}$$

The operator $\hat{Q}$ maps a fermionic state onto a bosonic state and vice versa. As the fermionic operators $\hat{Q}$ and $\hat{Q}^\dagger$ carry spin $\frac{1}{2}$, they generate a space-time symmetry in a non-trivial way. This contradicts the Coleman-Mandula theorem [6] which states that there can only be a trivial combination of space-time and internal symmetries [12]. Because the fermions transform differently concerning their chirality, the Haag-

Lopuszanski-Sohinus extension of [12] claims for $\hat{Q}$ and $\hat{Q}^\dagger$ to fulfil

$$\{\hat{Q}, \hat{Q}^\dagger\} = P^\mu, \tag{2.13}$$

$$\{\hat{Q}, \hat{Q}\} = \{\hat{Q}^\dagger, \hat{Q}^\dagger\} = 0 \tag{2.14}$$

and

$$[P^\mu, \hat{Q}] = [P^\mu, \hat{Q}^\dagger] = 0, \tag{2.15}$$

where P^μ is the four-momentum generator of spacetime translations. From equations (2.13) to (2.15) can be concluded that particles transformed by $\hat{Q}$ have equal masses and quantum numbers, e.g. electromagnetic charge, but different spin. Transformed particles are called superpartners and this framework is named **Su**per**sy**mmetry (SUSY).

2.3.2. The Minimal Supersymmetric Standard Model

Supersymmetry constitutes an extension to the Standard Model. Particles representing SUSY are clustered in supermultiplets where each supermultiplet contains as much fermions as bosons. Thus the spin quantum number of every superparticle (‘sparticle‘) differs by $\frac{1}{2}$ unit from the one of the Standard Model partner. Sparticles are indicated by a tilde. The superpartners of fermionic quarks and leptons are called squarks $\tilde{q}$ and

Supermultiplets	Boson fields	Fermionic partners	SU(3) (colour charge)	SU(2) (weak isospin)	U(1)(weak hyper charge)
gluon/gluino	g	$\tilde{g}$	8	0	0
gauge/gaugino	$W^\pm, W^0$	$\tilde{W}^\pm, \tilde{W}^0$	1	3	0
	B	$\tilde{B}$	1	1	0
slepton/lepton	$(\tilde{\nu}, \tilde{e}^-)_L$	$(\nu, e^-)_L$	1	2	-1
	$\tilde{e}_R^-$	e_R^-	1	1	-2
squark/quark	$(\tilde{u}_L, \tilde{d}_L)$	$(u, d)_L$	3	2	$\frac{1}{3}$
	$\tilde{u}_R$	u_R	3	1	$\frac{4}{3}$
	$\tilde{d}_R$	d_R	3	1	$-\frac{2}{3}$
Higgs/Higgsino	H_d^0, H_d^-	$\tilde{H}_d^0, \tilde{H}_d^-$	1	2	-1
	(H_u^+, H_u^0)	$(\tilde{H}_u^+, \tilde{H}_u^0)$	1	2	1

Table 2.3.: Attributes of the sparticles of MSSM [13]

sleptons $\tilde{l}$ (s for ‘scalar‘) and they have spin quantum numbers equal to 0. The superpartners of the gauge bosons have half-integer spins and are called gauginos [11]. For the attributes of binos, winos and gluinos see table 2.3. Zinos $\tilde{Z}^0$ and photinos $\tilde{\gamma}$ are mixtures of $\tilde{W}^0$ and $\tilde{B}^0$ after the electroweak symmetry breaking.

In the **m**inimal **S**upersymmetric extension of the **S**tandard **M**odel (MSSM) five Higgs bosons are predicted in the Higgs sector. One supermultiplet is not sufficient as the electroweak gauge symmetry would suffer a gauge anomaly. Two Higgs supermultiplets can be distinguished by the features of either giving masses to positively charged quarks like the up-quark or to negatively charged quarks like the down-quark and to leptons. They are named H_u and H_d, consisting of (H_u^+, H_u^0) and (H_d^0, H_d^-). The fifth Higgs field corresponds to the one of the Standard Model and is constructed by a linear combination of H_u^0 and H_d^0 [11].

Superpartners are supposed to have masses equal to the masses of their Standard Model siblings. The fact that they have not been observed so far is a clear hint for Supersymmetry being a broken symmetry. Spontaneous symmetry breaking happens when the ground state does not possess the symmetry of the basic equations which describe the system [6]. This breaking must occur in a soft manner what means that after the symmetry breaking the sparticles have somewhat higher masses than their superpartners. Otherwise the corrections to the m_H^2 parameter become very large and the hierarchy problem follows once again. SUSY breaking is probably assembled in a hidden sector containing neutral particles. These have almost no direct coupling to the MSSM particles and sparticles which provide the visible sector [13].

In the Standard Model the baryon number B and lepton number L are conserved in every interaction. In extended models this is not always assumed as some theories predict the decay of protons albeit with a very long lifetime [5]. A new quantity including the baryon number, the lepton number and the spin quantum number S is defined by

$$R = (-1)^{3(B-L)+2S}. \tag{2.16}$$

This is called R-parity. When plugging in the characteristics of the particles and sparticles it turns out that Standard Model particles have even R-parity while their superpartners have odd R-parity. If R-parity conservation at every interaction vertex is claimed in a SUSY model, there can be no mixing of particles and sparticles. Further consequences are

- that sparticles are produced in pairs when a Standard Model particle collision takes place,
- that every supersymmetric particle has to decay at some time into a state containing an odd number of stable sparticles and
- that the **l**ightest **S**upersymmetric **p**artner (LSP) is absolutely stable. It represents the final state for every heavier unstable sparticle in a decay chain.

In the supersymmetric particle sector of MSSM, mixing of gauginos and Higgsinos can take place. Four charginos $\tilde{\chi}_i^{\pm}$ (i = 1,2) can be constructed in this way by mixing charged Higgsinos $\tilde{H}_u^+$ and $\tilde{H}_d^-$ and charged winos $\tilde{W}^+$ and $\tilde{W}^-$. Mixing neutral Higgsinos $\tilde{H}_u^0$, $\tilde{H}_d^0$, $\tilde{B}$ and $\tilde{W}^0$ results in four physical states called neutralinos $\tilde{\chi}_i^0$ (i = 1, ..., 4). The lightest one ($\tilde{\chi}_1^0$) is often the LSP in a R-parity conserving model unless there is a lighter gravitino. For various assumptions about the relative values of the free parameters in the MSSM it can also nearly be a pure bino, a pure Higgsino or, together with the lightest chargino pair, a triplet of mass-degenerate pure winos [13].

Next to the effect of stabilizing the Higgs mass by solving the hierarchy problem, SUSY can provide an explanation to another outstanding issue. From astrophysical observations it came apparent that the speed of rotation of stars and clouds of interstellar medium stays too high in the outer regions of spiral galaxies. Also the kinematic movement of stars in dwarf galaxies or the mass of galaxy groups deduced from the effect of gravitational lenses can not be justified without assuming an additional mass which is composed by material not regarded so far. This material can only be made up by non-baryonic cold matter, so-called dark matter.

A good explanation for the dark matter would be **w**eakly **i**nteracting **m**assive **p**articles (WIMPs), for which SUSY can provide some candidates [14]. A model of the nucleosynthesis in the early universe considering Supersymmetry claims that there were heavy sparticles produced as long as the temperatures were sufficiently high. These decayed into LSPs which were created and annihilated until they froze out due to the decreasing available energy as the universe expanded. The possible candidates for both the LSP and dark matter are the lightest neutralinos, the gravitinos or - with some restrictions - the lightest sneutrinos [11].

The unification of the three coupling constants at energies $\mathcal{O}(10^{15}\,\text{GeV})$, shown in figure 2.6, is only an idle wish in the Standard Model. In reality the coupling constants behave more like shown in figure 2.6 (dashed line) and never meet in exactly one point. To this subject SUSY can provide a nice feature. The coupling constants must be recalculated and additional assumptions are included. Squarks and anti-squarks now also contribute with a colour factor of 3 to the running of the electromagnetic and the weak coupling constants. As a matter of fact the constants then merge exactly in one point at energies $\mathcal{O}(10^{16}\,\text{GeV})$ [16]. In figure 2.6 this is depicted by the continuous line.

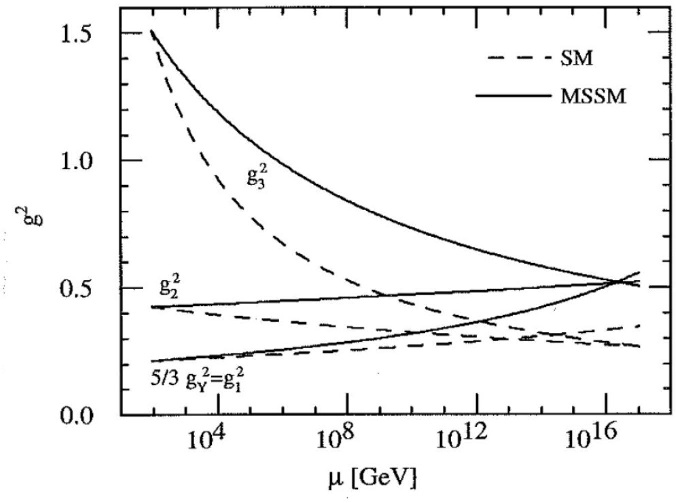

Figure 2.6.: Running of the squared coupling constants above the Z mass scale in the Standard Model (dashed line) and MSSM (continuous line) [16]

In SUSY the Higgs sector has eight degrees of freedom, three corresponding to the longitudinal degree of freedom of W^+, W^- and Z^0, and five are allocated to physical Higgs particles. This has of course consequences for the Higgs Mechanism, which causes the electroweak symmetry breaking in the Standard Model. The Higgs potential is changed accordingly and to achieve the symmetry breaking there are new constraints on e.g. the masses for H_u and H_d. The symmetry breaking can only be done by quantum corrections and that it must be a radiative electroweak symmetry breaking [11].

2.3.3. The Minimal Supergravity Model

The MSSM comprises 124 free parameters. This high number of parameters can be reduced very much by considerations upon phenomenological constraints like conservation of separate lepton numbers for the flavours muon, electron and tau, or charge and parity conservation. Models with assumptions on the breaking mechanism of SUSY can also lower the number of free parameters. An effort was made to do so in the **m**inimal **su**per**gra**vity model (mSUGRA). As implied by its name the breaking of SUSY is mediated by gravity in this framework. A boson with spin 2 is assumed for the gravity mediating graviton with its massive superpartner gravitino ($s = \frac{2}{3}$). In addition to the 19 Standard Model parameters now only

- the ratio of the vacuum expectation value for the neutral component of the Higgs fields H_u to H_d, $\frac{v_u}{v_d} = \tan\beta$,
- the universal sfermion masses m_0 at the GUT scale,
- the universal trilinear coupling A_0 at the GUT scale,
- the sign of the Higgsino mass parameter $sgn(\mu)$ and
- the universal gaugino mass $m_{3/2}$ at the GUT scale [15]

have to be determined. The number of parameters can be reduced to 23 because in mSUGRA it is assumed that the diagonal, soft-SUSY breaking scalar squared masses are universal at the Planck scale [13].

There are more theoretical frameworks based on SUSY, for example gauge-mediated SUSY breaking or R-parity violating SUSY. The fact that proton decay have not been observed limits the possibility of varying the assumptions of supersymmetric models.

2.4. Proton-Proton Collisions

For the experimental validation of theoretical frameworks physicists cause particle collisions at centre-of-mass energies close to temperatures which were prevalent in the early universe. Because of Einstein's simple law $E = mc^2$, high-energetic collisions can produce exotic particles. This makes the observation of interactions and final states possible which are so far only theoretically claimed. Next to the fixed- target experiments where a particle beam is aligned towards a fixed object, electrons or protons are accelerated and brought to interaction with each other in collision experiments. The advantage of storage rings over linear colliders is the accumulation of high energies as in every round the particles are accelerated one more time together with the high persistence of the beam.

The centre-of-mass energy E_{CM} can be calculated by the square root of the Mandelstam variable

$$s = (\hat{p}_1 + \hat{p}_2)^2 \tag{2.17}$$

with the four-momenta $\hat{p}_i = (E_i, p_{i1}, p_{i2}, p_{i3})$. The centre-of-mass energy simply becomes $E_{CM} = \sqrt{s} = 2E_i$ when the two colliding particles have both the same energy. The observer is put at rest in the centre of mass of the system [17].

The rate of collisions is expressed as luminosity. With the orbital frequency f, number of particle bunches in the storage ring n, number of particles in one bunch N and the cross-sectional area of the beams A this is

$$\mathcal{L} = \frac{fnN_1N_2}{A}. \tag{2.18}$$

Another characteristic variable to describe the interaction rate of a reaction is the cross-section σ. It is defined via the transition rate W per unit incident flux Φ per target particle of type b

$$\sigma = \frac{W}{\Phi} = \frac{W}{n_a v} \tag{2.19}$$

where n_a is the density of particles in the incident beam and v the relative velocity of target a and projectile particle b. The transition rate is given by Fermi's Golden Rule [18].

The decay products after the collision of two particles can be detected and reconstructed via their interactions with material. Effects like Čerenkov radiation, bremsstrahlung or deviation of charged particles in magnetic fields play a central role when looking for signals indicating new physics.

3. Experimental Setup

3.1. The Large Hadron Collider

The *European Organization for Nuclear Research* (CERN) is situated near Geneva, Switzerland, and is an international collaboration to maintain physical laboratories for elementary particle research. A tunnel between 45 and 170 m under the surface with a circumference of 26.7 km hosted the circular **L**arge **E**lectron **P**ositron collider (LEP) from the years 1989 until 2000. Then it became the **L**arge **H**adron **C**ollider (LHC). In contradistinction to an electron-positron collider, the proton-proton collider LHC can reach higher centre-of-mass energies. There are no limitations by synchrotron radiation: the mass reach of searches is then limited by the strength of the accelerating magnetic fields and the number of protons per bunch.

The largest experiments connected to the LHC are ATLAS[1], CMS[2], ALICE[3] and LHCb[4]. Each of them is a very large machine constructed from layers of detecting material and specialised on various physics topics. They are designed to perform at a centre-of-mass energy of $\sqrt{s} = 14\,\text{TeV}$ with a luminosity equal to $10^{34}\,\text{cm}^{-2}\text{s}^{-1}$. Until the end of 2012 the beam energy will be $E_i = 3.5\,\text{TeV}$, the upgrade to the designed performance with $\sqrt{s} = 14\,\text{TeV}$ is going to take place in 2013 - 2014.

For the collision of two particles which both carry positive charge, two separate magnetic dipole fields in two counter-rotating rings are needed. The protons are extracted from hydrogen gas and injected in the LHC ring after running through several smaller accelerators of the *Linac 2* injector chain. In figure 3.1 the sequence of the upgraded PSB[5], PS[6] and SPS[7] can be seen. In nominal configuration each proton beam consists of 2808 bunches with a bunch spacing of 25 ns. In August 2011 LHC was operated with

---

[1] ATLAS: **A** **T**oroidal **L**HC **A**paratus

[2] CMS:**C**ompact **M**uon **S**olenoid

[3] ALICE: **A** **L**arge **I**on **C**ollider **E**xperiment

[4] LHCb:**L**arge **H**adron **C**ollider **B**eauty experiment

[5] PSB: **P**roton **S**ynchrotron **B**ooster

[6] PS: **P**roton **S**ynchrotron

[7] SPS: **S**uper **P**roton **S**ynchrotron

a bunch spacing of 50 ns with 1380 bunches in a beam [23]. It is not possible to create a continuous particle beam due to the acceleration by fields which are alternating with high frequency [19].

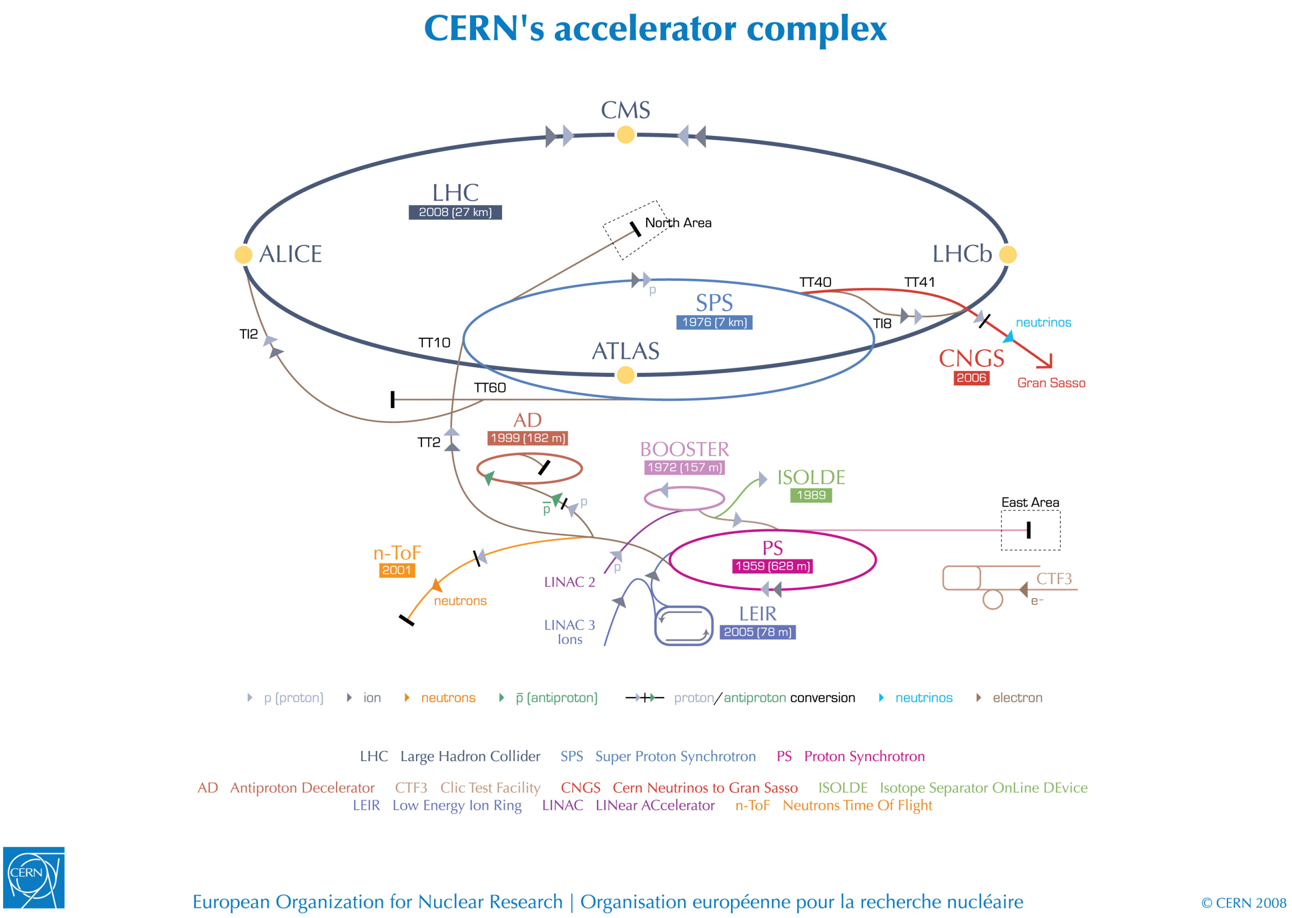

Figure 3.1.: The LHC injector chain [20]

3.2. ATLAS

One of the detectors at the LHC is **A** **T**oroidal **LHC** **A**pparatu**S** (ATLAS). A key issue of LHC is the investigation of electroweak symmetry breaking. As the Higgs boson is suspected of causing the symmetry breaking, its signal needs to be detected. Due to the theoretical Higgs-production chains this puts the following demands on the detector:

- precise (low) momentum measurements,
- possibility of tracking the particles,

- identification of electrons, photons, muons and hadrons and
- good coverage of the polar angle.

All features should be obtained with a high resolution [22].

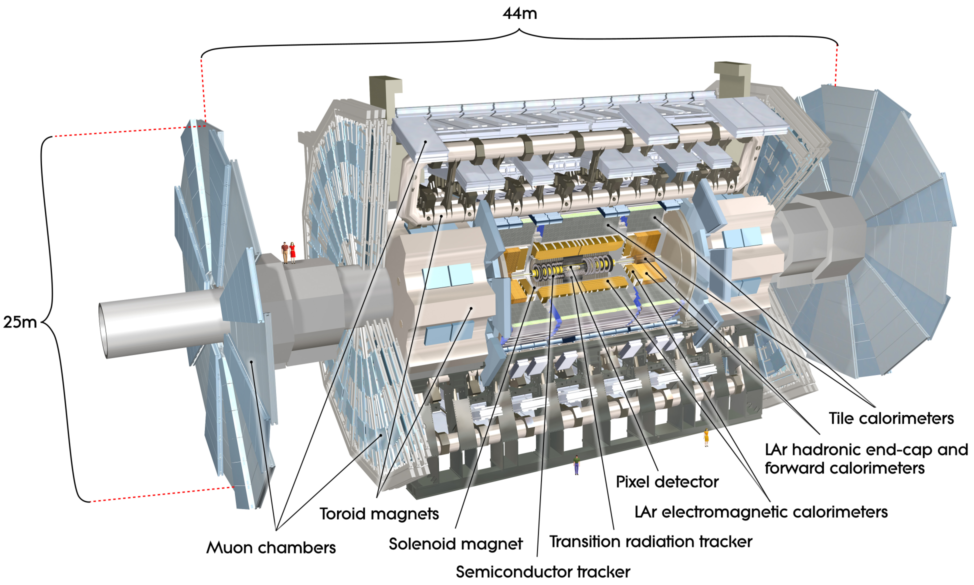

Figure 3.2.: Depiction of ATLAS [23]

ATLAS, which is also used to look for physics beyond the Standard Model, measures 44 m in lengths and 25 m in height [23] and is placed in a subterranean cavern. Its setup can be described by an onion skin structure. The back-and-forth symmetry is centred at the collision point of the two proton beams (see figure 3.2).

3.2.1. The ATLAS Coordinate System

The detector has a cylindrical shape along the beam axis and is laterally closed like a barrel. It is completed by end-caps on both ends. In a Cartesian right handed coordinate system the beam axis is allocated to the z-axis. The transverse plane is defined by the x-y plane. The polar angle is θ and around the z-axis the azimuth angle ϕ can be measured. The x-axis points from the point of collision to the centre of the LHC ring. The coordinate system is depicted in figure 3.3.

It is common to calculate the pseudorapidity η instead of using the polar angle itself [25]:

$$\eta = -\ln(\tan(\frac{\theta}{2})) \tag{3.1}$$

Some values for η and θ[8] are listed in table 3.1.

$\theta[^\circ]$	0	5	10	30	60	90	120	175	180
η	∞	3.13	2.44	1.32	0.55	0	-0.55	-3.13	$-\infty$

Table 3.1.: Pseudorapidity η corresponding to polar angle θ

When speaking about a transverse variable like transverse momentum p_T, this means the absolute value of the two-dimensional vector in the x-y plane

$$p_T = \sqrt{p_x^2 + p_y^2}. \tag{3.2}$$

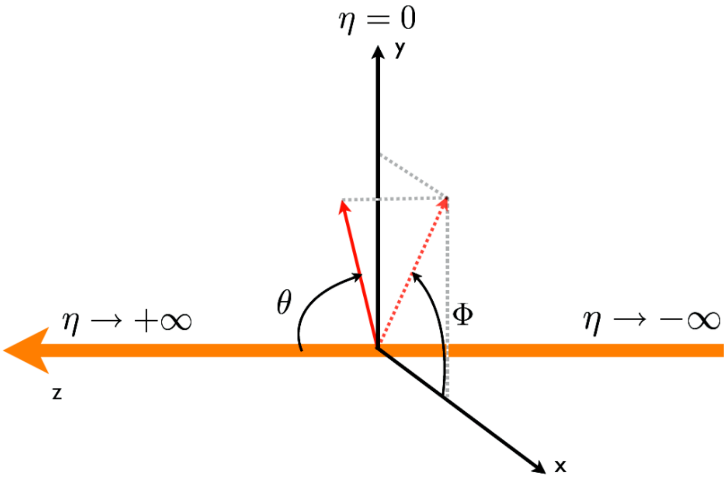

Figure 3.3.: ATLAS coordinate system [24]

The distance between detected objects will sometimes be given by

$$\Delta R = \sqrt{\Delta\phi^2 + \Delta\eta^2} \tag{3.3}$$

where ΔR defines the radius of a cone.

3.2.2. The Muon System

Starting with the outermost layer of ATLAS, this is the muon spectrometer. Muons do not interact strongly and carry more mass than electrons. Therefore they can be

---

[8] θ must be given in the unit radian for the calculation of η with equation (3.1).

detected without loss in the exterior subdetector as opposed to the other particles. The identification, charge measurement and momentum measurement of muons is based on the physical effect of the Lorentz force. Objects carrying the electromagnetic charge Q are diverted in a magnetic field $\vec{B}$ while moving with velocity $\vec{v}$. The acting force is given by

$$F_{Lorentz} = Q(\vec{v} \times \vec{B}) \tag{3.4}$$

The magnetic field is generated by toroids outside the barrel where each of the eight doughnut-shaped coils is fixed, see figure 3.4 (left). There are toroids at the end caps, too. The magnetic field strength is about 4 T [25].

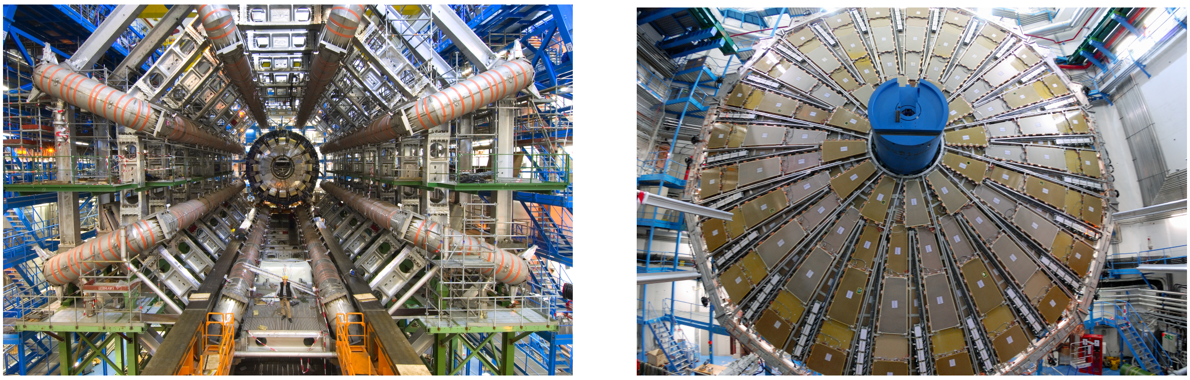

Figure 3.4.: Left: Photo of the coils creating the toroidal magnetic field. Right: TGC muon chamber for the end cap of ATLAS [23]

Four different kinds of muon chambers are used in the muon spectrometer:

- **mo**nitored **d**rift **t**ube chambers (MDT) consist of three to eight layers of drift tubes for precision momentum measurement in $|\eta| < 2.7$
- **c**athode **s**trip **c**hambers (CSC) in the forward region $(2 < |\eta| < 2.7)$ provide high rate capability and time resolution with multiwire proportional chambers.

Fast triggering on muon tracks for information about multiplicity and energy ranges in an early stage of the object reconstruction is possible by

- **r**esistive **p**late **c**hambers (RPC) in the barrel region $|\eta| < 1.05$ as gaseous parallel electrode-plate detectors and
- **t**hin **g**ap **c**hambers (TGC) in $1.05 < |\eta| < 2.4$ for the endcaps working with the same principle as multi-wire proportional chambers, see figure 3.4 (right).

The goal is to detect muons in a pseudorapidity range $|\eta| < 2.7$ with a high momentum resolution [25].

3.2.3. The Calorimeters

ATLAS combines hadronic and electromagnetic calorimeters to be optimally sensitive to the characteristics of the particles.

Very close to the beam there is a barrel cryostat containing an electromagnetic calorimeter in $0 < |\eta| < 1.475$ and each end cap cryostat hosts electromagnetic and hadronic calorimeters. Forward calorimeters cover the region of $3.1 < |\eta| < 4.9$. The locations of the calorimeters are shown in figure 3.5.

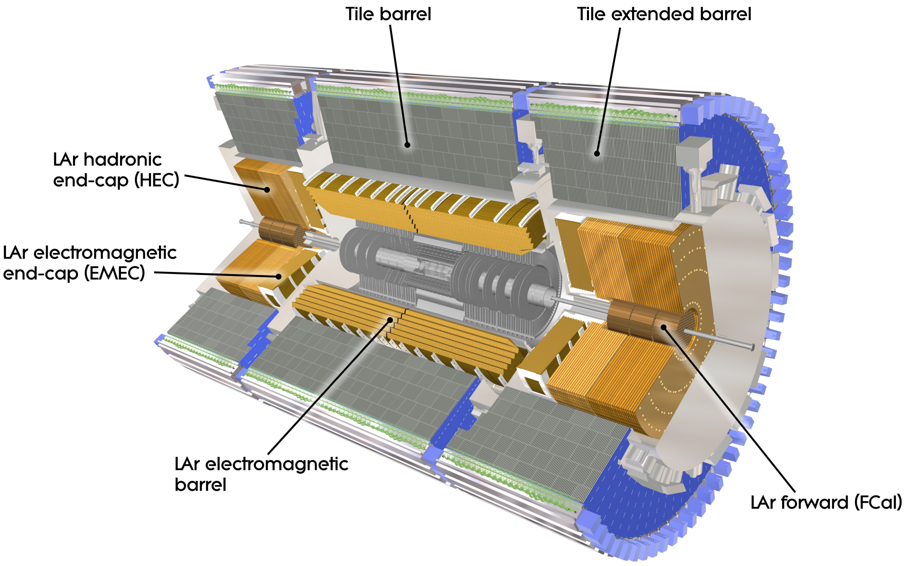

Figure 3.5.: Combined calorimeter of ATLAS [23]

The cryostats ensure low temperatures for the windings of the central solenoid needed for the Inner Detector. The solenoid and the electromagnetic calorimeter share a common vacuum vessel to minimize the material thickness in front of the calorimeters [25]. Due to bremsstrahlung and pair production, electromagnetic showers are initiated by a particle coming out of the proton-proton collisions. Accordion geometry is an excellent choice for the electromagnetic calorimeter because the signal is read out quickly and no information is lost in gaps. In the above calorimeter components the scintillating material is liquid argon. The energy of the showers is deposited in the calorimeter cells. The momentum and energy of a particle can be measured from the amount of lost energy in the calorimeter.

In the outer barrel regions, hadronic calorimeters consisting of scintillator tiles and absorbing material which is made out of steel are placed. These sampling detectors absorb and measure the energy in alternating layers as the strongly interacting hadrons can not be stopped in the scintillating material. They cover $|\eta| < 1.7$ [25].

Muons do not initiate showers but cause small signals in all layers of the calorimeters [26].

3.2.4. The Inner Detector

At the centre of ATLAS is the cylindrical **I**nner **D**etector (ID). The transverse momentum can be measured for tracks with $p_T > 0.5\,\mathrm{GeV}$. Primary and secondary vertices are resolved and electrons are identified. The solenoids around the Inner Detector provide a magnetic field of about 2.6 T [25]. Figure 3.6 shows a depiction of the ID.

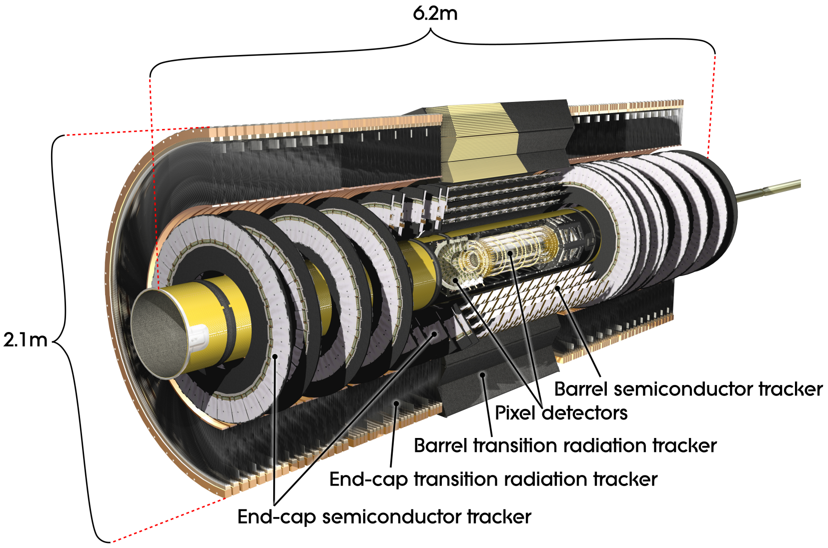

Figure 3.6.: The Inner Detector of ATLAS [23]

There are different subdetector components for various demands:

- a pixel detector in the very centre to provide two-dimensional spatial information for pattern recognition, next to a vertexing layer
- semiconducting silicon strip detectors for high precision tracking in the whole ϕ range constitute the **s**emi-**c**onductor **t**racker (SCT).

At larger radii of the Inner Detector is

- a straw tube system called **t**ransition **r**adiation **t**racker (TRT). Transition radiation in interleaved material can be used for improved electron identification ability when the track density is low. The momentum resolution of a particle is also further improved [25].

ATLAS recorded first collisions in March 2010 and has been reliably working since then. The analysis presented in this thesis is based on data recorded by ATLAS in the years of 2010 and 2011.

4. Particle Identification

4.1. Reconstruction of the Final State Particles

In this section the reconstruction of physical objects like jets consisting of many partons or leptons will be described; the objects leave marks in the detector. The goal is to reconstruct the particles emerging the proton-proton collision in the centre of ATLAS by putting together the information from the various subdetectors. Data can be matched to individual elementary particles like electrons, photons, muons, quark/gluon jets or τ-leptons.

4.1.1. Electrons

Electrons leave tracks in the ID and energy in the electromagnetic calorimeter but not in the hadronic calorimeter due to their physical attributes.

- A calorimeter tower is formed from all calorimeter cells in the η-ϕ-plane across the longitudinal layers, see figure 4.1. By adding up the energies which are deposited in neighbouring calorimeter cells, so-called pre-clusters are defined. The requirement on a pre-cluster is based on a threshold of the transverse energy E_T in a window consisting of calorimeter towers. In the window the deposited energy in a number of $N_\eta \times N_\phi$ grid elements is taken into account. The window ‘slides‘ over the tower grid. The positions of pre-clusters are defined by η and ϕ. After rejecting double-counted pre-clusters, the remaining clusters seed the final clusters in the following way: After their identification (see below) electron clusters are filled with calorimeter cells contained in a geometrical rectangle around the pre-cluster. The whole procedure is called *sliding-window algorithm* [27].

- Together with the information from the ID a track matching is performed. Good-quality tracks from the TRT are matched to the calorimeter clusters by looking at the η and ϕ distances and choosing the track with the smallest spacing to the cluster.

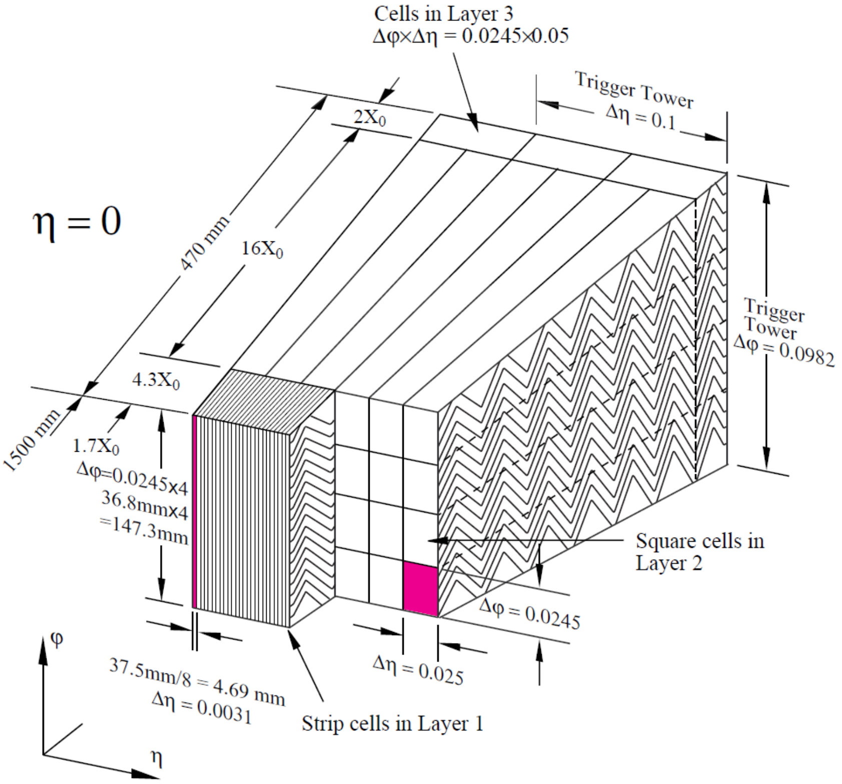

Figure 4.1.: Barrel calorimeter with 0.1·0.1 granularity in η-ϕ-plane and accordion geometry. The towers are also used by the trigger [25].

- Position corrections on η and ϕ of an electron candidate do not modify the global energy scale. They are needed due to variations of the calorimeter response or because of energy leaking outside the windows which define the pre-clusters [28].
- Energy reweighting is done by η-dependent longitudinal weights. They are established to optimise the energy resolution and the preferably linear response of the calorimeter. For example, energy is lost upstream of the presampler which provides shower sampling in front of the active electromagnetic calorimeter. Next to this effect longitudinal leakage is considered in the reweighting as well as an overall scale factor following from simulations [25].

An electron candidate from the calorimeter is loosely matched with a reconstructed track from the ID. The objects are then labelled according to their identification quality if they were detected in the trustworthy detector region with $|\eta| < 2.47$. The non-isolated electrons which have to be suppressed are mainly due to b- and c-hadron decays.

- Identification with **loose** quality: The electron is detected in a pseudorapidity range with $|\eta| < 2.5$. There is a cut on e.g. the ratio of E_T in the first sampling of the hadronic calorimeter over E_T in the electromagnetic calorimeter, or in general on shower shape variables.

- When an electron is identified with **medium** quality this means that, in addition to the loose quality criteria, further requirements are added. For example a cut on the strips in the first layer of the electromagnetic calorimeter is applied. Furthermore, the number of hits in the pixel detector or in the silicon are counted for requirements on the tracking. A cut on the transverse impact parameter is performed.

- For a **tight** electron, the main criteria in addition to the medium quality cuts concern the isolation of the object using all cell energies within $\Delta R < 0.2$ around the object. Among others hits in the vertexing-layer and in the TRT are required.

Electrons which are found in the forward region of the detector can only be reconstructed using information from the electromagnetic calorimeter. In particular the Inner Detector only covers the range within $|\eta| < 2.5$. This can be done by using just the clusters or carrying out a likelihood method [29].

A photon can be distinguished from an electron by looking for tracks which can be allocated to the calorimeter clusters. If it is not possible to match a track but a suitable photon conversion is found, the object is taken for a photon. If there is track matching, the clusters are allocated to an electron [25].

4.1.2. Jets

In a proton-proton collision coloured partons initiate clusters of hadronic particles due to hadronization and colour-confinement. The nearly cone-shaped objects are called jets [5]. They can be reconstructed by a variety of algorithms.

- The identification of jet candidates starts with topological clusters. Neighbouring cells in the calorimeters are grouped into three-dimensional clusters when they exceed an energy threshold. Thresholds can be adjusted separately depending on whether the cells belong to the same layer, the same calorimeter or anywhere across all calorimeters. Also, just a global energy threshold can be set or the threshold can depend on the relative value of the deposited energy in a cell compared to the neighbour cell. There are many ways to perform this algorithm [31].

- Other possibilities are for example the geometrical clustering where all cells around a seed position are included in the cluster defined by ΔR or the use of tracks as a seed [30].

In the analysis presented in this thesis, the definition of the jet objects is done by the *anti-k_T jet clustering algorithm*. For this reason it is briefly summarized in the following.

- The distances between so-called entities representing particles i and j or between a particle i and the beam B are calculated via

  $$d_{ij} = min(\frac{1}{k_{Ti}^2}, \frac{1}{k_{Tj}^2})\frac{\Delta_{ij}^2}{R^2} \tag{4.1}$$

  $$d_{iB} = \frac{1}{k_{Ti}^2} \tag{4.2}$$

  where $\Delta_{ij}^2 = (\eta_i - \eta_j)^2 + (\phi_i - \phi_j)^2$ defines a distance in the η-ϕ-plane, k_T is the transverse momentum and R is a radius parameter whose value is chosen to be e.g. 0.4. If the smallest of the distances is the one between two entities i and j, those are combined and the algorithm starts from scratch with this new entity. If it is the distance between an entity i and the beam, d_{iB}, the entity i is taken for a jet and won't be regarded any more in further iterations.
  Advantages of this algorithm are that first soft partons cluster with hard particles before clustering among themselves and that jets can not overlap. Moreover do soft particles not modify the shape of the jet [32]. For a visualisation, see figure 4.2.
  Another possibility for jet reconstruction is the cone algorithm, where a cone with radius ΔR is defined, whose axis must be aligned with the four-momentum of a high-p_T particle [34].

Due to gaps or dead material in the subdetectors next to Underlying Events or energy not included in the clusters used the final jets need to be calibrated. Another important issue is that the non-compensating calorimeter responds less to jets than to electrons. The jets can include many neutral particles whose significant amount of energy can not be detected with the calorimeters in contradiction to the electromagnetic showers. Jets therefore need to be corrected for their η-dependence, for non-linearity or for or the effect of magnetic fields on soft charged particles. The so-called **j**et **e**nergy **s**cale (JES) is figured out by comparisons to true jets when running the reconstruction algorithms

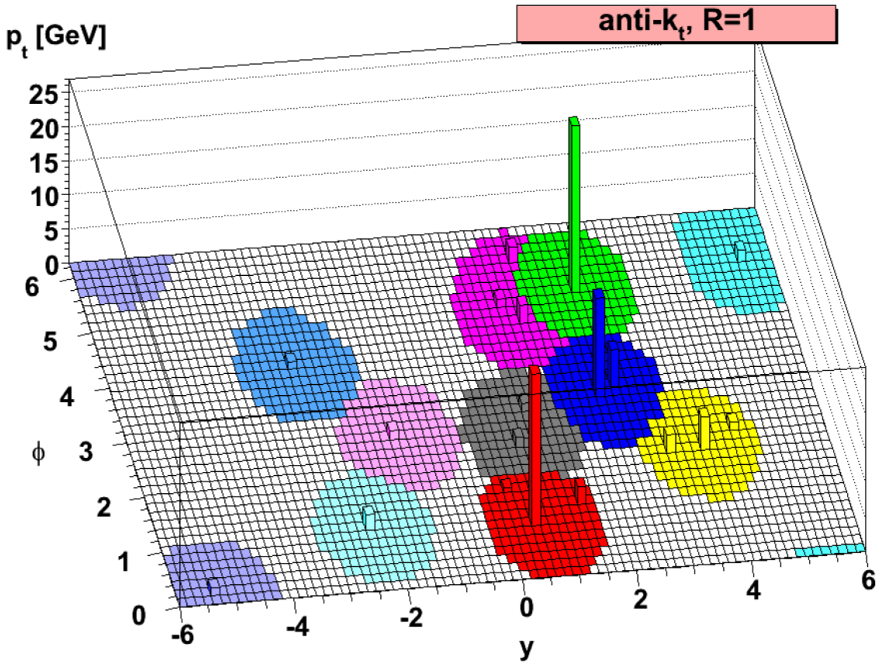

Figure 4.2.: A sample parton-level event illustrating the ‘active‘ draw areas of the resulting hard jets for the anti-k_T algorithm in the η-ϕ-plane. The z-axis indicates the p_T of the jet. Here is R equal to 1 [32].

on simulated data. Simulation of the calorimeters and of the fragmentation of the jets also contributes to the calibration. This is for example a crucial issue for calculating the inclusive jet cross section [36].

4.1.3. Muons

Muons in the final states after a proton-proton collision in ATLAS can be reconstructed by combining the information of the muon spectrometer which is sensitive to muons with $p_T > 3\,\text{GeV}$ and of the ID which is sensitive to low and intermediate p_T muons. The toroidal fields of the muon spectrometer provide a high momentum resolution. It is important to consider the alignment and calibration of the muon spectrometer and the Inner Detector [25].

- The stand-alone *Muonboy algorithm*, for which only information from the muon spectrometer is used, covers muons detected in $|\eta| < 2.7$. Regions of activity in the spectrometer are identified by the trigger chambers .

- The information of the Inner Detector and muon spectrometer is combined in the *STACO algorithm*. When fulfilling quality criteria the tracks in both subdetectors are formed to pairs of tracks with similar η and ϕ coordinates. The two independent measurements are then statistically combined . This algorithm can reconstruct muons with $|\eta| < 2.5$.

- The segment tag *MuTag algorithm* combines a track in the Inner Detector with a segment in the muon spectrometer on the basis of a ‘good‘ matching to improve the muon reconstruction by the *STACO algorithm*.

The *Muonboy* and the *STACO/MuTag algorithms* can lead to overlapping objects but the overlap is removed again when providing the datasets for analysis [37].
The algorithms make it possible to reconstruct muons in an energy range from 3 GeV to 3 TeV with a momentum resolution of 10% for 1 TeV tracks [25].

4.1.4. Missing Transverse Energy

The conservation of energy and momentum is one of the most important principles in physics. Of course this also must be valid in particle collisions. The total energy must be the same at all times if the system is closed. When calculating the total energy from the above introduced physical objects, it turns out that there can be energy missing. This was to be expected as there are physical objects which can not be seen in a detector. Neutral particles like neutrinos or supersymmetric neutralinos in the final states of decaying particles do not interact with the detector material. Their energies and momenta must be considered to obtain the conserved total energy. On the other hand the sum of the energy of all physical objects can be used to calculate the energy of the non-observable particles.
The transverse energy and momentum is defined by

$$E_T := \sqrt{E_x^2 + E_y^2} \tag{4.3}$$

and

$$p_T := \sqrt{p_x^2 + p_y^2}, \tag{4.4}$$

where p_x (E_x) and p_y (E_y) are the x- and y-components of the momentum (energy) vector. Analogously defined is the missing transverse energy

$$E_T^{miss} := \sqrt{(\sum_{all\,objects} E_x)^2 + (\sum_{all\,objects} E_y)^2} \tag{4.5}$$

or also noted as the negative vectorial sum

$$\vec{E}^{miss} = \begin{pmatrix} -\sum\limits_{all\,objects} E_x \\ -\sum\limits_{all\,objects} E_y \end{pmatrix} \quad . \tag{4.6}$$

Thus

$$\vec{E}^{miss} + \vec{E}^{all\,objects} = \vec{0}, \tag{4.7}$$

where

$$\vec{E}^{all\,objects} = \begin{pmatrix} \sum\limits_{all\,objects} E_x \\ \sum\limits_{all\,objects} E_y \end{pmatrix} \quad . \tag{4.8}$$

The deviation of reconstructed missing transverse energy from the true[1] E_T^{miss} is called fake E_T^{miss}. Main sources to these deviations are muons escaping in detector gaps, not read-out energy depositions in dead material, cracks or noise. Topological cuts are used to diminish these deviations [25].

Due to the various physical topics when analysing ATLAS data there are many different algorithms to calculate the missing transverse energy. Two of them will be introduced later in this thesis.

4.2. Data

4.2.1. Generation and Simulation

The use of simulated ATLAS data can be particularly useful for various studies. The events are first produced using an event generator; then also the according detector output is simulated.

The choice of the integrated luminosity and the centre-of-mass energy next to other input parameters like an assumed model for a physical effect starts the generation of a process like, for example $Z^0 \rightarrow e^+e^-$. Especially QCD processes can be of high complexity. Involved are, for example, higher order corrections, parton distribution functions, showering or hadronization [38].

Next to data driven methods, the signal can be extracted by comparing real data to simulated background processes. A special feature of simulated data is that, in addition

---

[1] see chapter 4.2.1

to the parameters of the reconstructed objects, it includes the true information about the objects based on the theoretical framework. The true parameters can be used to evaluate deviations and systematic errors resulting from the reconstruction algorithms.
To simulate the interaction of the particles of an event with matter, the toolkit *Geant 4* is used. Physical processes as well as detector simulation concerning geometry, tracking and detector response are considered in this software tool [39].
One example for a data generator is explained below as it produces data which is used in the analysis presented in this thesis. The generator is called *HERWIG* and as a special feature includes supersymmetric processes. Moreover, the production of Higgs bosons in the two-Higgs-doublet model, cascade decays of heavy particles according to input branching fractions and subprocesses which violate R-parity are considered. All MSSM particles and sparticles are taken into account. To derive probability amplitudes and cross sections, matrix elements are individually calculated for the different production mechanisms [40].

4.2.2. Pile Up

For each proton bunch crossing in ATLAS there are numerous collisions on top of any signal process. The detector does not have the ability to read out every single event on time since the detector response time is $\mathcal{O}(1\,\mu\mathrm{s})$ in the liquid argon calorimeters. As the signal needs more than $\sim 25\,\mathrm{ns}$ to be read out, this information piles up on the following bunch crossings.
Pile up is dominated by additional minimum bias collisions where partons of the colliding protons interact only very softly [41].
For increasing luminosity the pile up effect is no longer negligible. It is also simulated with *HERWIG* with various inputs for the average number of events for each bunch crossing.

4.2.3. Data Formats

The data files used for analysis are based on '**a**nalysis **o**bject **d**ata' (AOD). The chain of datafile configuration is shown in figure 4.3. Starting with the event generation and simulation, the artificial information is created about where a simulated particle is detected in ATLAS and what kind of signature it left. This again needs to be digitized to corresponding electronic signals like the ones read out of the detector for real events. Equally for real data this is the so-called RAW data in 'ByteStream' format. The RAW

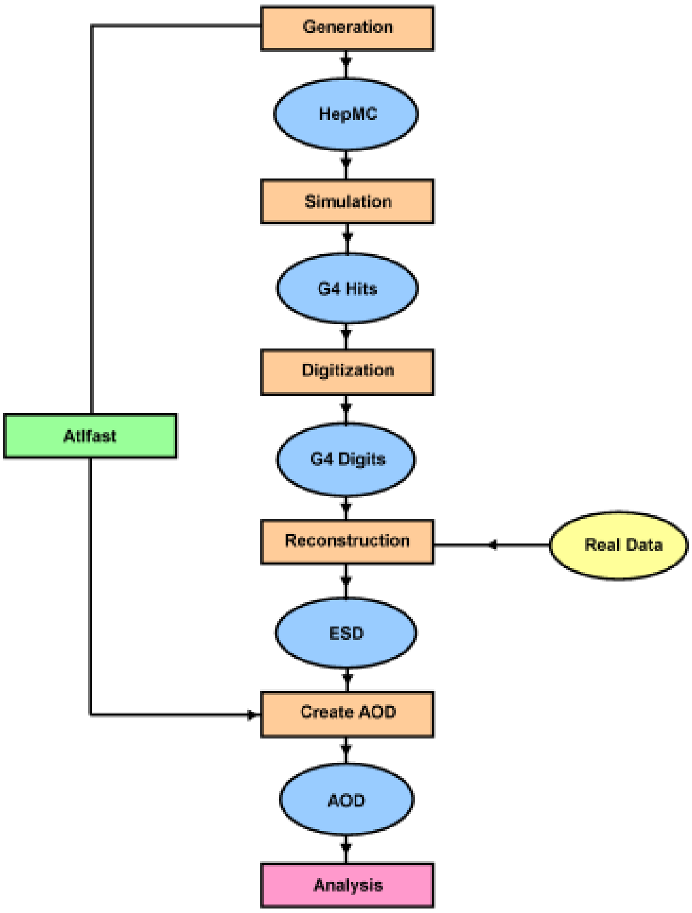

Figure 4.3.: Running the full chain [42]

data digits then are combined to tracks and energy deposits both for the real and the simulated data. The ‘**e**vent **s**ummary **d**ata‘ (ESD) is also the origin when - in the next step - the actual physical objects are reconstructed resulting in AOD. Further skimmed and slimmed data in respect of the analysed channel is called ‘**d**erived **p**hysics **d**ata‘ (DPD). The software framework that constitutes the skeleton for the application to run the chain of the above introduced data files is *Athena* based on the underlying architecture *Gaudi* [42].

Another framework for data processing, which is used in this thesis to analyse the DPD data, is *ROOT*. The data is saved, accessed and processed with this software. The plots shown in the analysis part of this thesis are histograms which are created with this tool [43].

5. Search for SUSY

To verify experimentally that Supersymmetry is indeed realized in nature as an extension to the Standard Model, and that it can provide solutions to the problems described in section 2.2, e.g. the hierarchy problem, sparticles must be detected.

5.1. Production of Sparticles

At the LHC, there are mainly two possibilities to produce coloured particles by a proton-proton collision.

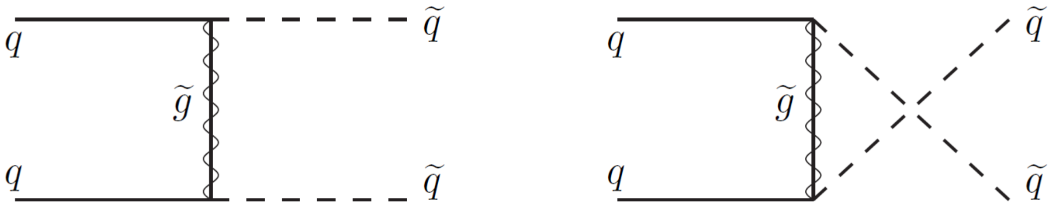

Figure 5.1.: Feynman diagrams showing squark production by quark-quark scattering with a time flow from left to right [11].

- Scattering of quarks and quarks produces squarks via the exchange of a gluino, see figure 5.1, and
- the fusion of gluons with gluons or gluons with quarks results in squarks and gluinos, see figure 5.2.

At the LHC, the production of strong interacting sparticles by fusion is dominating except for the case when gluinos and squarks have masses $>1\,\text{TeV}$ [11].

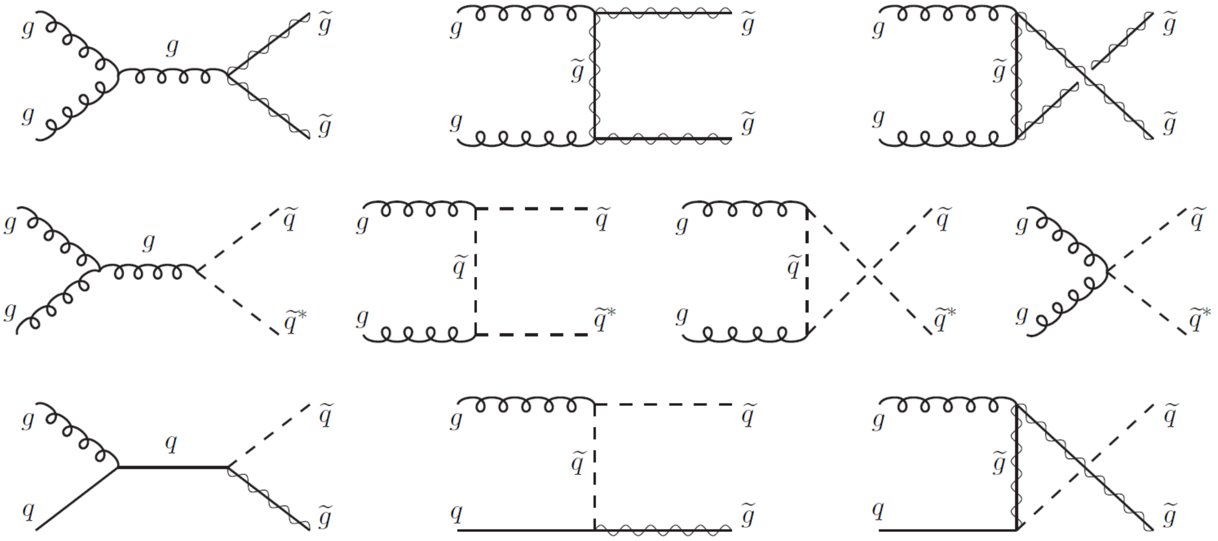

Figure 5.2.: Feynman diagrams showing gluino and squark production by gluon-gluon and gluon-quark fusion with a time flow from left to right [11].

5.2. Supersymmetric Signatures

The signal for supersymmetric events is categorized according to the number of leptons in the final state. Looking for example at figure 5.3, a gluino can be emitted after the proton-proton collision.

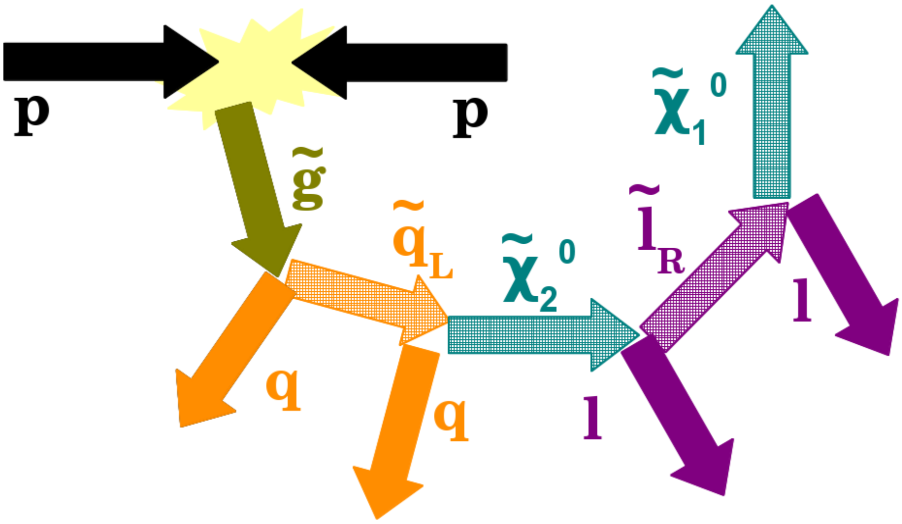

Figure 5.3.: Supersymmetric signal with two leptons in the final state after a gluino was emitted from the proton-proton collision.

It will decay until the final state contains a neutralino χ_1^0 as LSP, high-p_T jets initiated by quarks and several leptons. The analyses are classified in:

- Events with jets and E_T^{miss} without leptons (*0-lepton channel*): This is a very promising channel as it is sensitive to both the signal depicted in figure 5.3 when the leptons are badly reconstructed and other signals where the gluinos and squarks directly decay into jets and LSPs. The dominant Standard Model background are multijet events from the hadronic decays $W^- \to \bar{u}d$, $W^+ \to u\bar{d}$.

- Events with jets, E_T^{miss} and one lepton (*1-lepton channel*): Triggering on events containing one lepton in the final state is very reliable. Therefore the p_T thresholds for the jets can be lowered very much. These events have high background from W → lν processes.

- Events with jets, E_T^{miss} and two leptons (*2-lepton channel*): Here it is necessary to further distinguish between same-sign and opposite-sign leptons. A chargino in the decay chain of a squark of gluino can decay into a charged lepton, a neutrino and a neutralino. The sign of the charged lepton can be + or - with equal probability. Looking at the production of two gluinos by fusion this can lead to two same-sign leptons which do not have to have the same flavour. This signal has only very little Standard Model background.
  The supersymmetric processes resulting in two opposite-sign leptons have background from $W^-W^+ \to l^-\bar{\nu}l^+\nu$, Drell-Yan[1] and $t\bar{t}$-production ($t\bar{t} \to l^+\nu b l^-\bar{\nu}\bar{b}$).

- Events with jets, E_T^{miss} and at least three leptons (*multi-lepton channel*) can occur from fusion where one of the gluinos or squarks decays into a chargino and the other one into a neutralino. A main background to this channel is $Z^0 \to l^+l^-$ [11]. The *multi-lepton channel* can be more specialized if no jets are supposed in the final state.

To cut a long story short, it is all about looking for narrow high-p_T jets because of their large multiplicity in SUSY events, high E_T^{miss} and leptons with preferably high p_T. Up to now, no supersymmetric signal has been observed. Search results can therefore only be presented in terms of production cross section upper limits or of mass lower limits [15]. An example is given in figure 5.4 where the combined observed exclusion limits are shown for the mSUGRA parameters m_0 and $m_{1/2}$ while A_0, $\tan\beta$ and the sign

---

[1] a virtual photon or Z^0 decays into l^+l^- [4]

of μ are fixed. For this plot the analysis in the *0-lepton channel* with data corresponding to an integrated luminosity of $\int \mathcal{L}\,dt = 165\,\mathrm{pb}^{-1}$ was used[2] [51].

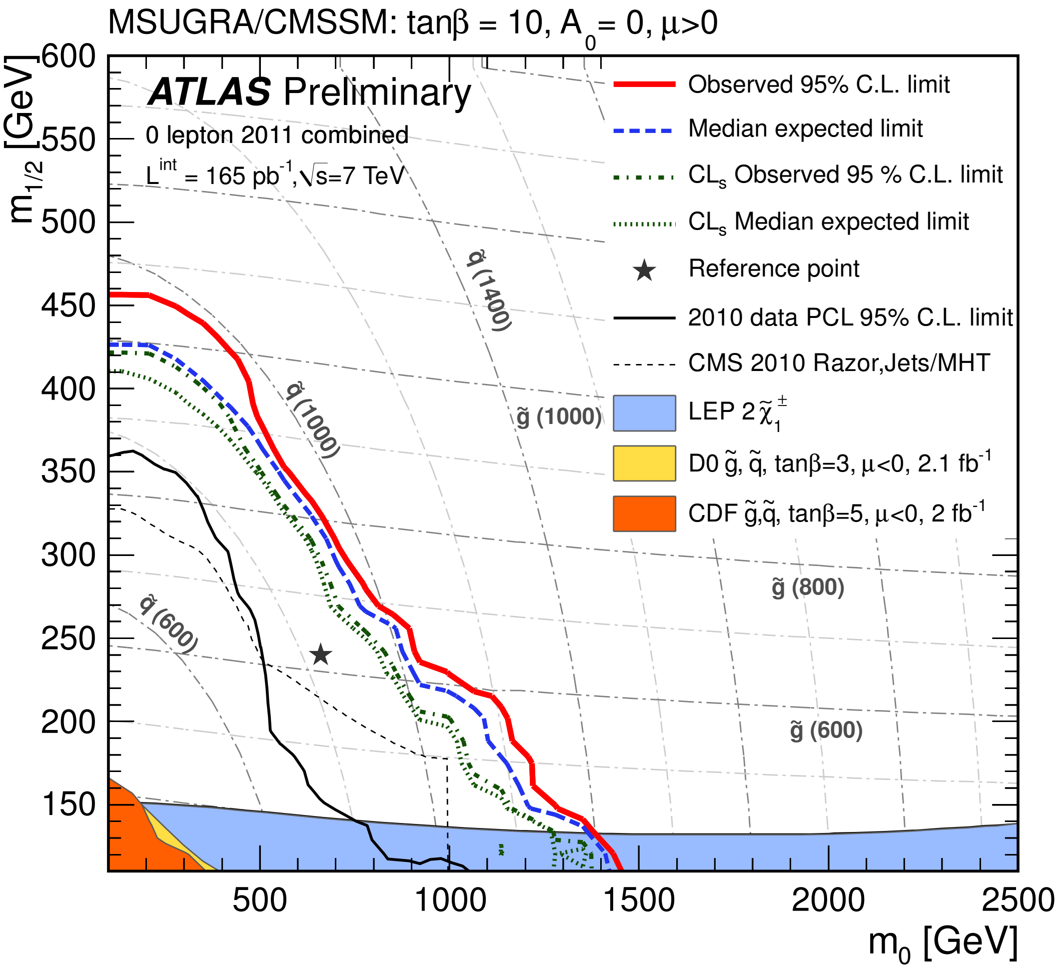

Figure 5.4.: Combined observed exclusion limits for m_0 and $m_{1/2}$. The dashed-blue line corresponds to the expected 95% CL limit, the red line corresponds to the observed limit at 95 % CL. Dot-dashed grey contours of constant gluino and squark mass are displayed at 200 GeV intervals [51].

---

[2] $1\ \mathrm{barn} = 10^{-28}\ \mathrm{m}^2$, $157\,\mathrm{pb}^{-1} = 157 \cdot 10^{36}\ \mathrm{cm}^{-2}$

6. Trigger System

6.1. Structure

In one proton bunch of LHC there can be up to $1.15{\cdot}10^{11}$ particles with a total hadronic cross-section of nearby $10^{-25}\,\mathrm{cm}^2$ [19]. When the LHC is running with its design luminosity, there will be $\mathcal{O}(10^7)$ particle collisions per second. This huge amount of data attained in the detector can not be stored. Thus there is the constraint to narrow down the choice. The solution is triggering on events which fulfil criteria making it probable that they are signal to new physics. The aim is to mainly reject the bulk of Standard Model QCD processes to become sensitive to interesting events with low cross-sections and to select them with high efficiency. If the trigger requirements are not strong enough, the event rate has to be prescaled by choosing randomly events which fulfil the requirements [44]. More than 99 % of the events will be rejected and are no more available for offline analysis.

The ATLAS trigger system is designed in order to limit the event rate to storable $\mathcal{O}(100\,\mathrm{Hz})$. Identifying physical objects, redefining their selection and cutting on their parameters like on transverse momentum or on missing transverse energy is done on three different trigger levels, see figure 6.1.
Starting with an initial bunch crossing rate of about 40 MHz this rate is stepwise reduced until all remaining data is of a dimension that can be stored.

6.1.1. Level 1

The first level (L1) of the trigger system is based on hardware. For calorimeter based triggers, longitudinal trigger towers are formed from the adjoining cells of the calorimeters with a granularity of 0.1×0.1 defined in the η-ϕ plane.
Triggering on jets on L1 means that an algorithm evaluates the deposited energy in jet elements consisting of 2×2 trigger towers. A jet element is included in a jet candidate if the transverse energy of the cluster is at a local maximum in a window of size

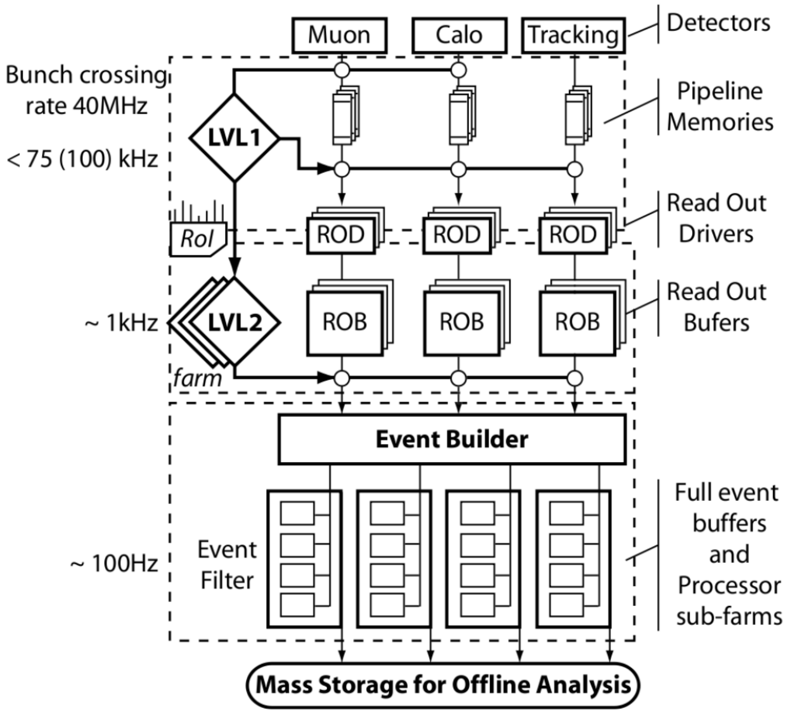

Figure 6.1.: The ATLAS trigger system [45]

$\Delta\eta \times \Delta\phi = 0.4\times0.4$. The jet candidate triggers if the deposited energy in 4×4 jet elements is above a given threshold like 5, 10, 20, 40, 70, 100, 130 or 150 GeV [46]. For a depiction see figure 6.2. The information about the location and the threshold energy of a jet candidate is passed to the next trigger level as a '**R**egion **o**f **I**nterest' (RoI).

To make a statement about the E_T^{miss} in an event, the vectorial sums of E_x and E_y of all jet elements are compared to a pass/fail table with a granularity of 1 GeV [47].

The time of deciding whether to keep or reject an event on L1 must be below 2.5 μs to pass an event rate of about 100 kHz to L2 [45].

6.1.2. Level 2

The **h**igh-**le**vel **t**rigger (HLT) is software based. Guided algorithms run in a stepwise manner to specify trigger hypotheses. Now the information from all subdetectors is available. L2 algorithms are seeded by the RoIs which are accepted from L1 and the appropriate data is demanded from the subdetectors. The use of RoIs limits the amount of requested data to 1-2 % of the total event size. Next to the redefinition of jet candidates the calorimeter shower shapes or tracks in the ID can be used for triggering [45].

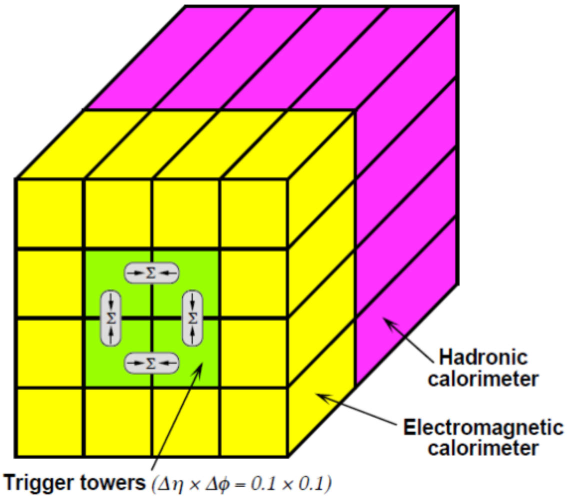

Figure 6.2.: Trigger towers in calorimeters. The green area corresponds to a window of size $\Delta\eta \times \Delta\phi = 0.4 \times 0.4$ [25]

Looking at the jets, a cone-shaped reference jet j_0 with a specified ΔR is defined at the RoI position. By calculating energy-weighted coordinates

$$\eta_{j1} = \frac{\sum_{i=1}^{n} E_i \eta_i}{\sum_{i=1}^{n} E_i} \tag{6.1}$$

and

$$\phi_{j1} = \frac{\sum_{i=1}^{n} E_i \phi_i}{\sum_{i=1}^{n} E_i} \tag{6.2}$$

and therefore using the energy and coordinates of the n grid elements inside the reference jet, a new jet j_1 is defined. This calculation is repeated for a fixed number of iterations. The resulting jets must then fulfil trigger requirements on their transverse momentum: For example at least one jet must have at least 7, 10, 15, ..., 200 GeV [46].

The information about missing transverse energy is seeded by L1 and could eventually be refined by running muon algorithms and including them in the calculation. At L2, $E_T^{miss} = \sqrt{E_x^2 + E_y^2}$ [48]. L2 has access to the entire event data with full detector granularity. Its algorithms need about 40 ms including data transfers and L2 may keep only 1 out of 100 events and pass it to the next trigger level not to exceed $\mathcal{O}(1\ \text{kHz})$ of event rate [44].

6.1.3. Event Filter Level

The **E**vent **F**ilter (EF) is in charge of further reducing the event rate to 200 Hz (400 Hz) in average which corresponds to $300\,\mathrm{MBs}^{-1}$. The EF is either seeded by RoIs received from L2 or makes a full scan of the complete data for every event. It provides a more refined analysis and uses very sophisticated algorithms which are comparable to the ones in the offline reconstruction due to its latency of about 4 s [44]. At the EF Level the events are classified into trigger streams like *JetTauEtmiss*, *Egamma* or *Muon*, according to which object triggered [45].
For triggering on E_T^{miss} a calorimeter cell will be included in the calculation if its energy exceeds $3 \cdot \sigma^1$. There is already object- dependent calibration [49].

6.2. Notation

In a trigger menu all trigger configurations are listed which ensure that not more than an event rate of 200 Hz or (in view of the increasing luminosity) even 400 Hz must be stored. Various slices depending on the trigger stream correspond to a fraction of the total bandwidth. A trigger signature puts demands on an event which is rejected if it does not accomplish them. The signature consists of requirements on the sort of the object being found in the event as well as on the p_T of the objects, the E_T^{miss} of the event and the information which is used to calculate these values.
The notation is

- ‘e‘ for an electron, ‘g‘ for a photon, ‘mu‘ for a muon, ‘j‘ for a jet, ‘tau‘ for a τ-lepton and ‘xe‘ for E_T^{miss}
- suffix ‘i‘ for an isolation requirement
- suffix ‘loose‘, ‘medium‘ or ‘tight‘ for the identification quality and
- a capital letter to indicate a L1 condition while small letters indicate a HLT requirement [44].

An example is the trigger *EF_e10_medium_mu6* which asks for at least one electron with $p_T \geq 10$ GeV which is identified with medium quality and for at least one muon with $p_T \geq 6$ GeV in an event on EF level. This would be seeded by the signature *EM5_MU0* in the first trigger level where the cluster in the electromagnetic calorimeter needs to

---

[1] σ: standard deviation from noise

have $p_T \geq 5\,\text{GeV}$ and there are yet no requirements on the demanded p_T of the muon. Luminosity blocks are subdivisions of a data-taking run and during a luminosity block the trigger menu is unchanged [44].

7. Efficiency Studies

The analysis in the *0-lepton channel* uses trigger signatures asking for minimum transverse momenta of the jets and missing transverse energy in an event. Recording data in 2010 was still possible in a commission mode - e.g. there was no need to run the jet algorithm at EF Level to achieve a storable event rate[1]. The peak luminosity in 2010 was only $2.1{\cdot}10^{32}\,\mathrm{cm}^{-2}\mathrm{s}^{-1}$, see figure 7.1.

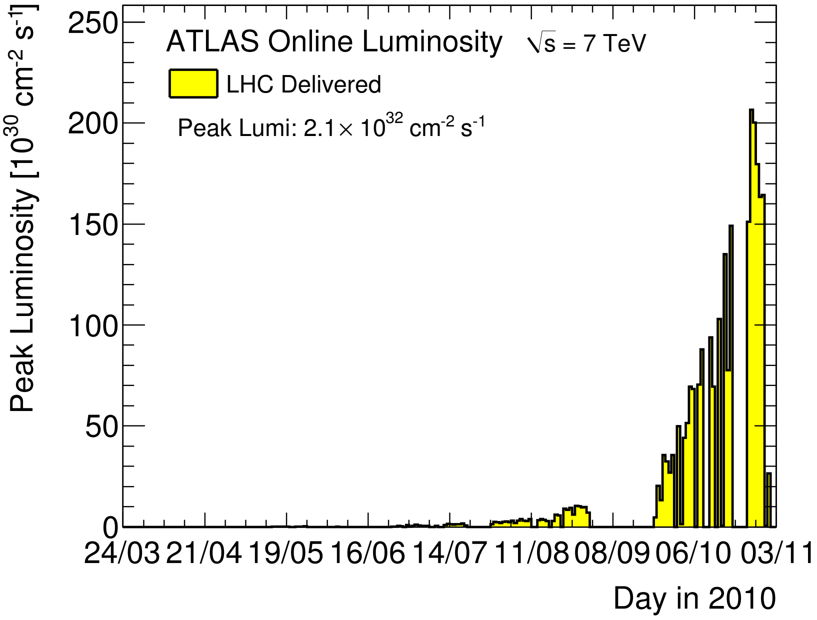

Figure 7.1.: Peak luminosity per day in the year 2010 [51]

For early data-taking runs in 2010 it was recommended to use *L2_j70* and *EF_xe25* in the analysis for which the jet threshold was seeded by *L1_J55*. For luminosities higher than $\sim 1.5{\cdot}10^{31}\mathrm{cm}^{-2}\mathrm{s}^{-1}$ the signature became *EF_j75_jetNoEF_EFxe25_noMu* [50].

In consideration of the further increasing luminosity there is the constraint to think of stronger trigger signatures to avoid prescaling. In August 2011 the peak luminosity already equalled $2.37{\cdot}10^{33}\,\mathrm{cm}^{-2}\mathrm{s}^{-1}$ [51]. In total a bandwidth of in average 200 Hz,

---

[1] The abbreviation for this circumstance is ‘jetNoEF‘ in the trigger signature variable.

maximally 600 Hz, for the data recording is available meaning that the data taking rate needs to be constrained by adjusting the trigger configurations. In doing so, the ultimate ambition is always not to loose signal for supersymmetric events.

7.1. Analysis in 0-Lepton Channel with 2011 Data

To search for supersymmetric events in ATLAS data, recommendations are concluded from many evaluations of the detector output. In the following, the Monte Carlo simulated SUSY signal is produced by *HERWIG* for the mSUGRA point *SU4*. *SU4* corresponds to a low mass point close to the Tevatron bound with $m_0 = 200$ GeV, $m_{1/2} = 160$ GeV, $A_0 = 0$, $tan\beta = 50$ and $\mu > 0$ [44]. Real data of period D of 2011 ATLAS data corresponding to an integrated luminosity of $\int \mathcal{L}\, dt = 157\,\mathrm{pb}^{-1}$ is also analysed. The data was skimmed by triggering on jets, τ-leptons[2] and E_T^{miss} resulting in the *JetTauEtmiss trigger stream*.

The following description of the event selection is taken from [52] and [53].

- In the analysis only luminosity blocks from ATLAS data taking periods, so-called runs, which are well understood and where the detector worked reliably are used. The SUSY good-run list version ‘DetStatus-v18-pro08-04‘ for 2011 ATLAS data is involved in this thesis.

- A special trigger signature must be fulfilled. For the *0-lepton channel* the recommendation is to ask for *EF_j75_a4tc_EFFS_xe45_loose_noMu*. There must be at least one jet with $p_T \geq 75$ GeV and at least 45 GeV of E_T^{miss} at EF Level. For computing E_T^{miss} no muons were included. The suffix ‘loose‘ means that the signature was seeded by *L1_J50_XE20* on the first trigger level. ‘EFFS‘ stands for ‘full scan at EF Level‘ while ‘a4tc‘ denotes that jet building based on geometrical tower-clustering was taken instead of the one which is based on topological clusters. The topological clustering was introduced later in jet triggers as it implies better robustness against pile-up.

- Events containing a ‘bad‘ jet are rejected. A bad jet is likely to not be initiated by the proton-proton collision but from spikes in the hadronic end caps, coherent noise in the electromagnetic calorimeter, cosmic rays or beam background. For

---

[2] Very massive τ-leptons have a small lifetime of $(290.6 \pm 1.0) \cdot 10^{-15}$ s [7] and decay mainly hadronically [10]; therefore they are triggered by jets.

this reason cuts are applied on energy fractions in the calorimeters, on timing information or on the ratio of the sum over all p_T of tracks associated to the jets over the calibrated jet p_t. This results in the identification of bad jets with loose (*0-lepton channel*), medium or tight quality [54].

- Only events are considered where the primary vertex has at least four good tracks to make sure that there was a collision.
- Beginning with run 180614 in period G of 2011 data, 6 **f**ront **e**nd **b**oards (FEBs) out of 1524 were lost. FEBs receive the RAW liquid-argon calorimeter signal and perform the analogue processing [25]. The outage causes lower jet response for jets pointing at this 'hole'[3] in the calorimeter. As a consequence for later runs events are no more analysed if (in the *0-lepton channel*) one of their four leading jets with $p_T > 40$ GeV is affected. Another solution is to consider a missing energy estimated using cell level correction based on neighbouring cells, and jet level correction based on Monte Carlo simulations [55].

Objects are selected from the electron, jet and muon containers of the DPD.

- Electrons must be reconstructed by the standard cluster-based algorithm with medium quality. Their transverse momentum must be larger than 20 GeV and they must be detected in a pseudorapidity range $|\eta| < 2.47$. Energy rescaling is applied. They may not touch a dead optical transmitter. Electrons not fulfilling these criteria are no more considered as leptons for the analysis.
- The *anti-k_T algorithm* was used on topological clusters to reconstruct jets with the radius variable $R = 0.4$. JES calibration was applied to jets reconstructed at electromagnetic scale. Further requirements on a jet are $p_T > 20$ GeV and $|\eta| < 2.8$ in order to be considered in the analysis. A jet is rejected if it overlaps with an electron. The overlap is defined by the cone variable $\Delta R < 0.2$ to describe the distance between both objects in the η-ϕ plane.
- Muons of loose reconstruction quality are selected with the *STACO* algorithm and thus need to be either a combination of tracks in the ID and the muon spectrometer or of a track in the ID associated with fragments in the muon spectrometer. On top of this cuts on momentum and pseudorapidity are recommended: $p_T > 20$ GeV and $|\eta| < 2.4$.

---

[3] A jet points at the hole if its coordinates lie in $-0.1 < \eta < 1.5$ and $-0.9 < \phi < -0.5$.

- *MET_Simplified20_RefFinal_et* is the missing transverse energy computation to be used in the *0-lepton channel* analysis. For this variable in every event the negative x and y components of the momenta of all selected objects are added. Energy scaled jets with $p_T > 20\,\text{GeV}$, medium electrons with $p_T > 10\,\text{GeV}$ and the above muons are considered. Clusters which are not allocated to these objects are included as ‘CellOut‘ term in the calculation. This formula summarizes the calculation:

$$\vec{E}^{miss} = \begin{pmatrix} E_x^{miss} \\ E_y^{miss} \end{pmatrix} = \begin{pmatrix} -\sum\limits_{sel.\,jets} p_x - \sum\limits_{sel.\,electrons} p_x - \sum\limits_{sel.\,muons} p_x - \sum\limits_{CellOut} p_x \\ -\sum\limits_{sel.\,jets} p_y - \sum\limits_{sel.\,electrons} p_y - \sum\limits_{sel.\,muons} p_y - \sum\limits_{CellOut} p_y \end{pmatrix} \tag{7.1}$$

$E_T^{miss} = \sqrt{(E_x^{miss})^2 + (E_y^{miss})^2}$.

Leptons are vetoed if they overlap with a jet by $\Delta R < 0.4$ as it is probable that these leptons exist due to a decay inside the jet.
The recommendations minimize the loss of signal but suppress fake objects, noise and Standard Model background.

When analysing Monte Carlo simulated data some criteria are not applied: Bad jets are not included and there is nothing like good run lists for MC data. Apart from that, electron energy is smeared to reproduce the non-optimal energy resolution and the non-linear detector response. The same applies to the p_T of muons. If the muons are not vetoed in the further analysis, events containing muons also need to be weighted according to the reconstruction efficiency of these objects.

In the *0-lepton channel* analysis all events still containing leptons after the object selection are rejected.

7.2. Trigger Studies

7.2.1. Introduction of Turn-on Curves

The efficiency ϵ when asking for the trigger *EF_j75_a4tc_EFFS_xe45_loose_noMu* can be calculated for each bin of the p_T distribution of the leading jets or the E_T^{miss} distribution. The number of events passing this requirement is divided by the number of all events. Plotting the efficiency results in a so-called turn-on curve for the variable on the x-axis which is e.g. the p_T of the leading jets or E_T^{miss}. The shape of the turn-on curve allows to make statements about the correlation of the involved variables. To get this information at a glance, the turn-on curve is fit with the following equation which describes the shape of the curve very well:

$$f(x, p_0, p_1, p_2) = \frac{p_0}{1 + 81^{\frac{p_1 - x}{p_2}}} \tag{7.2}$$

The number 81 in the denominator makes it possible to obtain the characteristics of the shape of the curve from the fitting parameters. The parameter p_0 states the value of the efficiency where the plateau levels off. The x-value for which the efficiency reaches the half of the plateau is given by p_1. The Δx corresponding to the rise of the efficiency from 10 % to 90 % of the plateau is indicated by p_2.
In figure 7.2 the efficiency when asking for *EF_xe70_noMu* is shown with E_T^{miss} at EF Level on the x-axis.

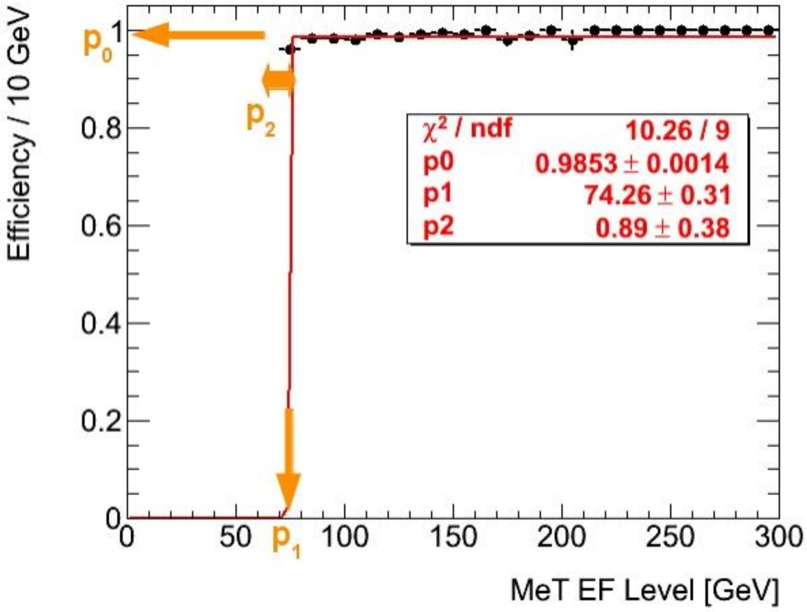

Figure 7.2.: Turn-on curve for *EF_xe70_noMu* with E_T^{miss} at EF Level on the x-axis. The statistic box shows the fitting parameters.

The E_T^{miss} is calculated without muons. This plot serves as an example for the fit which is done by the red line. For the turn-on curve in figure 7.2 this means that the plateau is at 99 %, ∼ 50 % are reached for $E_T^{miss} \approx 74$ GeV and the efficiency rises in the region from

~ 73 GeV to ~ 74 GeV. The sudden rise of the turn-on curve at almost the same value which the trigger uses for cutting expresses a very strong, almost perfect correlation of the variable on the x-axis and the variable used for triggering. The values for the fit parameters are also shown in the statistic box of the plot.

This generic, almost ‘ideal‘ turn-on curve is shown to introduce the method of deducing information about the correlation of the variable shown on the x-axis and the variable the trigger uses to cut on.

The parameter $x_{plateau}$ indicates for which x-value the curve begins the plateau. It is customary to make a recommendation for only using an event in the analysis if the x-axis variable of this event is higher than $x_{plateau}$. Events are therefore also rejected in the *0-lepton channel* if the p_T of the leading jet is smaller than 130 GeV and if the missing transverse energy is smaller than 130 GeV. The leading jet is the jet with the highest transverse momentum. This is motivated in the plots shown in figure 7.3 for the p_T.
The *Muon stream*[4] in real data is used and $E_T^{miss} > 130$ GeV is required. For E_T^{miss} the *MET_LocHadTopo_et* algorithm is picked - it uses the cells in the topological clusters and a local hadronic calibration is applied [52]. No muons enter the computation of *MET_LocHadTopo_et. EF_j75_a4tc_EFFS* is the sample trigger for the denominator when computing the efficiencies.

$$\epsilon = \frac{N\,events\,passing\,EF\_j75\_a4tc\_EFFS\_xe45\_loose\_noMu}{N\,events\;passing\,EF\_j75\_a4tc\_EFFS} \tag{7.3}$$

In this turn-on curve, the plateau is reached at $\epsilon = 99\,\%$, the half of the plateau is reached for $p_T = 107$ GeV and the p_2 fit parameter equals 18 GeV.

The plot in figure 7.4 shows the efficiency for $E_T^{miss} =$ *MET_Simplified20_RefFinal_et* in the *JetTauEtmiss stream* when the p_T of the leading jet exceeds 130 GeV.

$$\epsilon = \frac{N\,events\,passing\,EF\_j75\_a4tc\_EFFS\_xe45\_loose\_noMu}{N\,events\;before\;triggering} \tag{7.4}$$

This time the plateau is reached for $\epsilon = p_0 = 100\%$, p_1 equals 63 GeV and the rise is slower, which is also indicated by $p_2 = 45$ GeV.

---

[4] The corresponding trigger signature is *EF_mu18*: the muon must have at least 18 GeV of transverse momentum at EF level.

Looking at the plots 7.3 and 7.4 the plateau begins both times at $x_{plateau} \approx 130\,\mathrm{GeV}$, illustrated by the vertical blue lines.

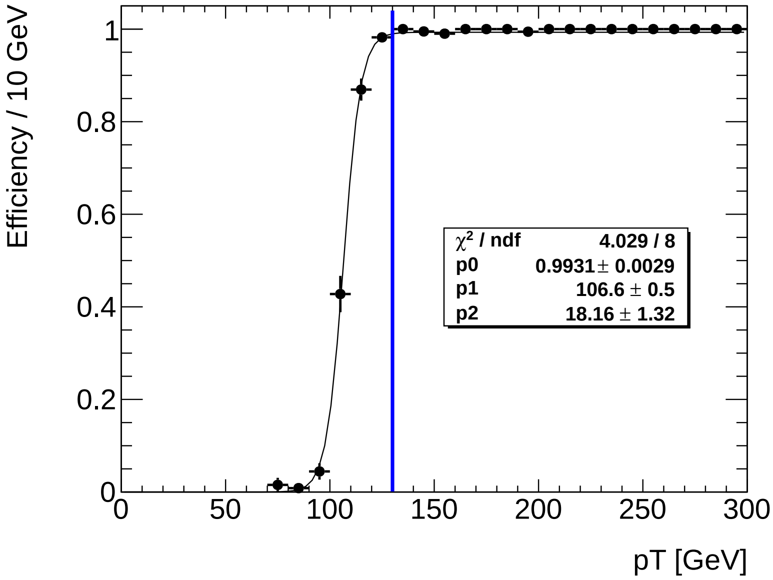

Figure 7.3.: Efficiency for *EF_j75_a4tc_EFFS_xe45_loose_noMu*. The leading jet p_T is shown on the x-axis for real data. The vertical blue line illustrates at which x- value the plateau begins.

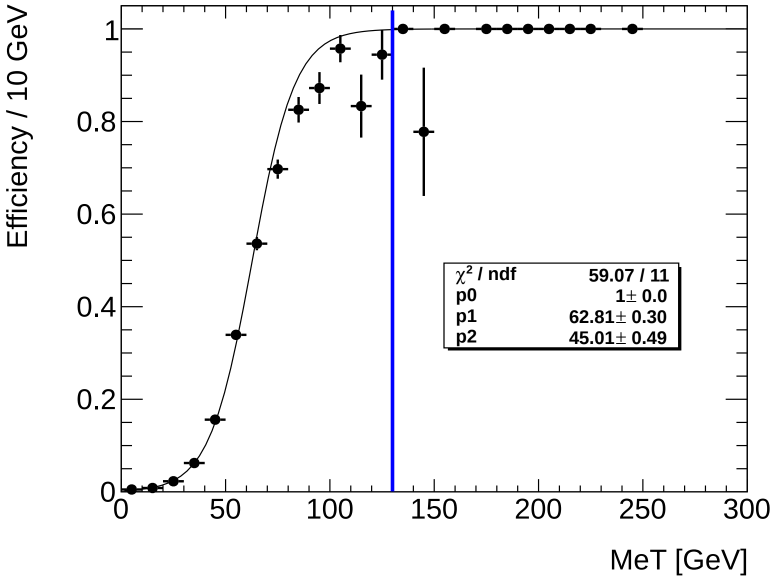

Figure 7.4.: Efficiency for *EF_j75_a4tc_EFFS_xe45_loose_noMu*. *MET_Simplified20_RefFinal_et* is shown on the x-axis for real data. The vertical blue line illustrates at which x-value the plateau begins.

7.2.2. Agreement of Online and Offline Variables

For the trigger signature *EF_jXX* a cut on the offline jet p_T will be performed in the following study and instead of the EF $|\eta|$ the offline $|\eta|$ will be shown since the EF and offline jet algorithms are very similar. The jet variables on EF Level are not stored in the DPD.

A check on the agreement of the online and offline variables seems reasonable to assure that cutting on the online p_T and $|\eta|$ of the leading jet and on online E_T^{miss} is trustworthy. The correlation of the leading offline jet p_T and the leading L2 jet p_T is shown on the left-hand side in figure 7.5 for real data. The correlation of the according pseudorapidities is shown on the right-hand side. Both distributions feature strong correlation thus the use of online jet variables for triggering is reliable. The plots for MC simulated data can be found in figure B.1 in the appendix. The simulated online and offline jet variables are also very similar.

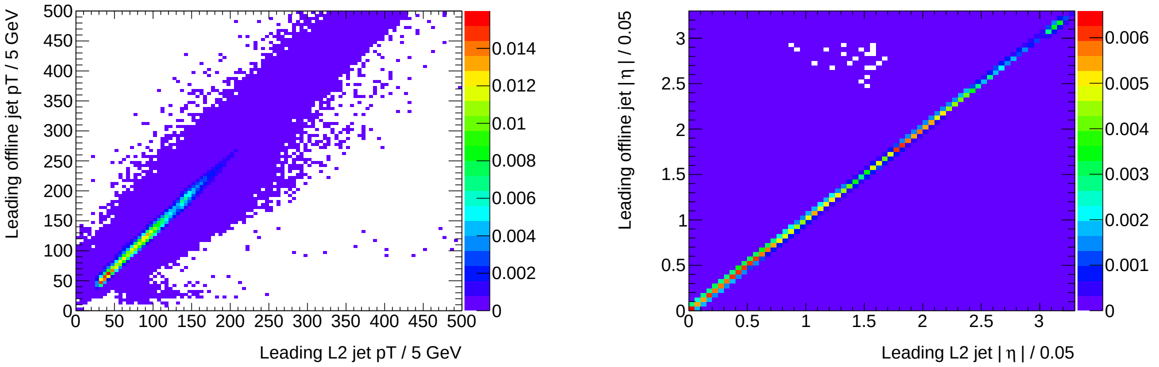

Figure 7.5.: Real data: Distribution of the leading L2 jet p_T versus leading offline jet p_T (left) and distribution of the according $|\eta|$ variables (right). Both distributions are normalized to 1.

The requirements on E_T^{miss} have to be fulfilled on EF Level. A check on the correlation of the E_T^{miss} on EF Level versus E_T^{miss} offline (*MET_Simplified20_RefFinal_et*) is shown in figure 7.6 for MC simulated data. Both E_T^{miss} variables are computed not including muons and are definitely correlated - therefore the requirement on E_T^{miss} on EF level can be seen as an analogue requirement on offline E_T^{miss}. This is valid for both Monte Carlo simulated signal and real data. The plot for real data can be found in figure B.2 in the appendix where the correlation is also visible. Some values are indeed very different, e.g. in the right lower region of the plot in B.2. This observation will be elaborated in chapter 8.

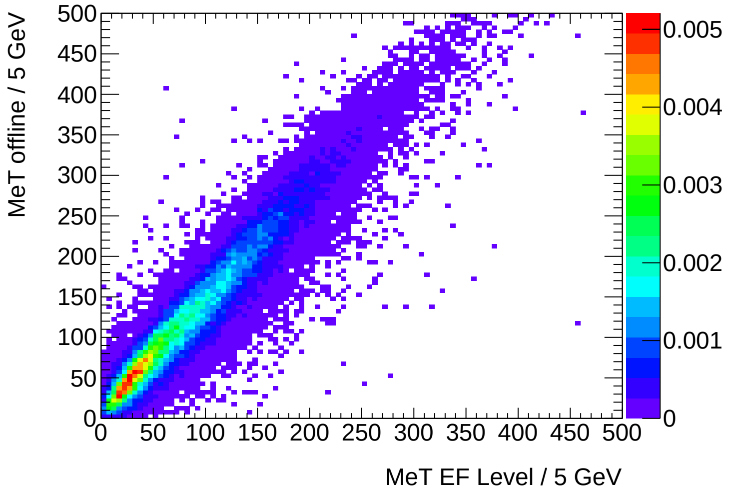

Figure 7.6.: MC simulated signal: Distribution of E_T^{miss} at EF Level versus E_T^{miss} offline (*MET_Simplified20_RefFinal_et*). The distribution is normalized to 1.

7.2.3. Centrality of the Supersymmetric Signal

Looking at characteristic parameters of the final state particles in a supersymmetric event, one thing attracts attention.

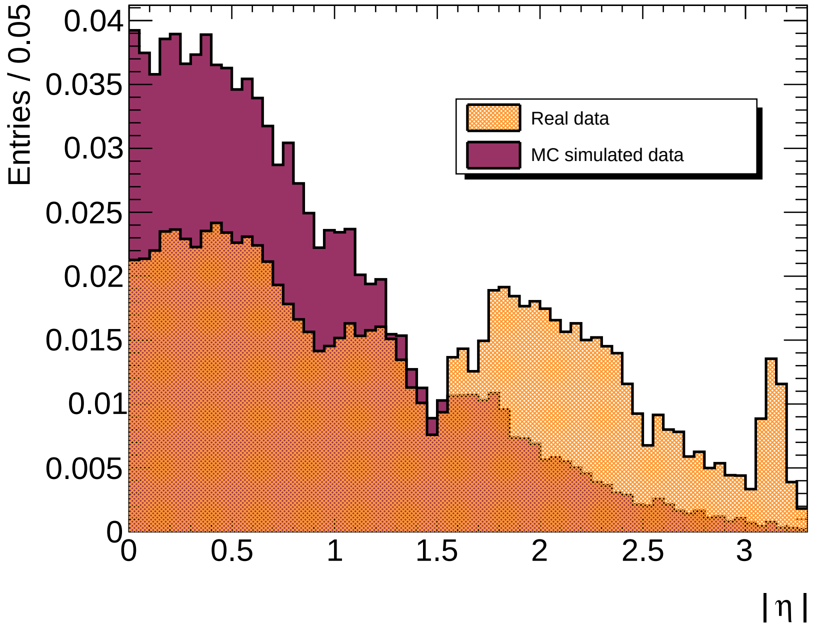

Figure 7.7.: Distribution of the absolute value of the pseudorapidity of the leading L2 jets for real data (orange) and MC simulated *SU4* signal (purple). The distributions are each normalized to 1.

The plot in figure 7.7 shows the distribution of the absolute value of the pseudorapidity $|\eta|$ of the leading jet in every event both for simulated supersymmetric signal (SU4) (purple) and real data (orange). It strikes the eye that the leading jets in supersymmetric events very often point at right angle to the beam axis which corresponds to rather small $|\eta|$ values. This is quite contrary to the real data events containing mostly Standard Model background where the $|\eta|$ of the leading jet is more isotropic. This establishes the idea of cutting on the pseudorapidity of jets to decrease the data rate and to preserve a high efficiency for SUSY signal at the same time.

The 2011 trigger baseline contains the signature *EF_j75_xe45* and one of the ways considered to control the rate at higher luminosity would be to rise the E_T^{miss} threshold from 45 GeV to 55 GeV or even 60 GeV while the p_T of the leading jet must be > 75 GeV. This is the starting point for an evaluation of the behaviour of the data rates and the trigger efficiencies when putting demands on the pseudorapidity of one or two jets in an event.

7.2.3.1. Stepwise Pseudorapidity at Trigger Level 1

At the first trigger level the pseudorapidity is computed only in a stepwise manner.

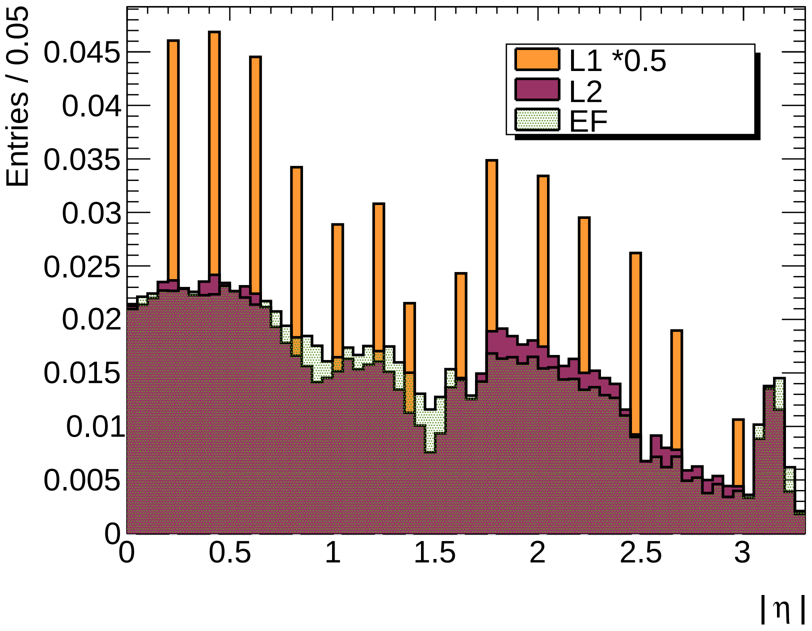

Figure 7.8.: Distribution of $|\eta|$ for leading jets on L1 (orange), L2 (purple) and offline (green) (= EF). The distributions are normalized to 1.

Figure 7.8 shows the $|\eta|$ distribution of the leading jets at L1 (orange), L2 (purple) and EF (green) (= offline) in real data.

At L2 and EF Level some peaks at $|\eta| \approx 0.5$, 1.2, 1.9 and 2.6 are still noticeable which run parallel to the entries of the L1 $|\eta|$ distribution. Those peaks are probably due to the fact that the pseudorapidity of the L1 jets is simply adopted for L2 jets without recalculation. The shape of the $|\eta|$ distribution depends in general from geometrical aspects, detector resolution and jet calibration.

7.2.3.2. Baseline Trigger Signature

The requirement on $|\eta|$ can not be implemented at the first trigger level due to technical reasons because only badly resolved, discrete values of η are available. To decrease the trigger rate, the pseudorapidity of the leading jet at L2 can however be used; it is required to be in some special range. It is reasonable to only let events pass where the leading L2 jet fulfils $p_T > 75\,\text{GeV}$ and $|\eta| < 2.7$, $|\eta| < 2.2$, $|\eta| < 1.7$, $|\eta| < 1.2$ and $|\eta| < 1.0$. As *EF_j75* is seeded by *L2_j70* and *L1_J50*, an event has to pass all these trigger signatures and there must be no prescaling before evaluating the value of $|\eta|$ at L2. Because of the possibility of changing the *EF_xe* criterion this option will be checked in addition, resulting in the trigger chains *L1_J50_L2_j70_*$|\eta|$*xx_EF_j75_xeXX* where xx denotes the upper value of the absolute value of the pseudorapidity of a jet and XX the minimum value of E_T^{miss}.

In the following centrality study no preselections except for asking for good runs in the *JetTauEtmiss stream* of real data and applying the introduced trigger signatures are performed as the data rate would include all events.

The number of events passing the above trigger is compared to the number of events passing *EF_j75_a4tc_EFFS_jetNoEF_EFxe25_noMu* (with the implicit requirement that $|\eta| < 3.2$ which is already included in *L2_j70*) to get comparable efficiency rates for the *SU4* MC sample, see equation (7.5). To get an idea of the data rate in which the evaluated trigger configurations would result, the number of events passing the above trigger is compared to the number of events passing *EF_j75_a4tc_EFFS_xe45_loose_noMu*. This ratio is multiplied with the data rate at EF Level corresponding to *EF_j75_a4tc_EFFS_xe45_loose_noMu* which is 15 Hz for the instantaneous luminosity of

$10^{33}\,\mathrm{cm}^{-2}\mathrm{s}^{-1}$. The data rate is calculated according to equation (7.6) [56].

$$\epsilon = \frac{N\,events\ passing\,L1\_J50\_L2\_j70\_|\eta|xx\_EF\_j75\_xeXX}{N\,events\ passing\,EF\_j75\_a4tc\_EFFS\_jetNoEF\_EFxe25\_noMu} \tag{7.5}$$

$$data\,rate = \frac{N\,events\ passing\,L1\_J50\_L2\_j70\_|\eta|xx\_EF\_j75\_xeXX}{N\,events\ passing\,EF\_j75\_a4tc\_EFFS\_xe45\_loose\_noMu} \cdot 15Hz \tag{7.6}$$

The plot in figure 7.9 shows the data rate indicated by colour on the z-axis for the cut on $|\eta|$ of the leading L2 jet (x-axis) and the E_T^{miss} at EF Level (y-axis). The corresponding numbers are listed in table 7.1. Figure 7.10 shows the efficiency for the *SU4* signal in the same style and the efficiencies are also given in table 7.2.

This study pursues the goal of decreasing the data rate by at least a factor of three and sustaining a signal efficiency which is not lower than the one for the baseline trigger configuration; a trigger signature which means that the efficiency becomes substantially smaller than 90 % will therefore not be taken into consideration.
Loosening the requirement on *EF_xe* with respect to *xe45* makes the data-rates with 20 - 60 Hz significantly higher than the initial 15 Hz. Only for *EF_xe* > 40 GeV with additional requirements on $|\eta|$ the data rate becomes < 15 Hz. A significant decrease of the data rate to < 5 Hz can only be obtained when asking for *EF_xe* > 50 GeV. A trigger signature involving *EF_xe* > 50 GeV means for the supersymmetric *SU4* signal a decrease of the efficiency to a maximum of 87 %. A high efficiency of > 90 % can only be maintained for a cut on *EF_xe* not higher than 40 GeV and still a large distribution of the pseudorapidity of the L2 jets of $|\eta| < 2.7$.

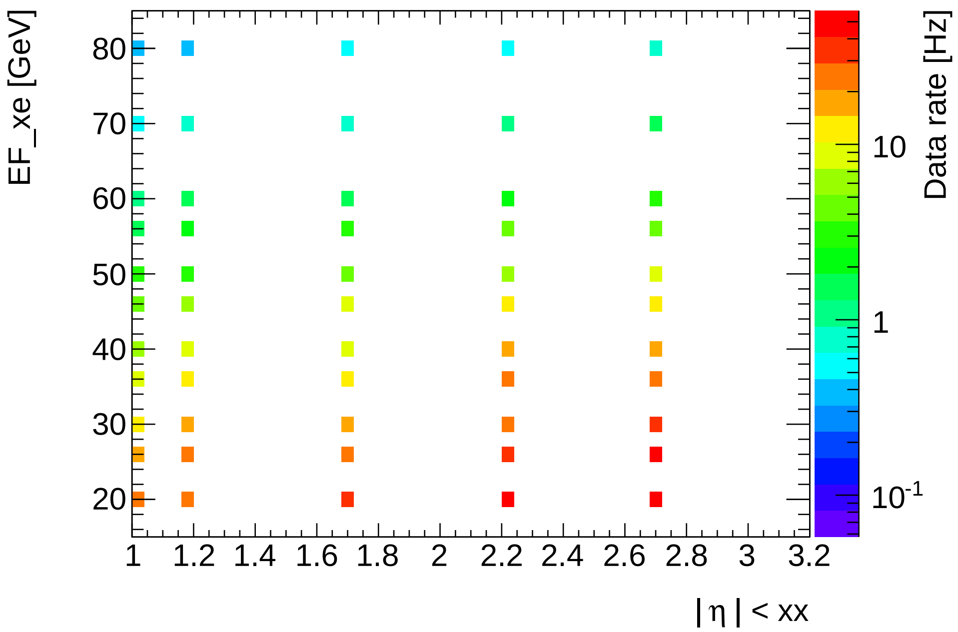

Figure 7.9.: Data rate for real data indicated by colour on the logarithmic z-axis for the trigger signature *L1_J50_L2_j70_*$|\eta|$*xx_EF_j75_xeXX*. Various demands on $|\eta|$ of the L2 jet (x-axis) and E_T^{miss} at EF Level (y-axis) are listed. The instantaneous luminosities are $\mathcal{L} = 2.44 \cdot 10^{33}\,\mathrm{cm}^{-2}\mathrm{s}^{-1}$ (period B) and $6.57 \cdot 10^{33}\,\mathrm{cm}^{-2}\mathrm{s}^{-1}$ (period D).

	Data rate [Hz]				
Trigger	$\|\eta\| < 2.7$	$\|\eta\| < 2.2$	$\|\eta\| < 1.7$	$\|\eta\| < 1.2$	$\|\eta\| < 1.0$
EF_xe80	0.71	0.64	0.5	0.4	0.34
EF_xe70	1.3	1.2	0.88	0.69	0.58
EF_xe60	3.0	2.5	1.8	1.4	1.2
EF_xe55	4.7	3.9	2.7	2.1	1.8
EF_xe50	8	6.5	4.4	3.4	2.8
EF_xe45	14	11	7.5	5.8	4.8
EF_xe40	19	15	10	7.8	6.5
EF_xe35	26	21	14	11	9.1
EF_xe30	35	28	19	15	13
EF_xe25	46	38	27	21	18
EF_xe20	58	48	35	27	23

Table 7.1.: Data rates for real data for the trigger signature *L1_J50_L2_j70_*$|\eta|$*xx_EF_j75_xeXX*. Various demands on $|\eta|$ of the L2 jet and E_T^{miss} at EF Level are listed.

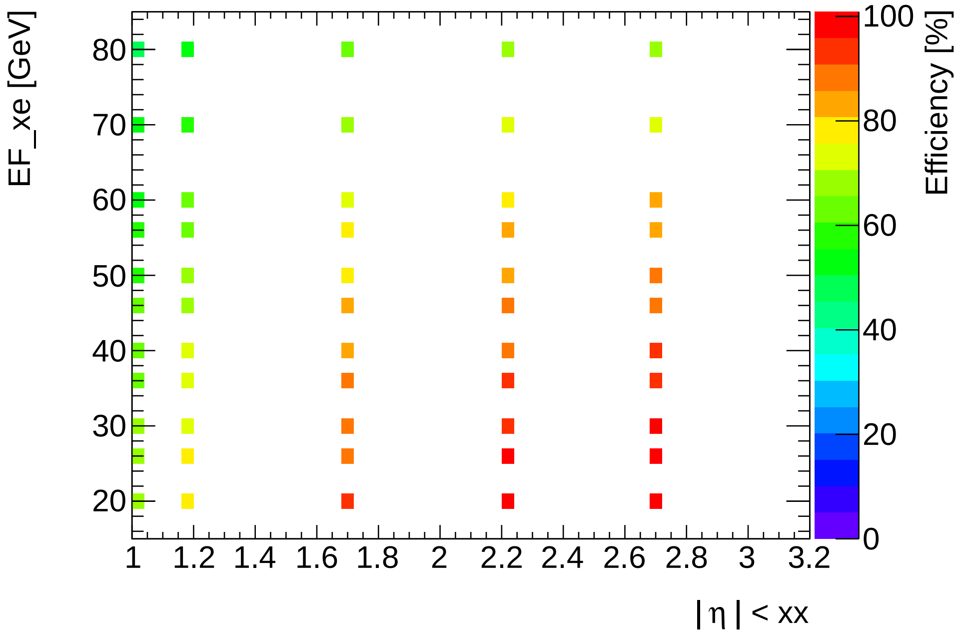

Figure 7.10.: Efficiency for *SU4* MC simulated data indicated by colour on the z-axis for the trigger signature *L1_J50_L2_j70_*$|\eta|$*xx_EF_j75_xeXX*. Various demands on $|\eta|$ of the L2 jet (x-axis) and E_T^{miss} at EF Level (y-axis) are listed.

	Efficiency [%]				
Trigger	$\|\eta\| < 2.7$	$\|\eta\| < 2.2$	$\|\eta\| < 1.7$	$\|\eta\| < 1.2$	$\|\eta\| < 1.0$
EF_xe80	69	67	62	53	47
EF_xe70	75	73	68	58	51
EF_xe60	81	79	73	63	55
EF_xe55	84	82	76	65	57
EF_xe50	87	85	79	68	59
EF_xe45	90	88	81	70	62
EF_xe40	92	90	84	72	63
EF_xe35	95	93	86	74	65
EF_xe30	97	95	88	76	67
EF_xe25	99	97	90	77	68
EF_xe20	101	98	91	78	69

Table 7.2.: Efficiency for MC simulated *SU4* signal for the trigger signature *L1_J50_-L2_j70_*$|\eta|$*xx_EF_j75_xeXX*. Various demands on $|\eta|$ of the L2 jet and E_T^{miss} at EF Level are listed.

In addition to demanding one jet at L2 pointing to a special $|\eta|$ region the requirements can be made even more stringent by asking for two central jets in the event. Plots show the resulting data rates and efficiencies in figure 7.11.

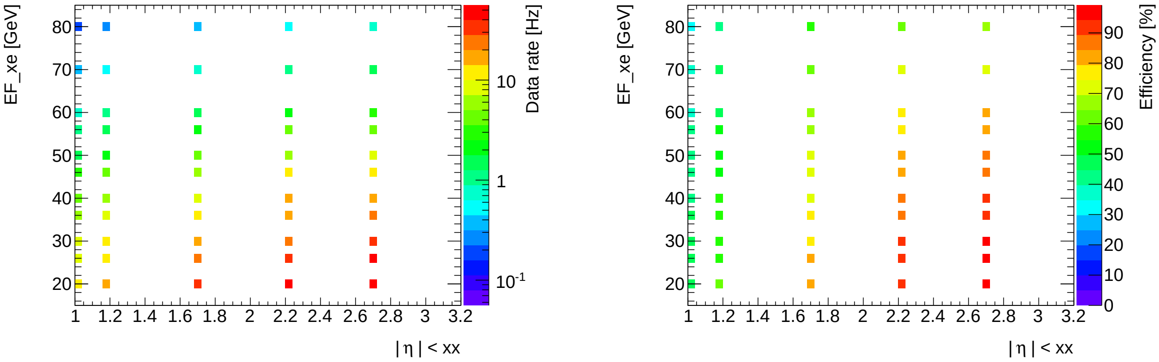

Figure 7.11.: Data rate for real data (left) and efficiency for *SU4* MC simulated data (right) indicated by colour on the (logarithmic) z-axis for the trigger signature *L1_J50_L2_j70_*$|\eta|$*xx_EF_j75_xeXX*. Various demands on $|\eta|$ of **two** L2 jets (x-axis) and E_T^{miss} at EF Level (y-axis) are listed.

See tables A.1 and A.2 in the appendix for data rate and efficiency numbers. Now the data rate becomes smaller than 15 Hz already for *EF_xe* > 25 GeV if stringent demands on $|\eta|$ like $|\eta| < 1.2$ (14 Hz) or $|\eta| < 1.0$ (9.9 Hz) are applied. At the baseline configuration with *EF_xe* > 45 GeV the data rate is further decreased to a minimum of 2.9 Hz when asking for two jets pointing to $|\eta| < 1.0$ This promising decrease of the data rate unfortunately results in a sharp decrease of the *SU4* signal efficiency to 43 % for *EF_xe* > 45 GeV and $|\eta| < 1.0$.

The data rate decreases less compared to the efficiency when requiring two central jets. The data rate is e.g. lessened from 15 Hz to 4.8 Hz (≈ 32 %) when requiring one central jet with $|\eta| < 1.0$ and *EF_xe* > 45 GeV and is only further decreased to still 2.9 Hz (≈ 60 % of 4.8 Hz) when requiring a second central jet. On the other hand is the efficiency diminished to 62 % for one central jet and further decreased to 43 % (which is 69 % from 62 %) for the requirement of two central jets. In figure 7.12 on the right-hand side the distribution of $|\eta|$ of the leading L2 jet (orange) is very similar to the one of $|\eta|$ of the second leading jet (purple) for simulated MC data. The efficiency is therefore lessened with the same factor when requiring two central jets compared to the requirement of one central jet. On the left-hand side of figure 7.12 the distribution of $|\eta|$ of the leading and second leading L2 jets is different; the second leading jets are more central. Therefore the data rate decreases less when requiring a second central jet.

Since the efficiency never exceeds 90% for this trigger configurations with two central jets when the data rate is lower than 15 Hz, it is not reasonable to consider those for decreasing the data rate.

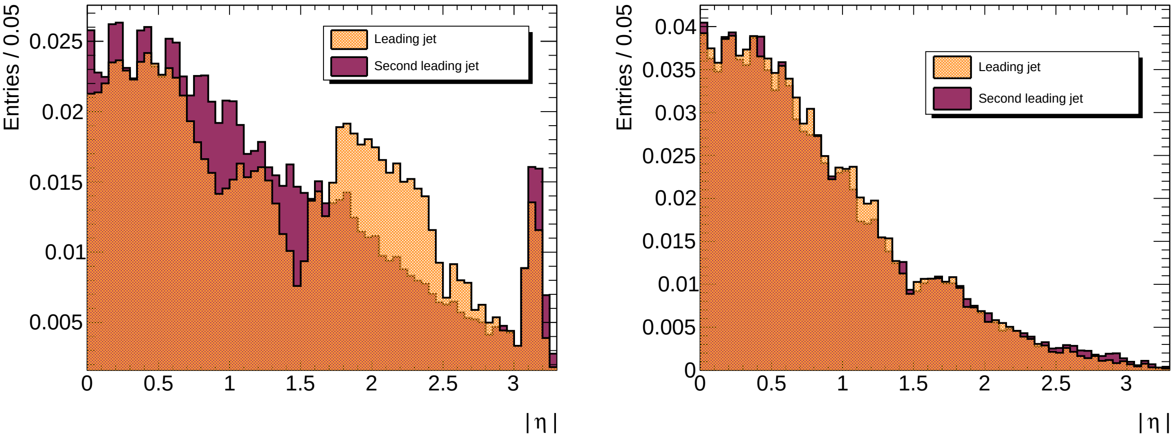

Figure 7.12.: Distribution of $|\eta|$ of the leading (orange) and second leading (purple) L2 jets for real data (left) and MC simulated SUSY signal (right). The distributions are normalized to 1.

7.2.3.3. Selection of the Trigger Jets

The leading L1 jet is chosen by just taking the L1 jet object with the highest p_T, namely the largest deposited energy in a window of 8×8 trigger towers. The correlation of η of the first and η of the second leading jet at L1 for MC simulated data is plotted in figure 7.13.

Showing this figure is motivated by the fact that at L2 of the trigger the allocation of the calorimeter clusters to the highest and second highest p_T jet is sometimes wrong. The jet collections on L2 seem to suffer from double counting of jet clusters which is probably caused by several trigger signatures being evaluated in parallel and their output dumped in the same trigger jet collection. η of the first and η of the second highest p_T jets are strongly correlated at L2 - a feature which is shown for MC data in figure 7.14 on the left-hand side. Obviously, the highest and the second highest p_T jets use the same calorimeter clusters with the same η coordinates.

The jets at L1 are therefore taken for orientation when looking for the leading and second leading jets at L2. To make sure there is no cluster used twice in the L2 jets, it is more reliable to choose those which have the smallest $\Delta R = \sqrt{\Delta\phi^2 + \Delta\eta^2}$ to the leading and second leading jets at L1.

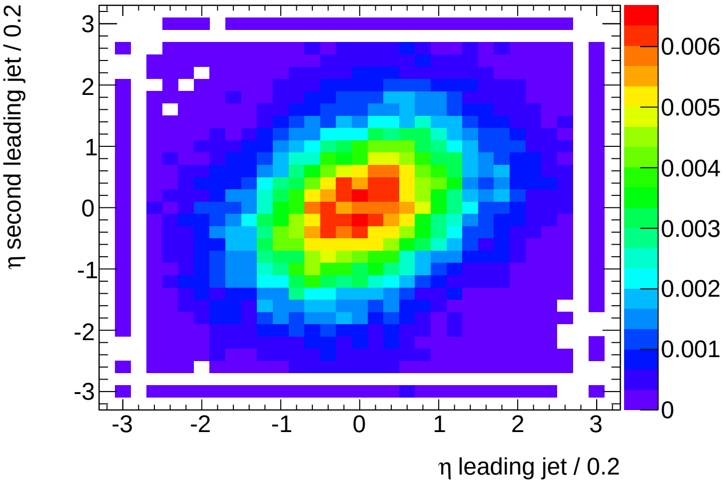

Figure 7.13.: MC simulated data: Distribution of η of the leading versus second leading jet at **L1** ordered by highest p_T. The distribution is normalized to 1.

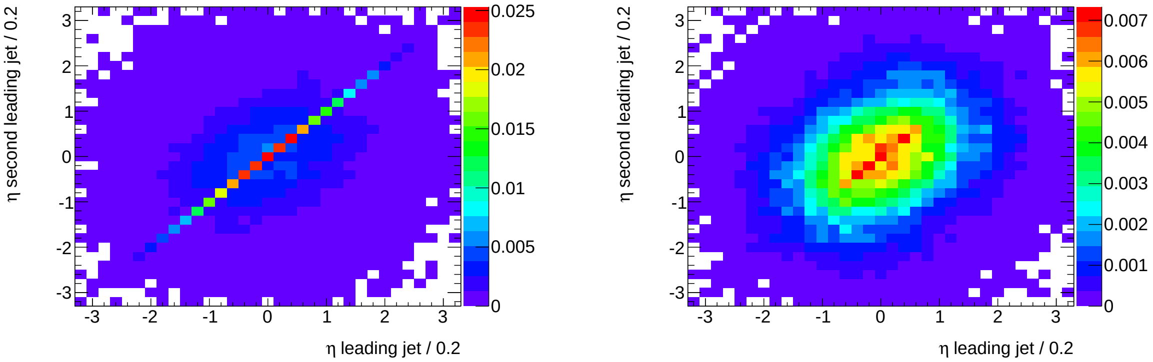

Figure 7.14.: MC simulated data: Distribution of η of the leading versus second leading jet at **L2** ordered by highest p_T (left) and chosen by smallest ΔR to L1 jets (right). Both distributions are normalized to 1.

The plot on the right-hand side of figure 7.14 shows the η of the first and second leading jet at L2 when the jets were determined by the smallest ΔR. The colour indicated correlation is less strong and thus the check on ΔR was used.

In figure 7.15 the correlation of η of the first and of the second highest p_T jets is shown for real data (left). The effect of the ΔR check is less strong (right-hand side).

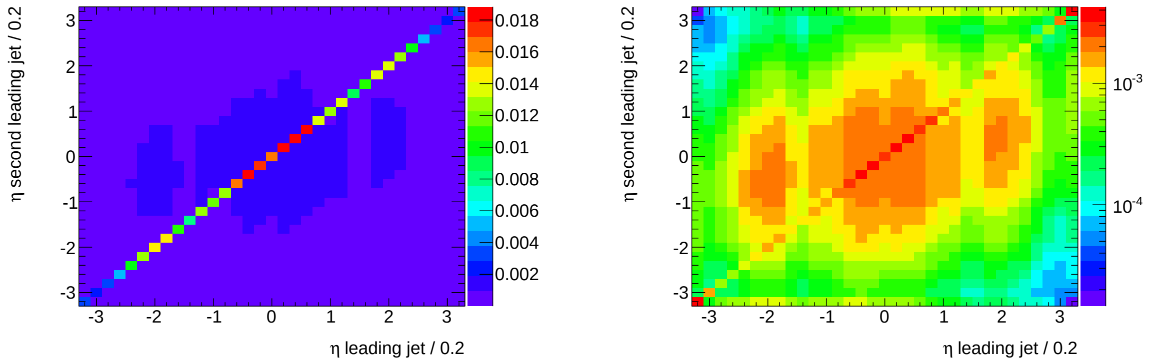

Figure 7.15.: Real data: Distribution of η of the leading versus second leading jet on **L2** ordered by highest p_T (left) and chosen by smallest ΔR to L1 jets with logarithmic colour indication (right). Both distributions are normalized to 1.

7.2.3.4. Variation of the Jet Trigger Requirements

Next to the 2011 baseline trigger for the *0-lepton channel* analysis two other trigger chains were evaluated. *EF_j55* is seeded by *L1_J30* and *L2_j50* while *EF_j100* demands *L1_J75* and *L2_j95* on the earlier trigger levels. The data rates and signal efficiencies have been studied for the requirement on the centrality of the jets on L2 of the trigger.

The trigger signatures for the looser jet requirement *L1_J30_L2_j50_*$|\eta|$*xx_EF_j55_xeXX* result as expected in slightly higher data rates than for the baseline trigger signature. For the data rates and efficiencies see table A.3 to A.6 and figures A.1 and A.2 in the appendix. Instead of 7.5 Hz for $|\eta| < 1.7$ after *L1_J50_L2_j70_*$|\eta|$*xx_EF_j75_xeXX* there are now 7.7 Hz. Looking at the signal efficiencies computed from the MC *SU4* data, these remain higher with 88 % instead of 81 % for the reference point. The less stringent requirement on the jet p_T corresponding to *EF_j55* results in a promising high efficiency of > 97 % and a data rate equal to 14 Hz for *EF_xe* > 45 GeV with $|\eta| < 2.7$. But here again the rate reduction to < 5 Hz with *EF_xe* > 50 GeV and $|\eta| < 1.7$ results in a efficiency smaller than 85 %. The rate reduction is attained analogously when asking for 2 jets in a special $|\eta|$ region.

The behaviour of the data rates and trigger efficiencies when asking for the tighter *L1_J75_L2_j95_*$|\eta|$*xx_EF_j100_xeXX* comes as no surprise. For the data rates and efficiencies see table A.7 to A.10 and figures A.3 and A.4 in the appendix. The data rate does not exceed the 15 Hz already for *EF_xe* > 30 GeV when asking for $|\eta| < 1.2$ in addition (12 Hz). Requiring two jets in a special $|\eta|$ region further drastically decreases the data rate to 5.7 Hz for $EF\_xe > 45$ GeV and $|\eta| < 1.7$. But the trigger efficiency for SUSY signal is lowered to 62 %, too.

7.3. Conclusion of Efficiency Studies

Implementing the idea of reducing Standard Model background when cutting on $|\eta|$ of leading jets shows that the data rate can indeed be decreased very much. But when checking what those tight trigger signatures yield for the SUSY signal efficiencies, it must be confessed that too much signal would be lost. For the baseline trigger signature, the efficiency falls to $\epsilon < 80\,\%$ when the data rate is lowered to < 5 Hz and becomes even lower than 70 % when asking for two central jets. Varying the jet requirement in the trigger signature to *EF_j55* respectively *EF_j75* allows the same conclusion - increasing the requirement on the jet p_T to *EF_j100* constrains the efficiency to values which are lower than 80 % already for $EF\_xe > 45$ GeV (see table A.8) while ϵ is still at $> 90\,\%$ for *EF_j75*.
Alternatively only considering trigger signatures which sustain a high signal selection efficiency $> 90\,\%$ translates in data rates marginally lower than 15 Hz. Therefore it seems not worthwhile to integrate the demand on the pseudorapidity of the jets in the trigger algorithm as this implicates some technical effort.
It is more advisable to just raise the cut on E_T^{miss} in the trigger. From table 7.1 it becomes apparent that the data rate decreases from 15 Hz to ~ 5 Hz when the requirement on E_T^{miss} is raised to 55 GeV. At the same time the efficiency stays at $\sim 85\%$.

8. E_T^{miss} Turn-on Curves

8.1. Turn-on Curves for the 2011 Baseline Trigger

Already mentioned in chapter 7.2.3 is the 2011 trigger baseline for the analysis of supersymmetric events which is *EF_j75_a4tc_EFFS_xe45_loose_noMu* for triggering on jets and E_T^{miss}. The turn-on curve for $E_T^{miss} = MET\_Simplified20\_RefFinal\_et$ was already shown in that previous chapter in figure 7.4 for the *JetTauEtmiss stream*. In principal the turn-on curve should have the same behaviour also for the *Muon stream* and the *Egamma stream*[1].

For the *Muon stream* the turn-on is expected to be faster since the trigger uses E_T^{miss} at EF Level which does not include muons in its computation but *MET_Simplified20_RefFinal_et* on the x-axis does. For a direct comparison the *MET_Simplified20_RefFinal_et* is calculated without muons in the *Muon stream*. This is no issue in the other streams because there an event does not need to have at least one muon in the final state.

In figure 8.1 the turn-on curves for all three streams are shown. The following study and all evaluations are made with real data of run period B and D of 2011 ATLAS data, corresponding to an integrated luminosity of 165 pb^{-1}. The object selection recommendation for the *0-lepton channel* is applied but not the lepton veto as this would result in too low statistics. The leading jet must have p_T>130 GeV.

The turn-on for the *Muon stream* (green) is lying almost exactly on top of the one for the *JetTauEtmiss stream* (orange). Both reach the plateau at 100 % for $E_T^{miss} \approx 130$ GeV, although the curve in the *Muon stream* is still a little bit faster for $60\,\text{GeV} < E_T^{miss} < 130\,\text{GeV}$. However, since the offline cut is adjusted to be in the plateau region with $E_T^{miss} > 130$ GeV, this small difference should not affect the analysis in any way. Curiously enough the efficiency in the *Egamma stream* (purple) rises notably much slower. It reaches the plateau only for $E_T^{miss} \approx 180$ GeV and does not reach 100 %. The p_1 and p_2 values also

---

[1] The corresponding trigger signature is *EF_e20_medium* for the *Egamma stream*: the electron which is identified with medium quality must have p_T>20 GeV at EF level. *EF_mu18* is the trigger signature for the *Muon stream*.

differ very much compared to the ones of the other two curves: The *Egamma stream* curve only reaches $\epsilon = 50\,\%$ for $E_T^{miss} = 100\,\text{GeV}$, the other curves reach it much faster at $\sim 60\,\text{GeV}$.

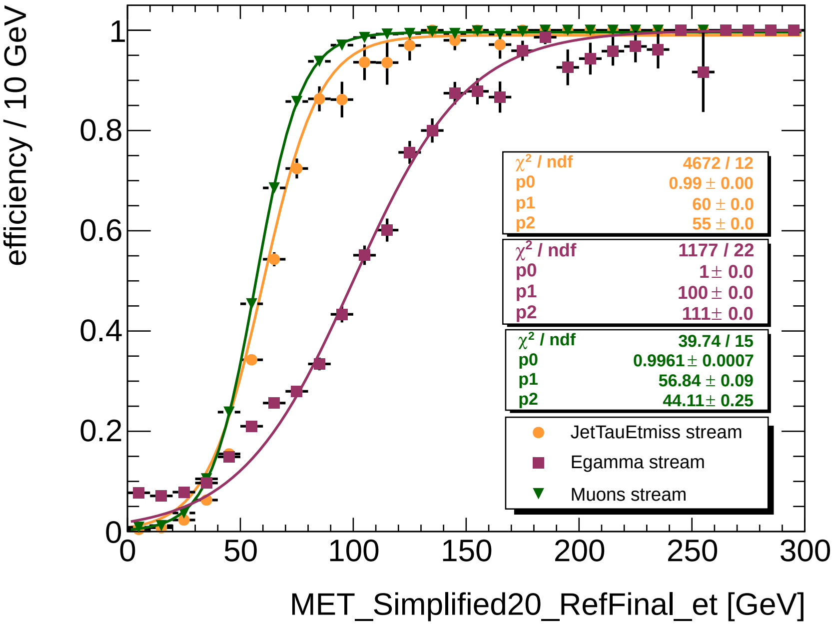

Figure 8.1.: Turn-on curves for *EF_j75_a4tc_EFFS_xe45_loose_noMu* with *MET_-Simplified20_RefFinal_et* on the x-axis in the *JetTauEtmiss* (orange), *Muon* (green) and *Egamma* (purple) *stream*.

The comparison of the three trigger streams where the muons are included in the computation of the E_T^{miss} in the *Muons stream* is shown in figure C.1 in the appendix where the *Muon stream* turn-on curve is thus even faster.

There is no obvious reason for such a difference between the behaviours in the *JetTauEtmiss stream* and the *Egamma stream* since *MET_Simplified20_RefFinal_et* is calculated including both the electron and jet objects of an event. As the plateau is reached far beyond the offline cut, this behaviour could impact analyses for events containing electrons (e.g. in control regions or lepton-based analysis relying on the E_T^{miss} trigger) and should hence be studied in more details.

To check whether the difference in the turn-on curves of the streams is also visible when another method of computing E_T^{miss} is used, the turn-on is also drawn for *MET_-RefFinal_et*. Its algorithm is described below.

- Firstly the missing transverse energy is calculated from the calibrated calorimeter cell energies and the stand-alone muons to avoid double-counting of the muons.
- The cryostat term is added to include the energy loss between the barrel calorimeters and the tile calorimeters [25].
- The redefinition of the missing transverse energy is done by associating each calorimeter cell to the reconstructed electrons, photons, hadronically decaying τ-leptons, jets and muons in the given order. The initial global calibration is also replaced by the one of the individual objects. Remaining unassigned cells are globally calibrated and contribute to the E_T^{miss}, too [57].

To search for supersymmetric events, the *MET_Simplified20_RefFinal_et* is used because in the offline analysis the jet calibration is done with the JES (see chapter 4.1.2). The jet calibration used in the *MET_RefFinal_et* computation is a more elaborate one. It is desirable to use the same calibration for both the E_T^{miss} and the offline jets in order to compute coherent M_{eff} values[2] and to propagate the systematics in transparent way. On theses grounds *MET_RefFinal_et* is not used a priori whereas it is closer to the 'true' E_T^{miss}.

Since it is the turn-on curve in the *Egamma stream* which shows an unexplained behaviour for *MET_Simplified20_RefFinal_et*, it is compared to the curve for *MET_RefFinal_et* also in the *Egamma stream* in figure 8.2.

The contribution of the muons in *MET_RefFinal_et* is replaced by the contribution of the selected muons in the *0-lepton channel* analysis because for *MET_RefFinal_et* low-quality muons are used. The consequences of these different quality criteria still have to be investigated.

Interestingly enough, the difference between the turn-on curves remains. The *MET_RefFinal_et* curve reaches the plateau for $\sim 130\,\text{GeV}$ even though the efficiency is not at $100\,\%$ yet. The rise with E_T^{miss} is faster, too, with a p_1 fitting parameter equal to $70\,\text{GeV}$ and $p_2 = 85\,\text{GeV}$. Implying that the *MET_RefFinal_et* algorithm works fine, there seems to be a problem in the calculation of *MET_Simplified20_RefFinal_et*. The turn-on curves for *MET_RefFinal_et* as a matter of fact all show the expected behaviour in the different trigger streams, see figure C.2 in the appendix.

---

[2] M_{eff} is the sum of E_T^{miss} plus the scalar sum over the p_T of N leading jets in an N-jet channel and the scalar sum of the p_T of the selected leptons ('H_T')

In the following, several checks will be made to get an idea of the difference between the two E_T^{miss} variables and to find out what causes the too slow turn-on of *MET_Simplified20_RefFinal_et* in the *Egamma stream*.

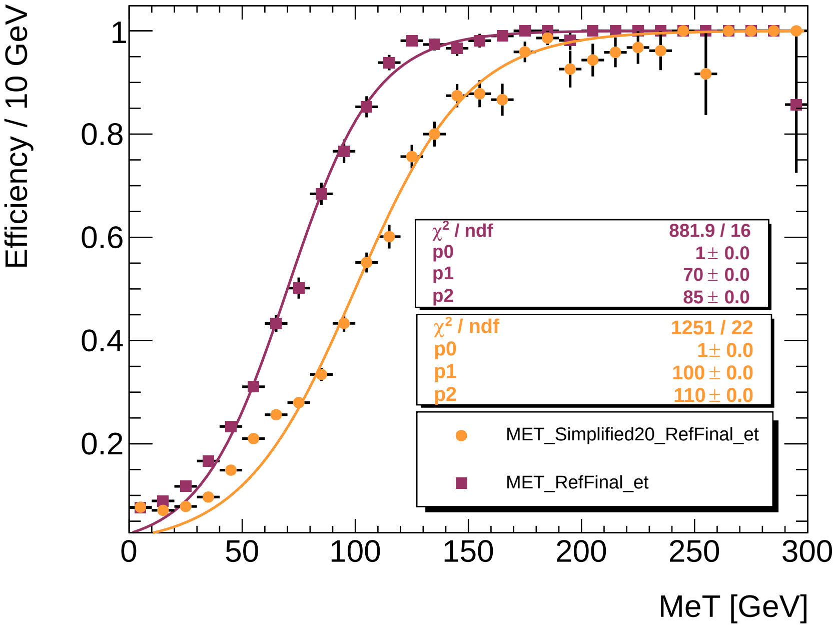

Figure 8.2.: Turn-on curves for *EF_j75_a4tc_EFFS_xe45_loose_noMu* with *MET_-Simplified20_RefFinal_et* (orange) and *MET_RefFinal_et* (purple) on the x- axis in the *Egamma stream*.

8.2. Comparison between E_T^{miss} Algorithms

The turn-on curves show that there is a correlation between offline E_T^{miss} and the variable the trigger uses, which is the E_T^{miss} at EF Level. To check whether the correlation of *MET_Simplified20_RefFinal_et* and E_T^{miss} at EF Level is indeed less strong compared to the one of *MET_RefFinal_et* and E_T^{miss} at EF Level, these are plotted in figure 8.3. On the left-hand side the colour-indicated correlation between *MET_RefFinal_et* and *EF_xe* is clearly visible. Compared to that, the plot on the right-hand side demonstrates that *MET_Simplified20_RefFinal_et* and *EF_xe* can differ by higher values. In figure 8.4 the two variables *MET_Simplified20_RefFinal_et* and *MET_RefFinal_et* are compared directly to each other. The correlation is widely spread, sometimes the variables in fact differ by $\mathcal{O}(100\,\mathrm{GeV})$. Hence, the assumption of significant variation in the E_T^{miss} algorithms is confirmed. The region with large values of *MET_Simplified20_RefFinal_et* while *MET_RefFinal_et* is very low leads to the problematic turn-on. This also means that these events, which probably have low ‘true‘ E_T^{miss}, can potentially populate the signal region.

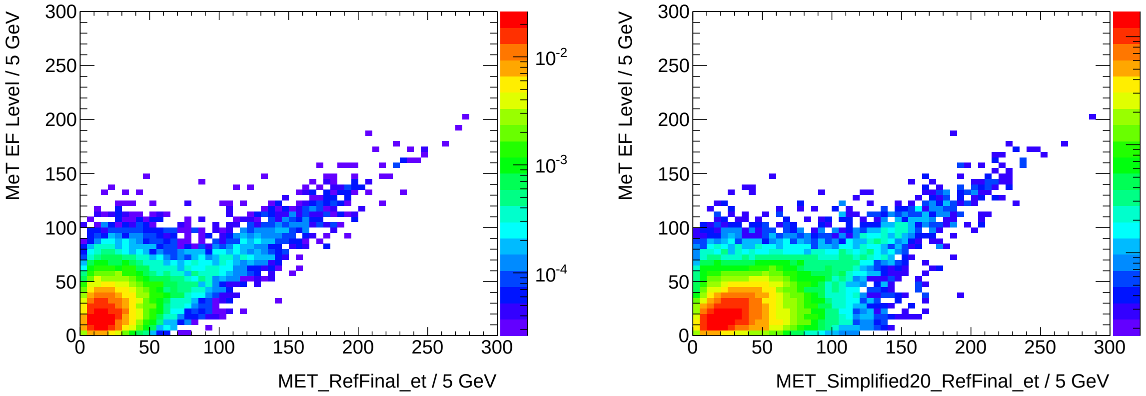

Figure 8.3.: Left: *MET_RefFinal_et* versus E_T^{miss} at EF Level; Right: *MET_Simplified20_RefFinal_et* versus E_T^{miss} at EF Level. The correlation is indicated by colour (logarithmic scale). Both distributions are normalized to 1.

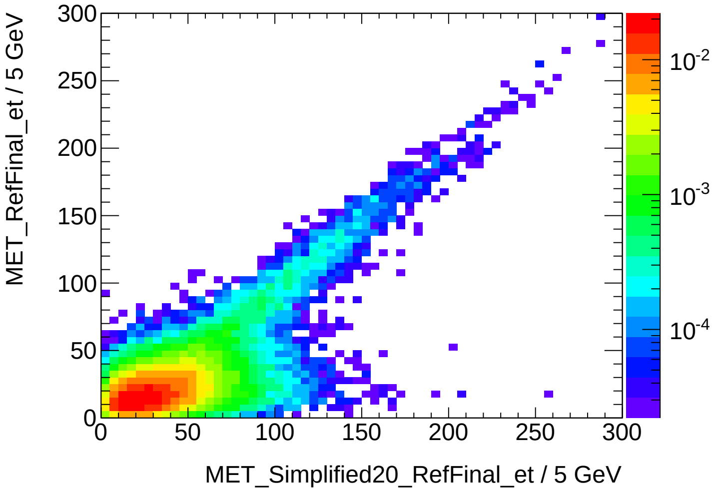

Figure 8.4.: *MET_Simplified20_RefFinal_et* versus *MET_RefFinal_et*. The correlation is indicated by colour (logarithmic scale). The distribution is normalized to 1.

8.2.1. Contribution of the Objects to E_T^{miss}

8.2.1.1. Contribution of the Photons

One thing which catches attention is the fact that *MET_RefFinal_et* also uses the contribution of photons as opposed to *MET_Simplified20_RefFinal_et*. It is possible to add the photons in the calculation - there is even a variable in the DPD where their contribution is already included. The resulting turn-on curve for *MET_Simplified20_-RefFinal_et* (orange) considering photons is shown in figure 8.5. It is again compared to the *MET_RefFinal_et* (purple) curve since it has the expected behaviour in the *Egamma stream*.

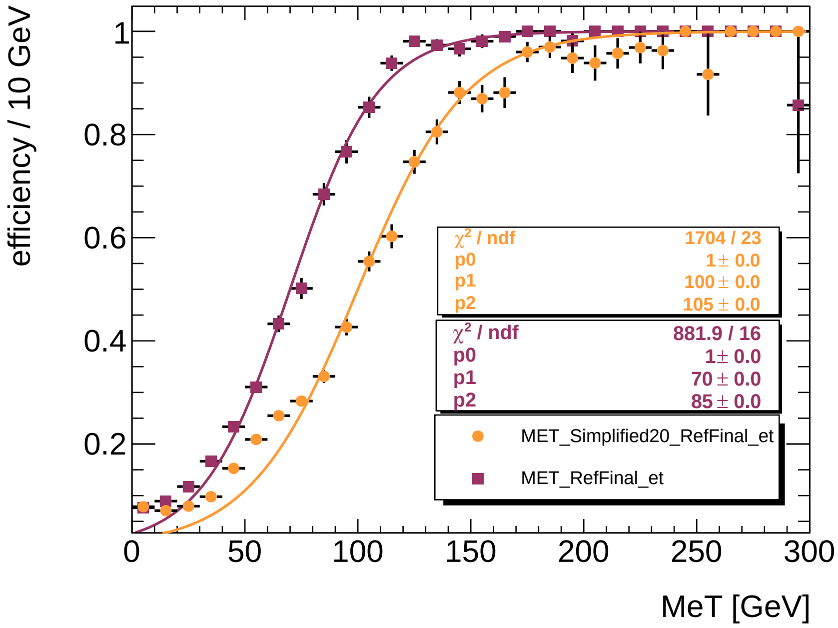

Figure 8.5.: Turn-on curves for *EF_j75_a4tc_EFFS_xe45_loose_noMu* with *MET_-Simplified20_RefFinal_et* plus photon contribution (orange) and *MET_RefFinal_et* (purple) on the x-axis in the *Egamma stream*.

The curve for *MET_Simplified20_RefFinal_et* with photons looks almost exactly the same as the one in figure 8.2 and also only the fitting parameter p_2 needs a small change to 105 GeV. Only some points around $E_T^{miss} \approx 200$ GeV are slightly shifted to higher ϵ. Omitting the contribution of the photons seems not to be the issue.

8.2.1.2. Difference between the Contributions

Both E_T^{miss} computations are based on summing over the p_T of all objects in an event. Therefore it is natural to compare the contributions of each category of objects with a view to significant differences in order to explain the different behaviour of the turn-on curves. The contribution of all jets, electrons, muons or the ‘CellOut‘ in an event are accessible in the DPDs. The difference between the contributions of the selected electrons to *MET_RefFinal_et* and to *MET_Simplified20_RefFinal_et* is shown in figure 8.6 on the left-hand side. The variables are called *MET_RefEle_et* and *MET_Simplified20_-RefEle_et*. The contribution in principal just corresponds to

$$E_{T\ electrons}^{miss} = \sqrt{(\sum_{sel.\,electrons} p_x)^2 + (\sum_{sel.\,electrons} p_y)^2}. \tag{8.1}$$

For electrons, there seems to be no difference. The check on the ‘CellOut‘ terms shows a small difference of $\mathcal{O}(\pm 20\text{ GeV})$, see figure 8.6 on the right-hand side, but this is too small to explain the $\mathcal{O}(100\,\text{GeV})$ seen in some cases.

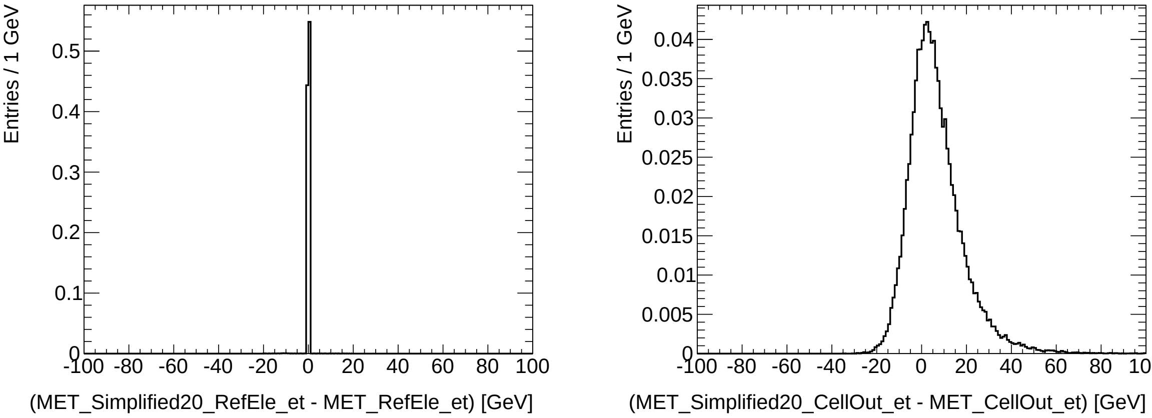

Figure 8.6.: Left: Difference between *MET_Simplified20_RefEle_et* and *MET_-RefEle_et*. Right: Difference between *MET_Simplified20_CellOut_et* and *MET_CellOut_et*. The distributions are normalized to 1.

On the other hand there is a substantial difference in the contributions of the jets to the E_T^{miss}, expressed by (*MET_Simplified20_RefJet_et* - *MET_RefJet_et*), up to ± 60 GeV and sometimes even ± 100 GeV. The distribution can be seen in figure 8.7. It is known that the two algorithms use different jets and jet calibrations. However, the different jets and jet calibrations can not be the cause of the problem, as was already shown in figure 8.1: The turn-on curve for the *JetTauEtmiss stream* does not show a strange behaviour even if at least one high-p_T jet in every event is required. Still, the different jet contributions remain as a key to the cause of the problem.

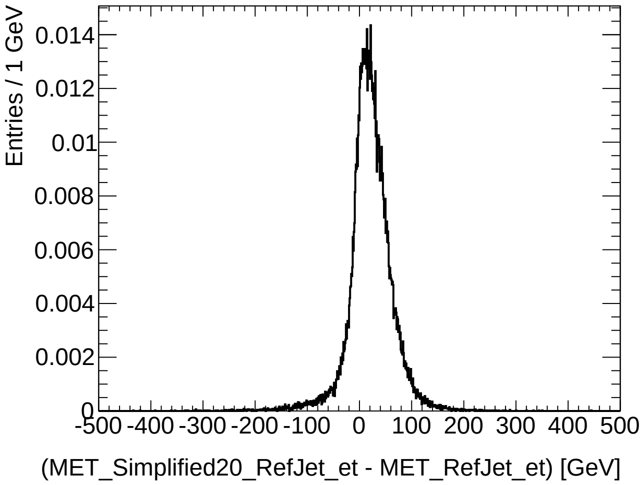

Figure 8.7.: Difference between *MET_Simplified20_RefJet_et* and *MET_RefJet_et*. The distribution is normalized to 1.

8.2.1.3. Contribution of the Electrons

Seeing that the turn-on curve for *MET_Simplified20_RefFinal_et* only shows a weird behaviour in the *Egamma stream*, the problem seems to have something to do with the presence of an electron. The distribution of the contribution of the electrons to *MET_Simplified20_RefFinal_et* is shown in figure 8.8.

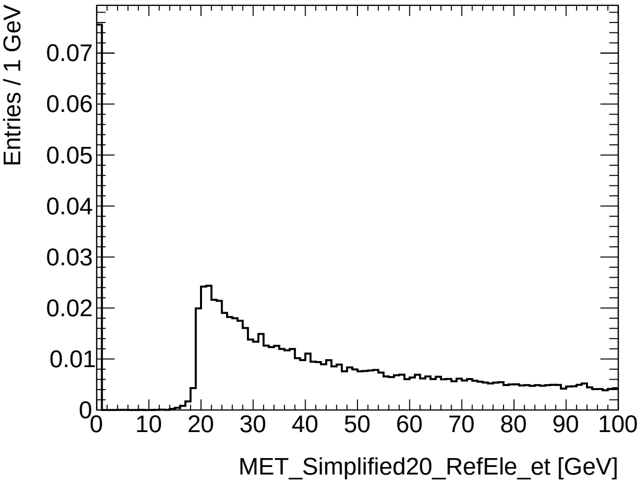

Figure 8.8.: *MET_Simplified20_RefEle_et* is shown on the x-axis. The distribution is normalized to 1.

The variable *MET_Simplified20_RefEle_et* clearly peaks at 0 GeV: almost 10 % of all events do not contain any selected electrons at all; the triggering electron seems to be rejected during the object selection. As a matter of fact, 99.5 % of all the electrons in the events which have sufficient p_T and $|\eta| < 2.47$ are rejected because they are not reconstructed with medium quality, of the remaining electrons 17 % are rejected because they are not reconstructed by the standard cluster-based algorithm and all the rest touches a dead optical transmitter or could not be reconstructed reliably. This is not surprising, as the electron trigger algorithm is looser than the offline electron reconstruction algorithm.

The efficiency of *MET_Simplified20_RefFinal_et* is at $\sim 8\,\%$ for $E_T^{miss} < 20\,\mathrm{GeV}$ in the *Egamma stream* while the curves for the other two streams still have $\epsilon = 0\,\%$. This is clearly visible in figure 8.1. Requiring that the leading electron in an event must be identified with medium quality adjusts the efficiency in the region with $E_T^{miss} < 20\,\mathrm{GeV}$, see figure C.3 in the appendix.

Whether the rejection of the electrons has something to do with the weird behaviour of the turn-on curve will be checked hereafter. Only events containing electrons which contribute at least 1 GeV to *MET_Simplified20_RefFinal_et* are selected. The turn-on curve for *MET_Simplified20_RefFinal_et* (orange) is again compared to the one for *MET_RefFinal_et* (purple) in the *Egamma stream* in figure 8.9.

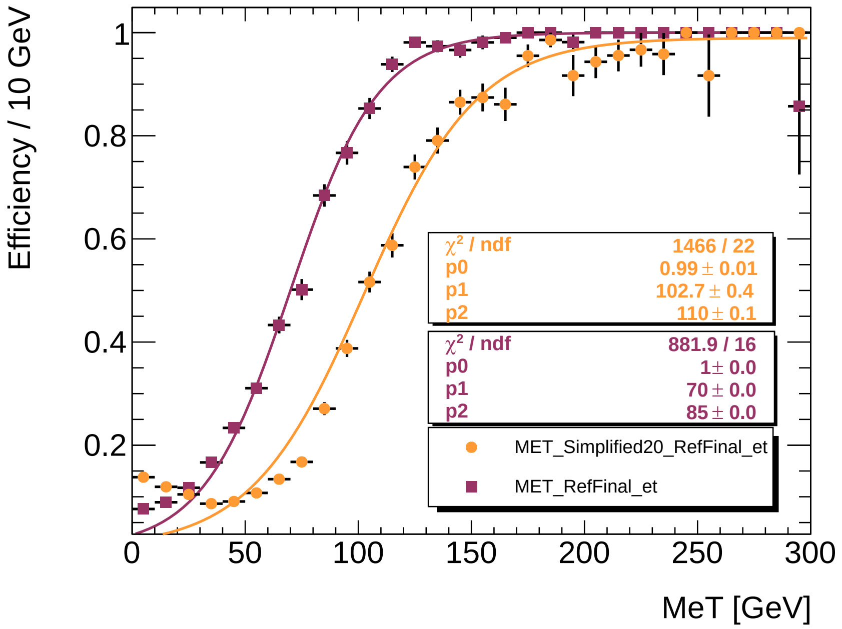

Figure 8.9.: Turn-on curves for *EF_j75_a4tc_EFFS_xe45_loose_noMu* with *MET_Simplified20_RefFinal_et* (orange) and *MET_RefFinal_et* (purple) on the x-axis in the *Egamma stream*. Only events with *MET_Simplified20_RefEle_et* ≥ 1 GeV are used for the *MET_Simplified20_RefFinal_et* turn-on curve.

From the fit parameters only a slight change of the shape of the curve can be reported - instead of at 100 GeV the curve reaches $\epsilon \approx 50\,\%$ now at 103 GeV but the turn-on is as slow as before, with $p_2 = 110$ GeV.

The turn-on curve where on the other hand only events with *MET_Simplified20_RefEle_et* < 1 GeV are used, i.e. events not containing any electrons in the final state after the object selection, is shown in figure 8.10. Again the orange curve shows the efficiency for *MET_Simplified20_RefFinal_et* for the trigger signature *EF_j75_a4tc_EFFS_xe45_loose_noMu* where this time no electrons contribute. The shape of the curve changes very much, reaching the plateau at $\epsilon = 100\,\%$ for ≈ 130 GeV. This is also expressed in the fitting parameters - the turn-on is even faster than for *MET_RefFinal_et*.

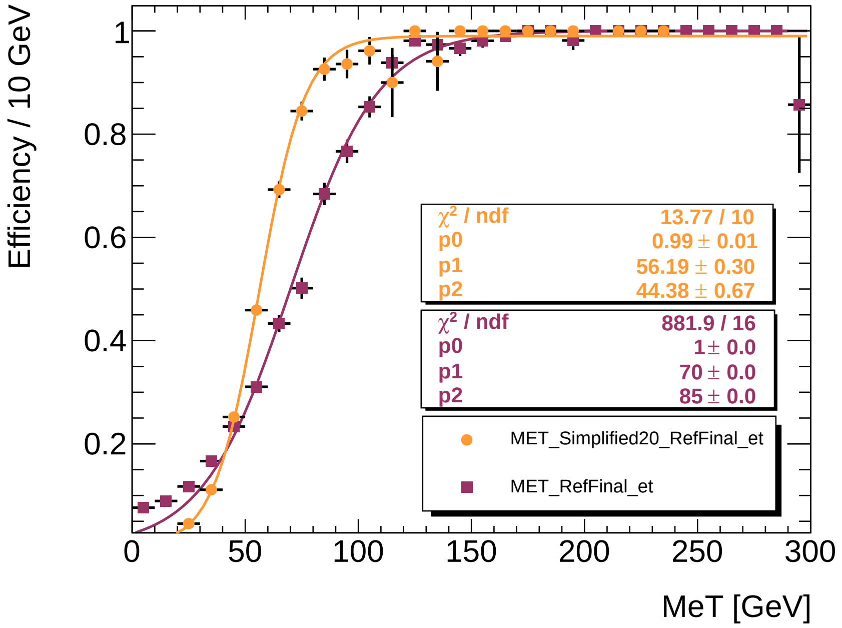

Figure 8.10.: Turn-on curves for *EF_j75_a4tc_EFFS_xe45_loose_noMu* with *MET_-Simplified20_RefFinal_et* (orange) and *MET_RefFinal_et* (purple) on the x- axis in the *Egamma* stream. Only events with *MET_Simplified20_RefEle_et* <1GeV are used for the *MET_Simplified20_RefFinal_et* turn-on curve.

The turn-on curve hence shows a good shape when no electrons are left in the event after the preselection which could contribute to *MET_Simplified20_RefFinal_et*. The assumption that the weird behaviour of the turn-on curve in the *Egamma stream* is due to the required electron seems to prove itself. Only for events containing electrons the turn-on curve is much too slow.

The reconstruction of both the jet and electron objects uses information from the calorimeters. To make sure that the calorimeter cells with energy deposition are allocated only to one object, an overlap removal between electrons and jets is performed (see chapter 7.1). Due to the possibility of wrong assignments in this procedure, the correlation of *MET_Simplified20_RefEle_et* and *MET_Simplified20_RefJet_et* is checked in figure 8.11.

Surprisingly, the plot in figure 8.11 suggests some correlation between the two variables. This means that the contribution of the jets as well as the one of the electrons to *MET_Simplified20_RefFinal_et* is very similar in many cases. The reason for this could be an incorrect overlap removal - if a high p_T object is counted both as an electron and as a jet, it dominates also both the contribution of the electrons and of the jets to *MET_Simplified20_RefFinal_et*. This suspicion will be investigated in the next chapter.

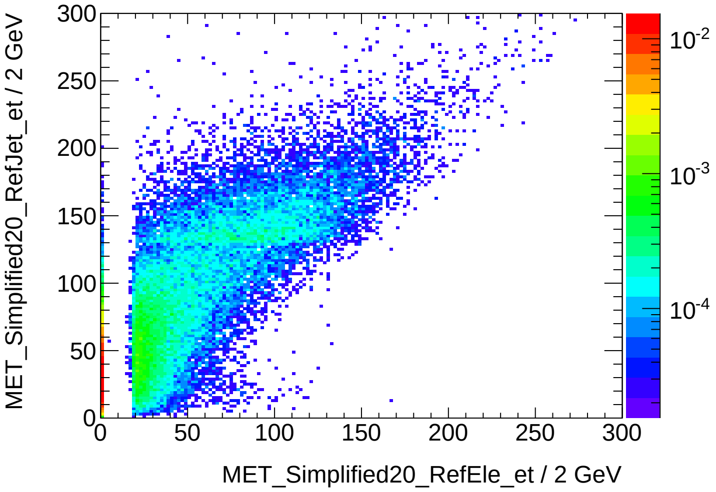

Figure 8.11.: *MET_Simplified20_RefEle_et* versus *MET_Simplified20_RefJet_et*. The correlation is indicated by colour (logarithmic scale). The distribution is normalized to 1.

8.3. Overlap Removal between Jets and Electrons

8.3.1. Example Event

The suspicion of incorrect overlap removal between jets and electrons is confirmed when looking for example at an event which is randomly chosen in a Monte Carlo simulated data sample. The sample used simulates the process $Z^0 \rightarrow e^+e^-$ and requires that three partons result from the interaction point. The electrons and jets contained in event number 20209 of the *mc10b p601* sample which is generated by *ALPGEN*[58] and *JIMMY*[59] are listed in table 8.1. When comparing the coordinates of the electron with index 0 and of the jet with index 0, they have almost the same η and ϕ, meaning that both objects point in the same direction and therefore must contain the same calorimeter cells. The overlap removal was not performed although ΔR equals only 0.01.

The information whether an object was used for the *MET_Simplified20_RefFinal_et* computation can be extracted from the DPD and if so, with which weight their x- and y-momentum components enter the E_T^{miss} computation. Both the leading jet and the

Index	p_x [GeV]	p_y [GeV]	η	ϕ [rad]	used for E_T^{miss}	weight$_x$	weight$_y$
Electrons							
0	-55.87	67.19	1.56	2.26	yes	1.02	1.02
1	-14.00	-24.03	0.79	-2.10	no	0	0
2	1.03	-4.07	1.75	-1.32	no	0	0
3	16.66	-10.43	3.75	-0.56	no	0	0
Jets							
0	-89.29	106.80	1.57	2.27	yes	0.94	0.95
1	-23.42	-40.31	0.85	-2.10	yes	1.03	1.03
2	39.06	-22.95	0.60	-0.53	yes	1.02	1.02
3	22.61	-14.28	3.76	-0.56	yes	1.01	1.00
4	7.85	-20.66	1.75	-1.21	yes	1.02	1.02
5	14.52	-1.52	1.69	-0.10	no	0	0
6	-2.09	14.11	-1.29	1.72	no	0	0
7	-8.16	-7.42	1.68	-2.40	no	0	0
8	-9.65	-3.39	-2.33	-2.80	no	0	0
9	9.66	-1.69	-2.20	-0.17	no	0	0
10	-9.36	0.37	1.97	3.10	no	0	0
11	-8.74	-2.28	1.47	-2.89	no	0	0
12	-4.83	5.57	-1.54	2.28	no	0	0
13	-3.59	-6.17	-1.07	-2.10	no	0	0

Table 8.1.: Attributes of electrons and jets in event 20209 of MC sample ZeeNp3.

leading electron which point in the same direction have been used for computing *MET_Simplified20_RefFinal_et*. *MET_Simplified20_RefFinal_et* equals 108.46 GeV in this event while *MET_RefFinal_et* equals only 28.45 GeV. The true E_T^{miss} is equal to 0 because in this simulated data there are no non-detectable objects assumed in the final state. *MET_RefFinal_et* is much closer to the true E_T^{miss} and therefore again seems more reliable.
From the DPD it is deduced that the jets contribute 37.75 GeV to *MET_Simplified20_RefFinal_et* but 92.19 GeV to *MET_RefFinal_et*.

In a ‘manual‘ overlap removal, the overlapping jet with index 0 is removed from *MET_Simplified20_RefFinal_et*, resulting in 110.51 GeV for *MET_Simplified20_RefJet_et* - that is much closer to the 92.19 GeV of the *MET_RefFinal_et* jet component. The initial

difference between the jet contributions of $\sim 55\,\text{GeV}$ shrinks to $\sim 18\,\text{GeV}$. An improvement is achieved.
The electron contribution to *MET_Simplified20_RefFinal_et* and *MET_RefFinal_et* is both times the same with 87.55 GeV - in both algorithms the same electron collections are used.

A reason for the large difference between the jet contributions to the different E_T^{miss} variables is found. The overlap removal between electrons and jets, removing a jet if it is found nearby an electron, is failing for some events. This was first shown in [60].

8.3.2. Reason for Incorrect Overlap Removal

There is no obvious explanation why the overlap removal fails in some events. Looking at the E_T^{miss} computation in detail, however, shows why the overlap removal is different in the two algorithms and does not cause trouble for *MET_RefFinal_et*.

- For the latter variable, the overlap removal is already done at cell level. A calorimeter cell is no more allocated to a jet if it is already assigned to an electron. This computation is performed when producing the AOD on which the DPD are based.
- For *MET_Simplified20_RefFinal_et*, the overlap removal is done with topological clusters. For every electron, it is checked in envelopes whether clusters are found in its vicinity. This is only done when producing the DPD.

Another consequence of the incorrect overlap removal which can make the difference between the jet contributions to E_T^{miss} even larger, is the issue of scaling the energy of those double-counted objects. An object which is treated as a jet has its energy scaled up for the E_T^{miss} computation with respect to the same object treated as an electron (see discussion about JES in chapter 4.1.2). A jet cluster is therefore multiplied with a scale factor of ~ 1.6. Jets entering the *MET_RefFinal_et* computation are on the other hand calibrated according to their shape in the calorimeter.

It is shown in [61] that the incorrect overlap removal traces back to a technical bug in the DPD production. The overlap removal regarding the E_T^{miss} computation in the corresponding software- code is sometimes wrongly terminated, leading to a false assignment of clusters to objects. This should be fixed in future DPD productions.

8.3.3. Attempt to Fix Incorrect Overlap Removal

An attempt to fix the technical bug in a recalculation of *MET_Simplified20_RefFinal_et* during the analysis is proposed in [62]. It is based on the assumption that looking only at the clusters in the calorimeters, those can be allocated either to an electron or to a jet. Taking into account that electrons are reconstructed at electromagnetic scale (e) and jets at the JES (or hadronic scale, h), it can be in principal assumed that

$$(\frac{e}{h})E_{T\ ele}^{miss} = -\sum_{all\ sel.} p_{T\ jet} - E_{T\ jet}^{miss} \approx -\sum_{overlapping} p_{T\ jet}. \tag{8.2}$$

To put it in words, it means that the transverse momenta of all selected jets which are overlapping with an electron must correspond to the contribution of the electrons to E_T^{miss} when considering $\frac{e}{h}$, or otherwise they would correspond to the contribution of the jets. The clustered energy depositions in the cells are either assigned to electrons or to jets.

When the overlap removal is not performed, the above equation does no longer hold. Now it happens that

$$(\frac{e}{h})E_{T\ ele}^{miss} > -\sum_{overlapping} p_{T\ jet}. \tag{8.3}$$

There are not enough jets removed although they are overlapping with an electron and thus the sum over their p_T becomes smaller than the contribution of the electrons to E_T^{miss}. An indicator is defined by the ratio of

$$\frac{|E_{T\ jet}^{miss} + -\sum_{all} p_{T\ jet}|}{E_{T\ ele}^{miss}} \tag{8.4}$$

which is equal to $\frac{e}{h}$ when there are no overlapping electrons and jets both contributing to E_T^{miss}, but which becomes smaller than $\frac{e}{h}$ if the overlap removal failed. It is recommended to assume $\frac{e}{h} \approx 1$ for this decision. The fix now entails replacing the contributions by

$$MET\_Simplified20\_RefJet\_etx \rightarrow -\sum_{all} p_{x\ jet} - (\frac{e}{h})E_{x\ ele}^{miss}, \tag{8.5}$$

and

$$MET\_Simplified20\_RefJet\_ety \rightarrow -\sum_{all} p_{y\ jet} - (\frac{e}{h})E_{y\ ele}^{miss}. \tag{8.6}$$

$\frac{e}{h}$ is taken from a W→eν sample and varies from ~ 1.9 for *MET_Simplified20_RefEle_et* ≤ 20 GeV to ~ 1.4 for *MET_Simplified20_RefEle_et* > 100 GeV.

The method described above was implemented and the modified *MET_Simplified20_RefFinal_et* results in the turn-on curve shown in figure 8.12.

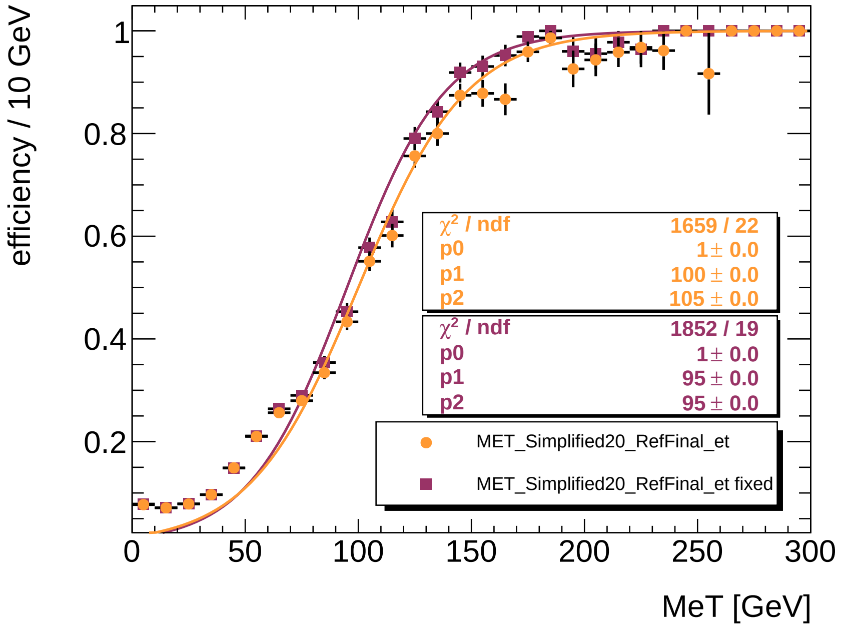

Figure 8.12.: Turn-on curves for *EF_j75_a4tc_EFFS_xe45_loose_noMu* with fixed *MET_Simplified20_RefFinal_et* (purple) and unaffected *MET_Simplified20_RefFinal_et* (orange) on the x-axis in the *Egamma stream*. *MET_Simplified20_RefFinal_et* is modified when the overlap removal is believed to have failed.

The fixed *MET_Simplified20_RefFinal_et* (purple) is compared to the unaffected *MET_Simplified20_RefFinal_et* (orange). The curves still lie pretty much on top of each other, the one for the fixed variable is turning on only slightly faster with little higher p_1 and p_2 fit values. The plateau is still reached only for $E_T^{miss} > 180\,\text{GeV}$ and the efficiency does not level off at $\epsilon = 100\,\%$. The fix based on *MET_Simplified20_RefEle_et* hardly improves the shape of the turn-on curve. Only in rare occasions, in 3 % of all events, equation (8.4) becomes smaller than 1 and the fix is performed.

8.4. E_T^{miss} calculated at DPD Level

In the newest DPD productions (version *p602*), there is also a *MET_RefFinal_et* variable calculated during the step AOD → DPD, namely *MET_Egamma10NoTau_RefFi-*

nal_et[3]. Plotting the turn- on curve in the *Egamma stream* for *MET_Egamma10NoTau_RefFinal_et* results in the orange curve shown in figure 8.13.

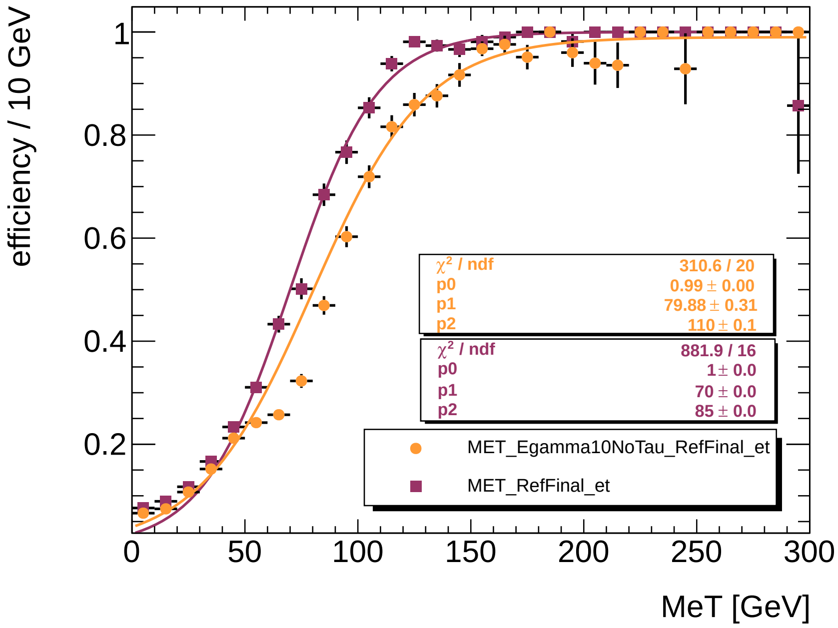

Figure 8.13.: Turn-on curves for *EF_j75_a4tc_EFFS_xe45_loose_noMu* with *MET_Egamma10NoTau_RefFinal_et* (orange) and *MET_RefFinal_et* (purple) on the x- axis in the *Egamma* stream.

It is compared to the one for *MET_RefFinal_et* (purple). So far the *MET_RefFinal_et* computation was believed to be trustworthy but now it becomes apparent that this is no longer the case when it was calculated during the DPD production. The curve for *MET_Egamma10NoTau_RefFinal_et* turns on too slow with $p_1 \approx 80$ GeV and $p_2 \approx 110$ GeV and reaches the plateau only for $E_T^{miss} > 180$ GeV.
MET_RefFinal_et is plotted versus *MET_Egamma10NoTau_RefFinal_et* in figure 8.14. The two variables can differ very much even if they are expected to give approximately the same value.

Already mentioned in chapter 8.3.2 is the difference of the *MET_RefFinal_et* and the *MET_Simplified20_RefFinal_et* algorithms concerning the overlap removal procedure. The different entities which are involved in the overlap removal are actually the only difference between *MET_RefFinal_et* and *MET_Egamma10NoTau_RefFi-*

---

[3] *Egamma10* refers to electrons with $p_T > 10$ GeV which are used for the E_T^{miss} calculation and no τ-leptons were used.

nal_et - the *MET_RefFinal_et* algorithm still accesses the information from the ESDs and assures that no calorimeter cells are included in more than one object. *MET_-Egamma10NoTau_RefFinal_et* by contrast can only allocate the topological clusters to the electrons and jets because it can only demand data from the AODs where information about single calorimeter cells is no more stored.

In [63] some events were checked where the E_T^{miss} calculated during the DPD production is very different to the one calculated during the AOD production. These events serve as examples where *MET_RefFinal_et* is very high in contrary to *MET_-Egamma10NoTau_RefFinal_et*, corresponding to the left upper area in the plot in figure 8.14.

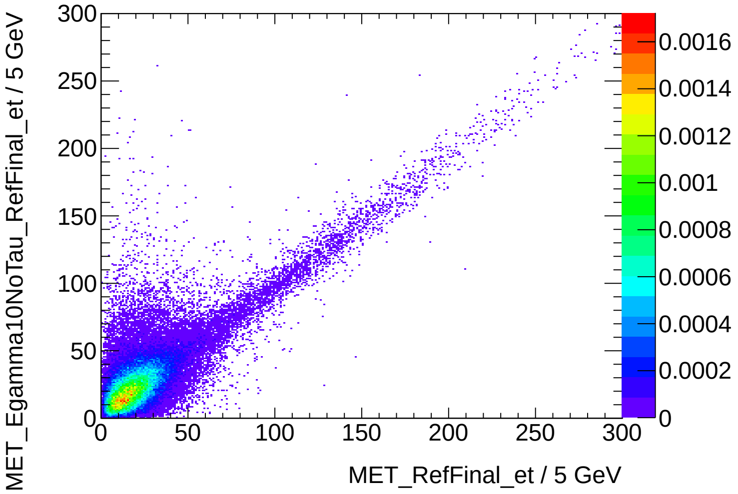

Figure 8.14.: *MET_RefFinal_et* versus *MET_Egamma10NoTau_RefFinal_et*. The distribution is normalized to 1.

Replacing the weighted p_T of the electron by the p_T of the jet shifts the E_T^{miss} variables computed during the DPD production much closer to *MET_RefFinal_et*. The electron is in general less extensive compared to the jet and in addition has a weight smaller than 1. It seems like in this case, the overlap removal overdoes: a jet is completely removed if it contains more cells than the electron which is kept.

Various checks reveal also a deficiency concerning the weights of the electrons and the overlap-removed jets. Overlapping, but removed jets do not enter *MET_Simplified20_-RefFinal_et* or *MET_Egamma10NoTau_RefFinal_et*, meaning they have a weight equal to 0. In [63] it is shown that those jets have a weight >0 when computing *MET_RefFinal_et*. The energy discrepancy is indeed taken into account. Since the removed jets can have a very high p_T, this explains why there can be such disagreement between the E_T^{miss} variables computed at different levels in the data chain.

8.5. Conclusion of E_T^{miss}-Turn-on Curves

The turn-on curve in the *Egamma stream* for the E_T^{miss} variable *MET_Simplified20_-RefFinal_et* shows a strange behaviour as it turns on much too slow compared to the other trigger streams and to *MET_RefFinal_et*. It is recommended to use *MET_Simplified20_RefFinal_et* in the *0-lepton channel* analysis. The two E_T^{miss} algorithms differ significantly but are not expected to do so. The deviations can be ascribed to the jets which enter the E_T^{miss} computation because *MET_RefFinal_et* has a very different contribution from jets. Also the electrons seem to be an issue since the turn-on is too slow in the events where an electron is required in the final state. The turn-on is also too slow in events where electrons contribute more than 1 GeV to E_T^{miss}.

It became apparent that the overlap removal for an electron and a jet using the same cell clusters sometimes fails when computing *MET_Simplified20_RefFinal_et*. The attempt to fix this problematic assignment of clusters to electrons or jets does not lead to the favoured turn-on curve. The jets and electrons are differently calibrated and weighted, and jets in general use broader clusters - therefore it seems not possible to solve the problem on the basis of DPD data samples.

Further checks including the information that can be deduced only from AODs about objects which enter *MET_RefFinal_et* show, that parts of the electron and jet clusters are not taken into account for the *MET_Simplified20_RefFinal_et* computation. The weights for the overlapping and removed jets are different even for the same *MET_RefFinal_et*, depending on whether it was performed during the AOD or the DPD production. Hence, it can only be recommended to use the reliable *MET_RefFinal_et* variable when it was computed during the AOD production. Another idea is of course to further investigate the origin of the problem that sometimes the weights of the jets are dropped out when computing *MET_Simplified20_RefFinal_et* for the DPD. The latter seems to be a technical problem. The details of the allocation of topological clusters to objects during the overlap removal is the troublemaker.
The E_T^{miss} performance group has been made aware of the issues evidenced in this thesis and a first version of the debugged code should be made available soon.

A.

	Data rate [Hz]				
Trigger	$\|\eta\|<2.7$	$\|\eta\|<2.2$	$\|\eta\|<1.7$	$\|\eta\|<1.2$	$\|\eta\|<1.0$
EF_xe80	0.69	0.6	0.43	0.29	0.22
EF_xe70	1.3	1.1	0.77	0.5	0.37
EF_xe60	2.9	2.4	1.6	1.0	0.74
EF_xe55	4.7	3.8	2.4	1.5	1.1
EF_xe50	7.9	6.2	3.9	2.4	1.8
EF_xe45	14	11	6.6	4.1	2.9
EF_xe40	18	14	8.8	5.4	3.9
EF_xe35	25	20	12	7.4	5.3
EF_xe30	34	26	16	10	7.3
EF_xe25	45	35	22	14	9.9
EF_xe20	56	45	28	17	13

Table A.1.: Data rates for real data for the trigger signature *L1_J50_L2_j70_-$|\eta|$xx_EF_j75_xeXX*.Various demands on $|\eta|$ of **two** L2 jets and E_T^{miss} at EF Level are listed. The instantaneous luminosities are $\mathcal{L} = 2.44{\cdot}10^{33}\,\mathrm{cm}^{-2}\mathrm{s}^{-1}$ (period B) and $6.57{\cdot}10^{33}\,\mathrm{cm}^{-2}\mathrm{s}^{-1}$ (period D).

	Efficiency [%]				
Trigger	$\|\eta\|<2.7$	$\|\eta\|<2.2$	$\|\eta\|<1.7$	$\|\eta\|<1.2$	$\|\eta\|<1.0$
EF_xe80	67	64	55	41	32
EF_xe70	74	70	60	45	35
EF_xe60	79	75	65	48	38
EF_xe55	82	78	67	50	40
EF_xe50	85	81	70	52	41
EF_xe45	88	84	72	54	43
EF_xe40	91	86	74	55	44
EF_xe35	93	88	76	57	45
EF_xe30	95	90	78	58	46
EF_xe25	97	92	80	59	47
EF_xe20	99	94	81	60	48

Table A.2.: Efficiency for MC simulated *SU4* signal for the trigger signature *L1_J50_-L2_j70_$|\eta|$xx_EF_j75_xeXX*. Various demands on $|\eta|$ of **two** L2 jets and E_T^{miss} at EF Level are listed.

	Data rate [Hz]				
Trigger	$\lvert\eta\rvert<2.7$	$\lvert\eta\rvert<2.2$	$\lvert\eta\rvert<1.7$	$\lvert\eta\rvert<1.2$	$\lvert\eta\rvert<1.0$
EF_xe80	0.74	0.67	0.53	0.42	0.36
EF_xe70	1.4	1.2	0.92	0.73	0.61
EF_xe60	3.1	2.6	1.9	1.5	1.2
EF_xe55	4.9	4.1	2.8	2.2	1.8
EF_xe50	8.2	6.6	4.5	3.5	2.9
EF_xe45	14	11	7.7	5.9	4.9
EF_xe40	19	15	10	8.0	6.7
EF_xe35	27	22	15	11	9.5
EF_xe30	36	29	20	16	13
EF_xe25	49	40	28	22	19
EF_xe20	63	53	38	30	25

Table A.3.: Data rates for real data for the trigger signature *L1_J30_L2_j50_-$\lvert\eta\rvert$xx_EF_j55_xeXX*. Various demands on $|\eta|$ of the L2 jet and E_T^{miss} at EF Level are listed. The instantaneous luminosities are $\mathcal{L} = 2.44{\cdot}10^{33}\,\mathrm{cm}^{-2}\mathrm{s}^{-1}$ (period B) and $6.57{\cdot}10^{33}\,\mathrm{cm}^{-2}\mathrm{s}^{-1}$ (period D).

	Efficiency [%]				
Trigger	$\lvert\eta\rvert<2.7$	$\lvert\eta\rvert<2.2$	$\lvert\eta\rvert<1.7$	$\lvert\eta\rvert<1.2$	$\lvert\eta\rvert<1.0$
EF_xe80	71	69	64	55	48
EF_xe70	78	76	71	61	53
EF_xe60	85	83	77	66	58
EF_xe55	89	87	81	69	61
EF_xe50	93	91	84	72	63
EF_xe45	97	95	88	75	66
EF_xe40	101	98	91	78	69
EF_xe35	104	102	94	81	71
EF_xe30	108	105	97	84	74
EF_xe25	111	108	100	86	76
EF_xe20	114	111	103	88	78

Table A.4.: Efficiency for MC simulated *SU4* signal for the trigger signature *L1_J30_-L2_j50_$\lvert\eta\rvert$xx_EF_j55_xeXX*. Various demands on $|\eta|$ of the L2 jet and E_T^{miss} at EF Level are listed.

	Data rate [Hz]				
Trigger	$\lvert\eta\rvert$ <2.7	$\lvert\eta\rvert$ <2.2	$\lvert\eta\rvert$ <1.7	$\lvert\eta\rvert$ <1.2	$\lvert\eta\rvert$ <1.0
EF_xe80	0.72	0.63	0.45	0.3	0.23
EF_xe70	1.4	1.1	0.8	0.52	0.39
EF_xe60	3.0	2.5	1.6	1.0	0.77
EF_xe55	4.8	3.9	2.5	1.6	1.1
EF_xe50	8.0	6.3	4.0	2.5	1.8
EF_xe45	14	11	6.8	4.1	3
EF_xe40	19	15	9	5.5	4
EF_xe35	26	20	13	7.7	5.5
EF_xe30	35	28	17	10	7.6
EF_xe25	47	37	23	14	10
EF_xe20	60	48	31	19	14

Table A.5.: Data rates for real data for the trigger signature *L1_J30_L2_j50_-|η|xx_EF_j55_xeXX*. Various demands on $|\eta|$ of **two** L2 jets and E_T^{miss} at EF Level are listed. The instantaneous luminosities are $\mathcal{L} = 2.44 \cdot 10^{33}\,\mathrm{cm}^{-2}\mathrm{s}^{-1}$ (period B) and $6.57 \cdot 10^{33}\,\mathrm{cm}^{-2}\mathrm{s}^{-1}$ (period D).

	Efficiency [%]				
Trigger	$\lvert\eta\rvert$ <2.7	$\lvert\eta\rvert$ <2.2	$\lvert\eta\rvert$ <1.7	$\lvert\eta\rvert$ <1.2	$\lvert\eta\rvert$ <1.0
EF_xe80	69	66	57	42	33
EF_xe70	76	73	63	47	37
EF_xe60	84	79	68	51	40
EF_xe55	87	83	71	53	42
EF_xe50	91	86	74	55	44
EF_xe45	95	90	77	58	46
EF_xe40	99	93	80	60	47
EF_xe35	102	97	83	62	49
EF_xe30	106	100	86	64	51
EF_xe25	109	103	88	66	52
EF_xe20	112	106	91	67	54

Table A.6.: Efficiency for MC simulated *SU4* signal for the trigger signature *L1_J30_-L2_j50_|η|xx_EF_j55_xeXX*. Various demands on $|\eta|$ of **two** L2 jets and E_T^{miss} at EF Level are listed.

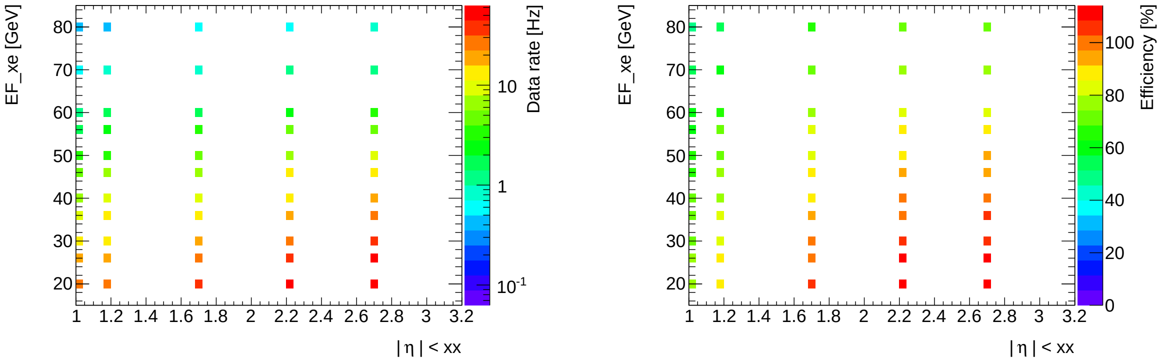

Figure A.1.: Data rate for real data (left) and efficiency for *SU4* MC simulated data (right) indicated by colour on the (logarithmic) z-axis for the trigger signature *L1_J30_L2_j50_*$|\eta|$*xx_EF_j55_xeXX*. Various demands on $|\eta|$ of the L2 jet (x-axis) and E_T^{miss} at EF Level (y-axis) are listed.

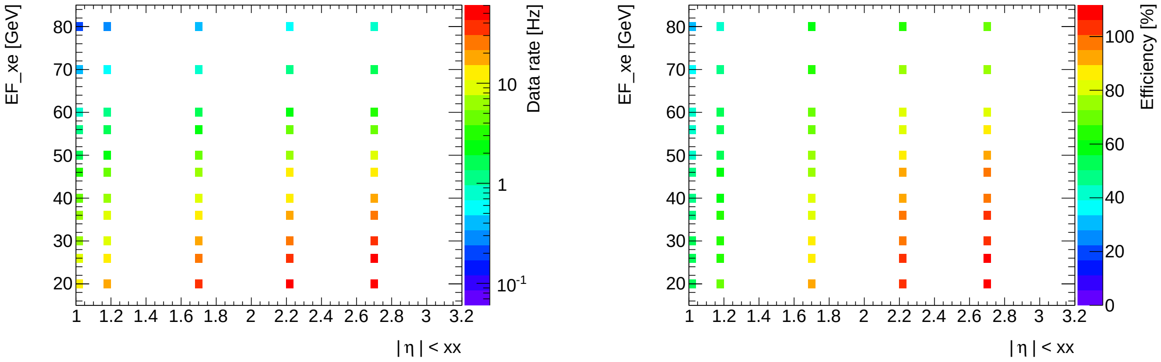

Figure A.2.: Data rate for real data (left) and efficiency for *SU4* MC simulated data (right) indicated by colour on the (logarithmic) z-axis for the trigger signature *L1_J30_L2_j50_*$|\eta|$*xx_EF_j55_xeXX*. Various demands on $|\eta|$ of **two** L2 jets (x-axis) and E_T^{miss} at EF Level (y-axis) are listed.

	Data rate [Hz]				
Trigger	$\lvert\eta\rvert < 2.7$	$\lvert\eta\rvert < 2.2$	$\lvert\eta\rvert < 1.7$	$\lvert\eta\rvert < 1.2$	$\lvert\eta\rvert < 1.0$
EF_xe80	0.6	0.54	0.42	0.33	0.28
EF_xe70	1.2	1.0	0.76	0.59	0.49
EF_xe60	2.6	2.2	1.6	1.2	1.0
EF_xe55	4.2	3.5	2.4	1.9	1.6
EF_xe50	7.0	5.7	3.9	3.0	2.5
EF_xe45	12	9.5	6.4	4.9	4.1
EF_xe40	16	13	8.5	6.6	5.5
EF_xe35	21	17	12	9.1	7.6
EF_xe30	28	23	16	12	10
EF_xe25	36	30	21	17	14
EF_xe20	44	37	27	21	18

Table A.7.: Data rates for real data for the trigger signature *L1_J75_L2_j95_-*$\lvert\eta\rvert$*xx_EF_j100_xeXX*. Various demands on $\lvert\eta\rvert$ of the L2 jet and E_T^{miss} at EF Level are listed. The instantaneous luminosities are $\mathcal{L} = 2.44 \cdot 10^{33}\,\mathrm{cm}^{-2}\mathrm{s}^{-1}$ (period B) and $6.57 \cdot 10^{33}\,\mathrm{cm}^{-2}\mathrm{s}^{-1}$ (period D).

	Efficiency [%]				
Trigger	$\lvert\eta\rvert < 2.7$	$\lvert\eta\rvert < 2.2$	$\lvert\eta\rvert < 1.7$	$\lvert\eta\rvert < 1.2$	$\lvert\eta\rvert < 1.0$
EF_xe80	62	61	57	48	42
EF_xe70	67	65	61	52	46
EF_xe60	71	69	65	55	49
EF_xe55	73	72	67	57	50
EF_xe50	75	74	68	59	52
EF_xe45	77	75	70	60	53
EF_xe40	79	77	72	62	54
EF_xe35	80	78	73	63	55
EF_xe30	81	80	74	64	56
EF_xe25	82	81	75	64	57
EF_xe20	83	82	76	65	57

Table A.8.: Efficiency for MC simulated *SU4* signal for the trigger signature *L1_J75_-L2_j95_*$\lvert\eta\rvert$*xx_EF_j100_xeXX*. Various demands on $\lvert\eta\rvert$ of the L2 jet and E_T^{miss} at EF Level are listed.

	Data rate [Hz]				
Trigger	$\lvert\eta\rvert < 2.7$	$\lvert\eta\rvert < 2.2$	$\lvert\eta\rvert < 1.7$	$\lvert\eta\rvert < 1.2$	$\lvert\eta\rvert < 1.0$
EF_xe80	0.58	0.51	0.37	0.25	0.19
EF_xe70	1.1	0.98	0.68	0.44	0.33
EF_xe60	2.6	2.2	1.4	0.9	0.66
EF_xe55	4.2	3.4	2.2	1.4	1.0
EF_xe50	6.9	5.5	3.5	2.1	1.6
EF_xe45	12	9.1	5.7	3.5	2.5
EF_xe40	15	12	7.5	4.6	3.3
EF_xe35	21	16	10	6.2	4.5
EF_xe30	27	22	14	8.3	6
EF_xe25	35	28	18	11	8
EF_xe20	43	35	23	14	10

Table A.9.: Data rates for real data for the trigger signature *L1_J75_L2_j95_*$\lvert\eta\rvert$*xx_EF_j100_xeXX*. Various demands on $\lvert\eta\rvert$ of **two** L2 jets and E_T^{miss} at EF Level are listed. The instantaneous luminosities are $\mathcal{L} = 2.44 \cdot 10^{33}\,\mathrm{cm}^{-2}\mathrm{s}^{-1}$ (period B) and $6.57 \cdot 10^{33}\,\mathrm{cm}^{-2}\mathrm{s}^{-1}$ (period D).

	Efficiency [%]				
Trigger	$\lvert\eta\rvert < 2.7$	$\lvert\eta\rvert < 2.2$	$\lvert\eta\rvert < 1.7$	$\lvert\eta\rvert < 1.2$	$\lvert\eta\rvert < 1.0$
EF_xe80	61	58	50	37	29
EF_xe70	66	63	54	40	32
EF_xe60	70	67	58	43	34
EF_xe55	72	69	59	44	35
EF_xe50	74	71	61	46	36
EF_xe45	76	72	62	47	37
EF_xe40	77	74	64	48	38
EF_xe35	79	75	65	49	38
EF_xe30	80	76	66	49	39
EF_xe25	81	77	67	50	39
EF_xe20	82	78	68	51	40

Table A.10.: Efficiency for MC simulated *SU4* signal for the trigger signature *L1_J75_L2_j95_*$\lvert\eta\rvert$*xx_EF_j100_xeXX*. Various demands on $\lvert\eta\rvert$ of **two** L2 jets and E_T^{miss} at EF Level are listed.

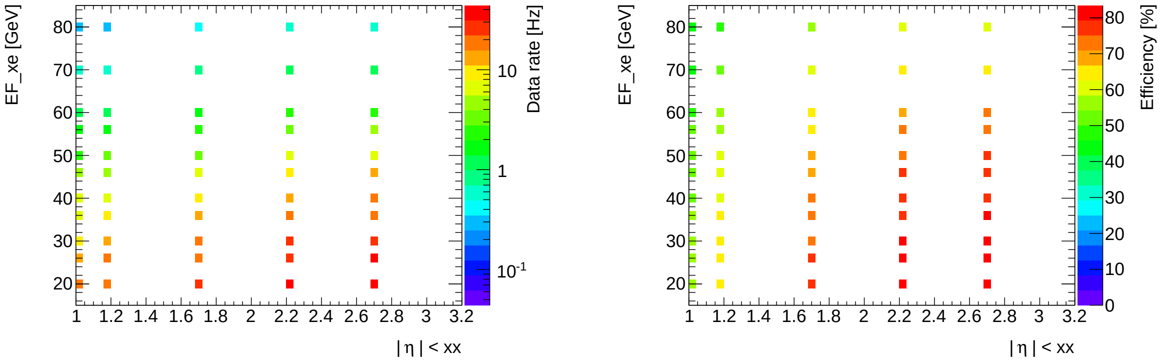

Figure A.3.: Data rate for real data (left) and efficiency for *SU4* MC simulated data (right) indicated by colour on the (logarithmic) z-axis for the trigger signature *L1_-J75_L2_j95_*$|\eta|$*xx_EF_j100_xeXX*. . Various demands on $|\eta|$ of the L2 jet and E_T^{miss} at EF Level (y-axis) are listed.

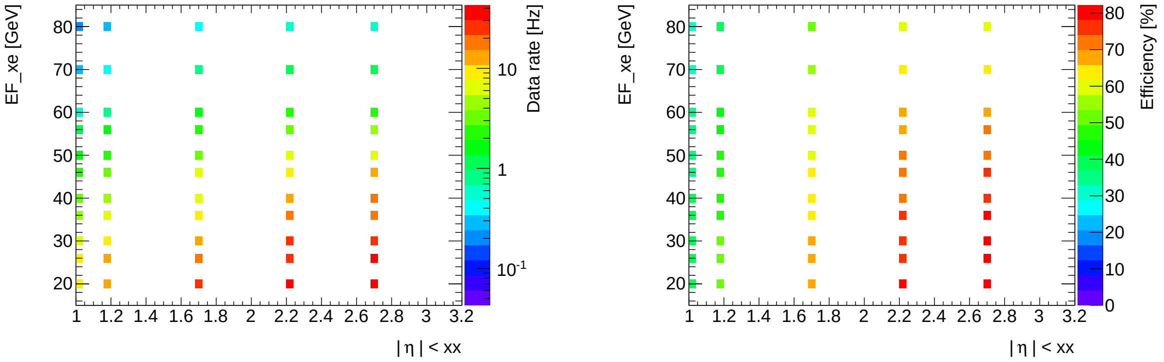

Figure A.4.: Data rate for real data (left) and efficiency for *SU4* MC simulated data (right) indicated by colour on the (logarithmic) z-axis for the trigger signature *L1_-J75_L2_j95_*$|\eta|$*xx_EF_j100_xeXX*. Various demands on $|\eta|$ of **two** L2 jets (x-axis) and E_T^{miss} at EF Level (y-axis) are listed.

B.

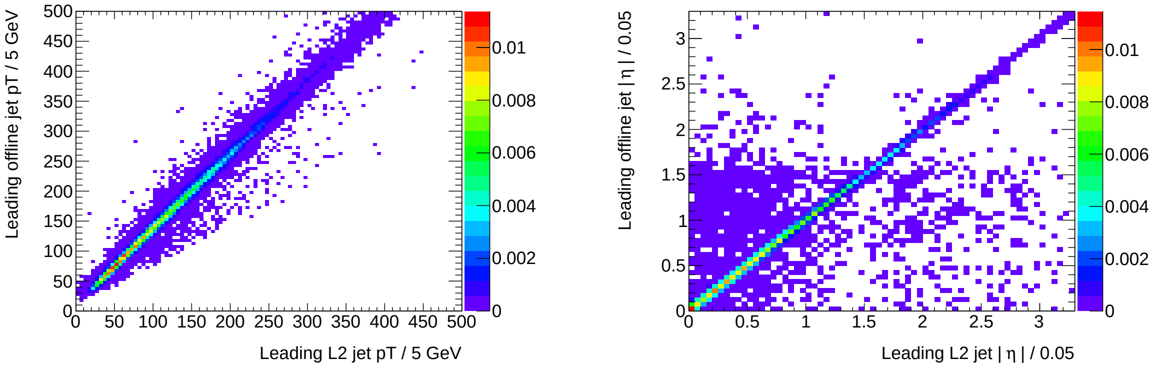

Figure B.1.: MC simulated signal: Distribution of the leading L2 jet p_T versus leading offline jet p_T (left) and distribution of the according $|\eta|$ variables (right). Both distributions are normalized to 1.

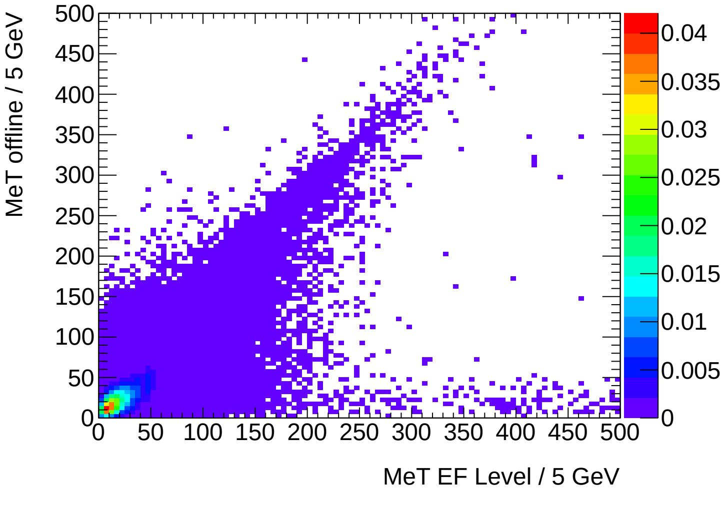

Figure B.2.: Real data: Distribution of E_T^{miss} at EF Level versus E_T^{miss} offline (*MET_-Simplified20_RefFinal_et*). The distribution is normalized to 1.

C.

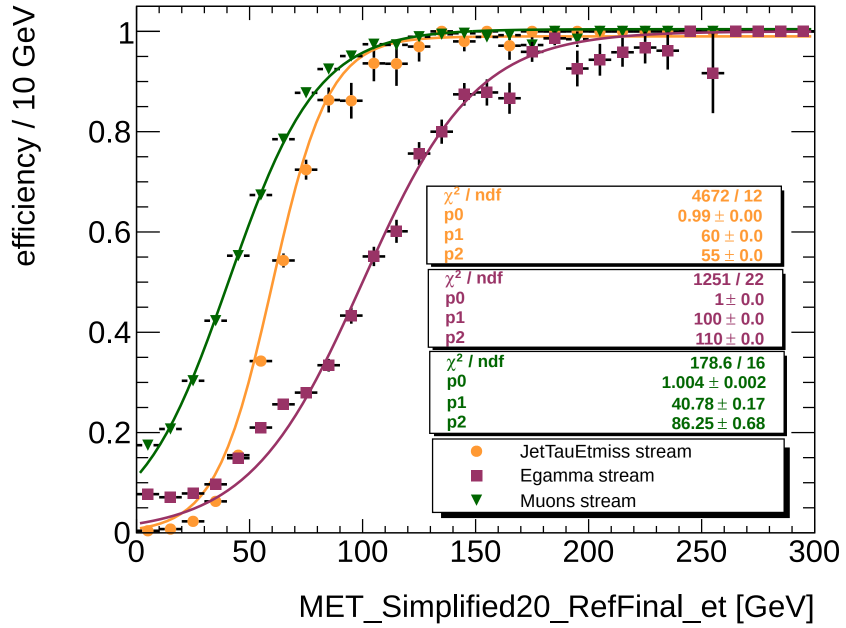

Figure C.1.: Turn-on curves for *EF_j75_a4tc_EFFS_xe45_loose_noMu* with *MET_Simplified20_RefFinal_et* on the x-axis in the *JetTauEtmiss* (orange), *Muon* (green) and *Egamma* (purple) stream. This time the muons have been included in the computation of *MET_Simplified20_RefFinal_et* in the *Muon stream*

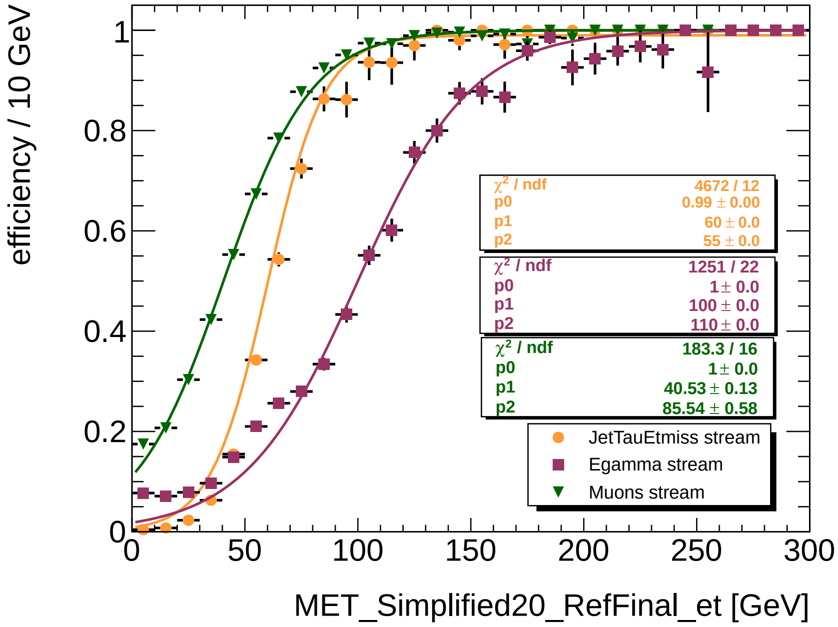

Figure C.2.: Turn-on curves for *EF_j75_a4tc_EFFS_xe45_loose_noMu* with *MET_RefFinal_et* on the x-axis in the *JetTauEtmiss* (orange), *Muon* (green) and *Egamma* (purple) stream. Since there are no muons used for computing E_T^{miss} at EF Level but still for *MET_RefFinal_et*, the curve for the *Muon stream* shows a weird behaviour for low x-values.

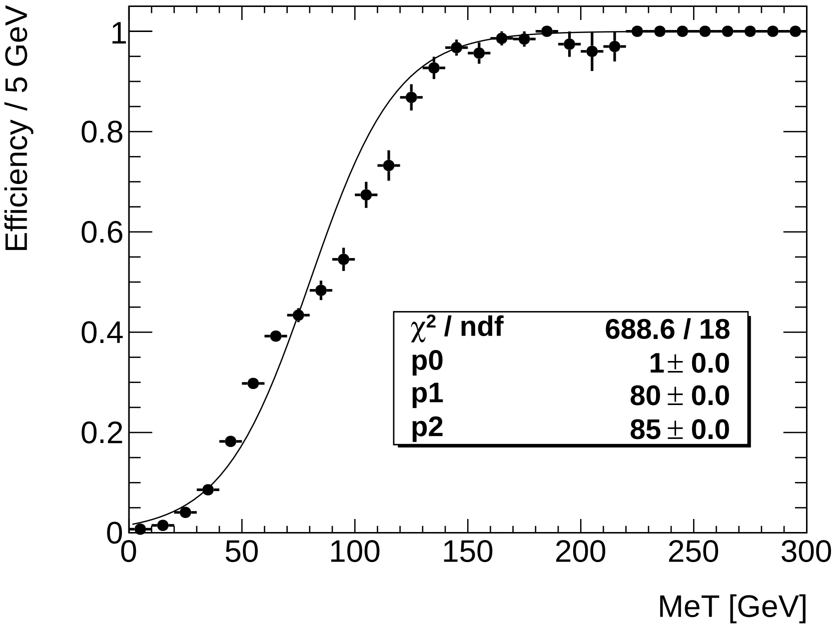

Figure C.3.: Turn-on curve for *EF_j75_a4tc_EFFS_xe45_loose_noMu* with *MET_-Simplified20_RefFinal_et*. The events with $\epsilon > 0\%$ for $E_T^{miss} < 20$ GeV vanish when requiring a leading electron which is identified with medium quality.

Bibliography

[1] Woit, P.: *Imagine There's No God Particle*. 5.9.2001, blog 'Not Even Wrong', `http://www.math.columbia.edu/~woit/wordpress/?p=3960` (URL last visited: September 2011)

[2] Stassler, M.: *Implications of Higgs Searches* 10.9.2011, `http://profmattstrassler.com/articles-and-posts/the-higgs-particle/implications-of-higgs-searches-as-of-92011/` (URL last visited: September 2011)

[3] Capra, F.: *The Tao of Physics*. 1975, Shambhala Publications , Inc.

[4] Griffiths, D.: *Introduction to Elementary Particles*. 2008, Wiley-VCH

[5] Peskin, M. / Schroeder, D.: *Introduction to Quantum Field Theory*. 1987, Addison-Wesley Publishing Company, Inc.

[6] Schaile, D.: *Advanced Particle Physics*. Lecture LMU München SoSe 2010

[7] Particle Data Group: *Particle Physics Booklet*. July 2008, Extracted from *The Review of Particle Physics*: C. Amsler, et al., Physics Letters B 667,1

[8] Bethke, S.: *The 2009 World Average of alpha s*. 15.8.2009, arXiv:0908.1135v2 [hep-ph]

[9] ATLAS collaboration: *ATLAS Design and Physics Performance, Technical Design Report* . 25.5.1999, ATLAS TDR 14, CERN/LHCC 99-14

[10] Berger, C.: *Teilchenphysik, Eine Einführung*. 1992, Springer-Verlag

[11] Martin, S.: *A Supersymmetry Primer*. 10.12.2008, hep-ph/9709356, arXiv:hep-ph/9709356v5

[12] Coleman,S. / Mandula, J.: *All Possible Symmetries of the S Matrix*. 10.11.03 PhysRev.159.1251

[13] Haber, H.: *Supersymmetry, Part I (Theory)*. 2009, `pdg.lbl.gov/2011/reviews/rpp2011-rev-susy-1-theory.pdf` (URL last visited: September 2011)

[14] Eisenhauer, F. / Hasinger, G.: *Einführung in die Astrophysik*. Lecture TU München WiSe 2010/11

[15] Grivaz, J.: *Supersymmetry, Part II (Experiment)*. 2009, `pdg.lbl.gov/2011/reviews/rpp2011-rev-susy-2-experiment.pdf` (URL last visited: September 2011)

[16] Drees, M. / Godbole, R. / Roy, P.: *Theory and Phenomenology of Sparticles*. 2004, World Scientific

[17] Amsler, C.: *Kern- und Teilchenphysik*. 2007, vdf Hochschulverlag AG an der ETH Zuerich

[18] Perkins, D.: *Introduction to High Energy Physics*. 1987, Addison-Wesley Publishing Company , Inc.

[19] Evans,L. / Bryant,P.: *LHC Machine*. 2008 JINST 3 S08001, iopscience

[20] CERN Document Server: *Photos* `http://cdsweb.cern.ch/collection/Photos`

[21] CERN press: *CERN Announces LHC to Run in 2012*. 31.11.2011 `http://press.web.cern.ch/press/PressReleases/Releases2011/PR01.11E.html` (URL last visited: September 2011)

[22] The ATLAS collaboration: *ATLAS Technical Proposal for a General-Purpose pp Experiment at the LHC at CERN*. 15.12.1994 CERN report CERN-LHCC-94-43; LHCC-P-2

[23] The ATLAS Experiment: *Official Website*. `http://www.atlas.ch/` (URL last visited: September 2011)

[24] Lamprecht, M.: *Studien zu Effizienz und Akzeptanz des ATLAS-Myontriggers mit simulierten Messdaten*. 2007, diploma thesis LMU München

[25] The ATLAS collaboration: The ATLAS Experiment at the CERN Large Hadron Collider. 2008 JINST 3 S08003

[26] Biebel, O.: *Detektoren für Teilchenstrahlung*. Lecture LMU München WiSe 2009/2010

[27] The ATLAS Experiment: *Twiki: SlidingWindowClustering*. `https://twiki.cern.ch/twiki/bin/viewauth/Atlas/SlidingWindowClustering` (URL last visited: September 2011)

[28] The ATLAS Experiment: *Twiki: ElectronReconstruction* `https://twiki.cern.ch/twiki/bin/view/AtlasProtected/ElectronReconstruction` (URL last visited: September 2011)

[29] ATLAS Collaboration: *Reconstruction and Identification of Electrons in ATLAS*. ATLAS CSC Note EG-1, `www.physics.smu.edu/web/research/preprints/SMU-HEP-08-21.pdf` (URL last visited: September 2011)

[30] The ATLAS Experiment: *Twiki: Inputs to Jet Reconstruction*. `https://twiki.cern.ch/twiki/bin/view/AtlasProtected/JetInputs` (URL last visited: September 2011)

[31] The ATLAS Experiment: *Topological Clustering*. `https://twiki.cern.ch/twiki/bin/viewauth/Atlas/TopologicalClustering` (URL last visited: September 2011)

[32] Cacciari, M. / Salam, G. / Soyez, G.: *The anti-kT Jet Clustering Algorithm*. JHEP04(2008)063, `http://iopscience.iop.org/1126-6708/2008/04/063` (URL last visited: September 2011)

[33] Joey Huston: *QCD at the LHC*. Lecture 2010, `www.pa.msu.edu/~huston/lhc_lectures/atlas_lecture2.pdf` (URL last visited: September 2011)

[34] The ATLAS Experiment: *Twiki: JetAlgorithms*. `https://twiki.cern.ch/twiki/bin/view/AtlasProtected/JetAlgorithms` (URL last visited: September 2011)

[35] Biebel, O.: *Studien der Quanten-Chromodynamik mit Collider-Experimenten* Lecture LMU München SoSe 2010

[36] Giangiobbe, V.: *Jets Energy Calibration in ATLAS*. 18.-20.2.2009, Workshop sui Monte Carlo, la Fisica e le Simulazioni a LHC, Laboratori Nazionali di Frascati, `moby.mib.infn.it/~nason/mcws4/giangiobbe.pdf` (URL last visited: September 2011)

[37] The ATLAS Experiment: *Twiki: StacoMuon Collections Documentation.* `https://twiki.cern.ch/twiki/bin/view/AtlasProtected/StacoMuonCollection` (URL last visited: September 2011)

[38] Dobbs, M. et al.: *Les Houches Guidebook to Monte Carlo Generators for Hadron Collider Physics.* 5.3.2004, arXiv:hep-ph/0403045v2

[39] Geant4 Collaboration: *Introduction to Geant4.* 17.12.2011, Version: geant4 9.4, `http://geant4.web.cern.ch/geant4/UserDocumentation/UsersGuides/IntroductionToGeant4/html/index.html` (URL last visited: September 2011)

[40] Moretti, S. et al.: *Implementation of Supersymmetric Processes in the HERWIG Event Generator.* 11.4.2002, arXiv:hep-ph/0204123v1

[41] Schouten, D.: *Jet Energy Calibration in ATLAS.* 2007, Masterthesis Simon Fraser University, `hep.phys.sfu.ca/theses/DougSchouten_msc.pdf` (URL last visited: September 2011)

[42] The ATLAS Experiment: *The ATLAS Computing Workbook.* `https://twiki.cern.ch/twiki/bin/viewauth/Atlas/WorkBook` (URL last visited: September 2011)

[43] The ROOT Team: *Webside: Discovering ROOT.* `http://root.cern.ch/drupal/content/discovering-root` (URL last visited: September 2011)

[44] The ATLAS Experiment: *Expected Performance of the ATLAS Experiment.* December 2008, CERN-OPEN-2008-020

[45] Tamsett, M.: *Triggering on Leptons for Beyond the Standard Model Searches at ATLAS.* 2010, CERN-THESIS-2010-136

[46] Genest, M.-H.: *Jet Triggers for Early-Data SUSY Searches.* 3.9.2009, ATL-PHYS-INT-2009-085

[47] ATLAS L1Calo Group: *ATLAS Level-1 Calorimeter Trigger Algorithms.* 13.9.2004, ATL-DAQ-2004-011

[48] The ATLAS Experiment: *Twiki: AtlasHltMetSlice.* `https://twiki.cern.ch/twiki/bin/viewauth/Atlas/AtlasHltMetSlice` (URL last visited: September 2011)

[49] Genest, M.-H.: *Private communications.*

[50] *The ATLAS Experiment*: Twiki: SusyObjectDefinitionsr15, Stream/Trigger. `https://twiki.cern.ch/twiki/bin/view/AtlasProtected/SusyObjectDefinitionsr15` (URL last visited: September 2011)

[51] ATLAS Experiment - Public Results: `https://twiki.cern.ch/twiki/bin/view/AtlasPublic/WebHome` (URL last visited: September 2011)

[52] ATLAS Collaboration: *Search for Squarks and Gluinos Using Final States with Jets and Missing Transverse Momentum with the ATLAS Detector in* $\sqrt{s} = 7$ *TeV Proton-Proton Collisions*. 3.6.2011, ATLAS-CONF-2011-086 and supporting documentation

[53] The ATLAS Experiment: *Twiki: SUSY Object Definitions Release 16*. `https://twiki.cern.ch/twiki/bin/view/AtlasProtected/SusyObjectDefinitionsr16` (URL last visited: September 2011)

[54] The ATLAS Experiment: *Twiki: HowToCleanJets*. `https://twiki.cern.ch/twiki/bin/view/AtlasProtected/HowToCleanJets` (URL last visited: September 2011)

[55] Jet/Etmiss Meeting ATLAS: *LAr Hole Treatment - Summarizing Contributions from Many People*. 22.6.2011, `https://indico.cern.ch/materialDisplay.py?sessionId=0&materialId=0&confId=144227` (URL last visited: September 2011)

[56] Petersen, B.: *2011 Trigger Menu. Introduction to 2011 Triggers and Their Rates at* 10^{33}. 1.2.2011, Trigger General meeting, `https://indico.cern.ch/conferenceDisplay.py?confId=125322` (URL last visited: September 2011)

[57] The ATLAS Experiment: *Twiki: EtMissRefFinal*. `https://twiki.cern.ch/twiki/bin/view/AtlasProtected/EtMissRefFinal` (URL last visited: September 2011)

[58] Mangano, M.L., et al.: *ALPGEN V2.14, A Collection of Codes for the Generation of Multi-Parton Processes in Hadronic Collisions*. `http://mlm.home.cern.ch/mlm/alpgen/` (URL last visited: September 2011)

[59] Butterworth, J., et al.: *JIMMY Generator, Multiparton Interactions in HERWIG*. `http://projects.hepforge.org/jimmy/` (URL last visited: September 2011)

[60] Genest, M.-H.: *Overlap Troubles in MET*. 27.6.2011, ATLAS Analysis Meeting LMU,`https://indico.cern.ch/conferenceDisplay.py?confId=143368` (URL last visited: September 2011)

[61] Yamanaka, T. / Kataoka, Y.: *MET Recalculation Bug Report*. 14.7.2001, ATLAS SUSY Software and Production Meeting, `https://indico.cern.ch/conferenceDisplay.py?confId=146549` (URL last visited: September 2011)

[62] Yamanaka, T. / Kataoka, Y.: *Temporal Solution for MET Recalculation*. Private communications, `https://twiki.cern.ch/twiki/pub/Main/TakashiYamanaka/TemporalMetSolution_110721.pdf` (URL last visited: September 2011)

[63] Genest, M.-H.: *MET Triggers in the Presence of Electrons*. 17.8.2011, ATLAS SUSY Trigger Weekly Meeting, `https://indico.cern.ch/conferenceDisplay.py?confId=150203` (URL last visited: September 2011)

Erklärung

Hiermit versichere ich, dass ich die vorliegende Arbeit selbstständig verfasst und keine anderen als die angegebenen Quellen und Hilfsmittel benutzt habe, dass alle Stellen der Arbeit, die wörtlich oder sinngemäß aus anderen Quellen übernommen wurden, als solche kenntlich gemacht sind und dass die Arbeit in gleicher oder ähnlicher Form noch keiner Prüfungsbehörde vorgelegt wurde.

München, 23. 9. 2011

(Josephine Wittkowski)

Acknowledgements

Ich möchte mich bei allen Personen bedanken, die mich bei der Anfertigung dieser Masterarbeit unterstützt haben.

- Vielen herzlichen Dank an Frau Prof. Dr. Dorothee Schaile, die mich an ihrem Lehrstuhl aufgenommen hat und es mir ermöglicht, diese Arbeit zu verfassen.
- Thank you very much, Dr. Marie-Hélène Genest, for your excellent supervision, for your many ideas, for answering all my questions and for proofreading this thesis.
- Vielen Dank, Frau Franz, für Ihre Hilfe in administrativen Fragen.
- Herzlichen Dank allen Lehrstuhlmitgliedern, die mir in allen fachlichen Fragen mit Rat und Tat zur Seite standen und aber auch für viele vergnügliche Pausen sorgten. Dank hierfür an Josipa Vujaklija, Julien de Graat (auch fürs Korrekturlesen), Sebastian Becker, Nicola Tylor, Christopher Schmitt, Christian Meineck, Alexander Ruschke, Katharina Behr, Prof. Dr. Otmar Biebel, Dr. Albert Engel, Jonas Will, Dr. Thomas Müller, Dr. Johannes Elmsheuser und PD Dr. Thomas Nunnemann.
- Vielen herzlichen Dank, liebe Frauke Alexander, ich hatte viel Spaß mit dir in den letzten Jahren - egal ob im Hörsal, in der Bibliothek, beim Ausgehen oder beim Sport.
- Dankeschön, Tobias Verlage, für viel Spaß und für deine Unterstützung im Studium.
- Herzlichen Dank natürlich auch an all meine nicht-Physiker-Freunde: Monika Schuster, Theresa Weis, Kathrin Jänsch, Miriam Reinhardt, Pia Keller, Sebastian Brummer, Johanne Aga, Matthias Stadler und Peter Scherer.
- Ein riesengroßes Dankeschön an meine Eltern Beate und Andreas Wittkowski, die immer für mich da sind. Danke!
- Danke, Schwesterherz Larissa Wittkowski und danke an meine Großeltern Alfred-Maria und Rosemarie Kellner, Eckart und Maria Wittkowski.
- Danke dir, Thomas Maier - in Liebe.